TNO report

TNO-060-UT-2012-00245

Using basin modeling for geothermal energy exploration in the Netherlands - an example from the West Netherlands Basin and Roer Valley Graben

Date	January 2012
Author(s)	S. Nelskamp J.M. Verweij

Copy no	
No. of copies	5
Number of pages	113 (incl. appendices)
Number of appendices	6
Sponsor	Ministry of Economic Affairs
Project name	4DMod/Geothermie
Project number	034.24607/034.20566

Contents

1 Introduction

The West Netherlands Basin and Roer Valley Graben in the Netherlands have been studied in detail by several authors over the years (Geluk, 1990; Zijerveld et al., 1992; Geluk et al., 1994; De Jager et al., 1996; Van Balen et al., 2000a; Van Balen et al., 2002; Worum and Michon, 2005; Worum et al., 2005; Luijendijk et al., 2010). A lot of the geological research was focused on conventional oil and gas exploration. However the exploration focus currently shifts towards unconventional energy such as geothermal energy or shale gas. For geothermal purposes new questions with regard to porosity/permeability and temperature of sandstone aquifers and the related thermal conductivity have surfaced. More detailed knowledge of eroded thicknesses and the influence of the erosion on the geological framework is important for predicting e.g., porosity / permeability in sandstones and shales. The correct determination of these parameters, especially in a more regional context, are essential for successful exploration of geothermal energy. We use basin modeling to study the thermal and structural evolution of the study area and to determine the necessary parameters for geothermal energy also between wells.

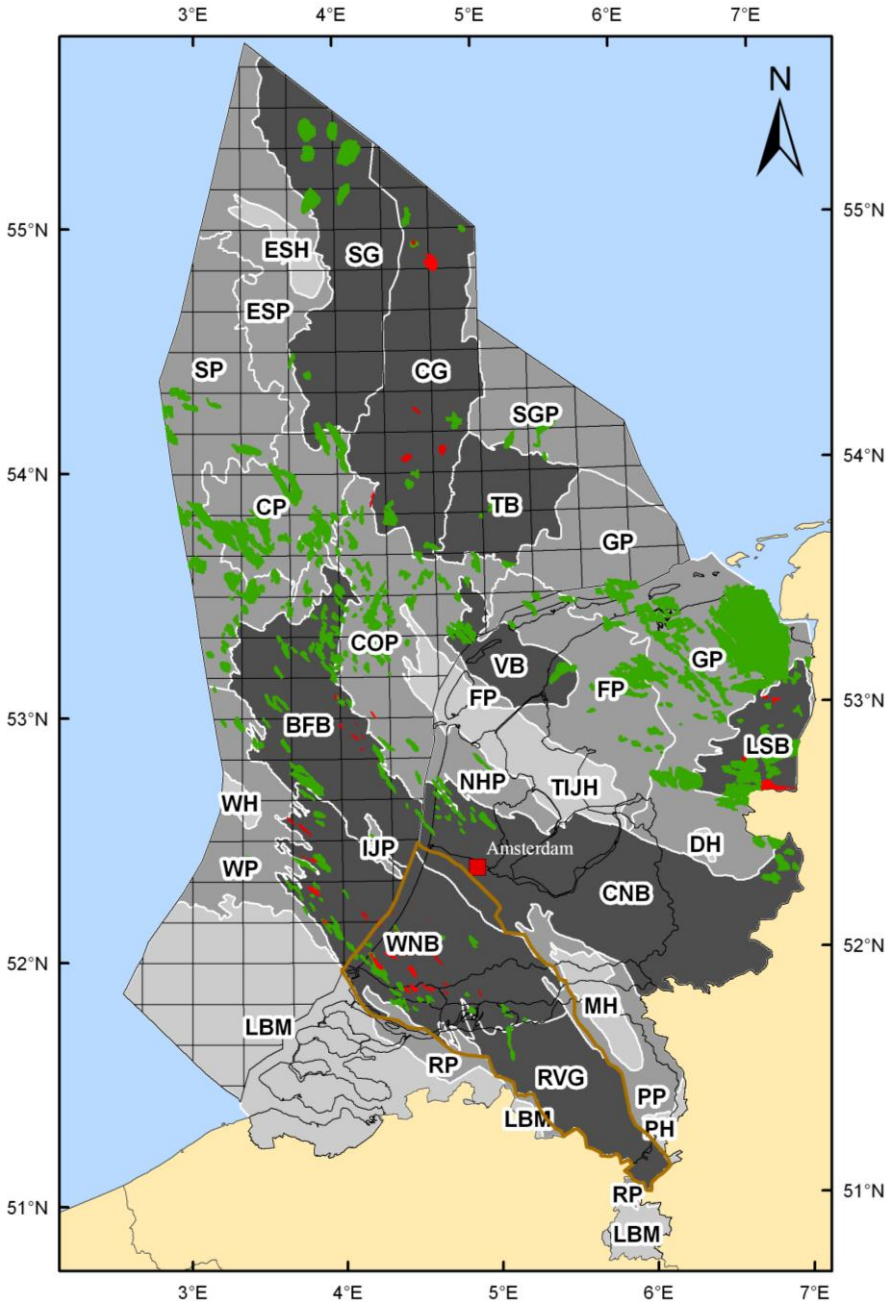

Figure 1 Overview map of the Netherlands with structural elements (grey), known oil (red) and gas (green) fields and position of the study area (brown line)

1.1 Geological setting

The Roer Valley Graben (RVG) belongs to the northwestern part of the Lower Rhine Embayment. It is bordered in southwest to northeast, the Campine Block and respectively the Peel Block. Towards the south the Erft Block is situated, which is not in the prolongation of the RVG but shifted towards the northeast. In Mesozoic times, the West Netherlands Basin (WNB) was the continuation of the RVG with a common tectonic origin and similar tectonic evolution (Worum et al., 2005). Their Cenozoic and especially Neogene/Quaternary evolution

however is different (van Balen et al., 2005; Worum et al., 2005). The transition area between these two Mesozoic structures is characterized by a sedimentation and fault pattern which has similarities to both grabens. The WNB is located in the southwestern part of the Netherlands and extends into the offshore (Figure 1). The basin is bounded to the south by the London-Brabant Massif; the Zandvoort Ridge/IJmuiden High to the north separates it from the Central Netherlands Basin and Broad Fourteens Basin (Van Adrichem Boogaert and Kouwe, 1993).

Between the Late Permian and Early Triassic, the area was characterized by thermal subsidence following the orogenic collapse of the Variscan orogen and minor fault activity as attested by a thick homogeneous sedimentation in the RVG, the WNB and surrounding areas (Zijerveld et al., 1992; Winstanley, 1993). During the Late Jurassic–Early Cretaceous the RVG and WNB have strongly subsided while the surrounding blocks and platforms were uplifted (Zijerveld et al., 1992; Geluk et al., 1994). This was related to major rifting activity and subsidence was controlled by the reactivation of pre-existing Variscan faults as normal faults. During the Late Cretaceous/Early Tertiary several inversion events removed most of the sediments deposited during the Late Jurassic/Early Cretaceous (Winstanley, 1993). In the RVG the major phase of uplift and erosion occurred already in the Campanian and later inversion events had only little effect which can be seen in well logs and biostratigraphic analyses of the Late Cretaceous sediments in the southern RVG. They show a Late Maastrichtian to Danian age and therefore represent chalk deposition after the major inversion phase (Luijendijk et al., 2011). In the WNB the later inversion events had more influence; the Late Maastrichtian to Danian sediments are not observed. Whether most erosion occurred during the Campanian or Latest Cretaceous/Early Tertiary cannot be deduced from the stratigraphic record (De Jager, 2003).

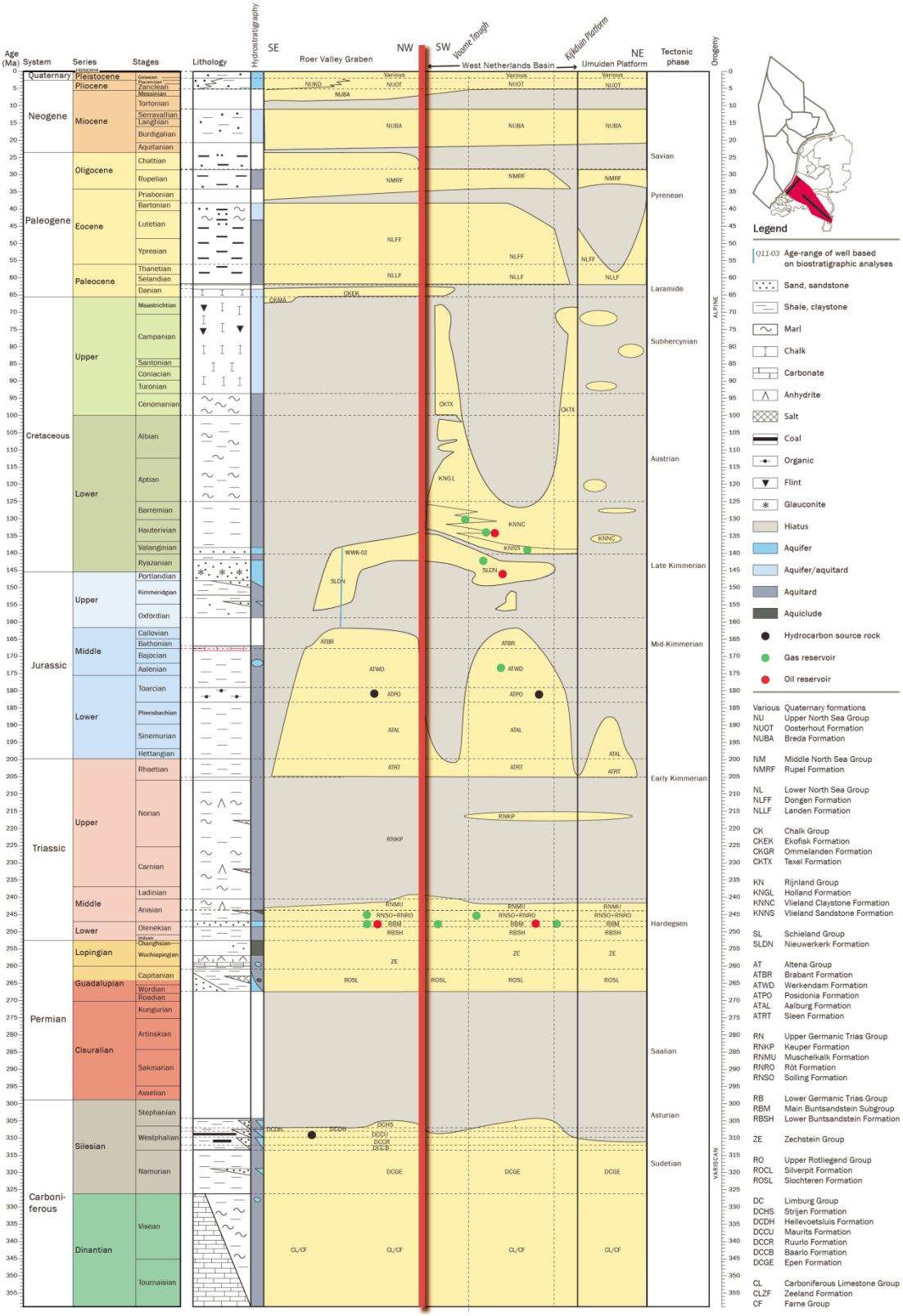

Figure 2 Tectono-stratigraphic chart of the West Netherlands Basin and the Roer Valley Graben. Timescale and ages mostly according to (Gradstein et al., 2004), except (1) the Triassic (according to Kozur and Bachmann, 2008), (2) the Upper Jurassic (according to Munsterman et al. in prep) and (3) the Quaternary (according to the International Commission on Stratigraphy, 2009). The Western European nomenclature is used for the Carboniferous series and stages.

1.2 Hydrocarbon system

Two major source rocks in the WNB are generally accepted to occur (De Jager et al., 1996). The Late Carboniferous (Westphalian) type III source rock consists of coals and shales. The average coal content is about 5.5% (Dusar et al., 1998), the TOC of the coals is at least 70% (Van Bergen, 1998). The second important source rock is of Early Jurassic age. The Posidonia Shale Formation (5-10% TOC) and the underlying Aalburg Formation (1-3% TOC) are type II source rocks. Further source rock intervals situated in the Late Jurassic and in the Namurian and Dinantian deposits are generally considered to be of less importance (Van Balen et al., 2000b).

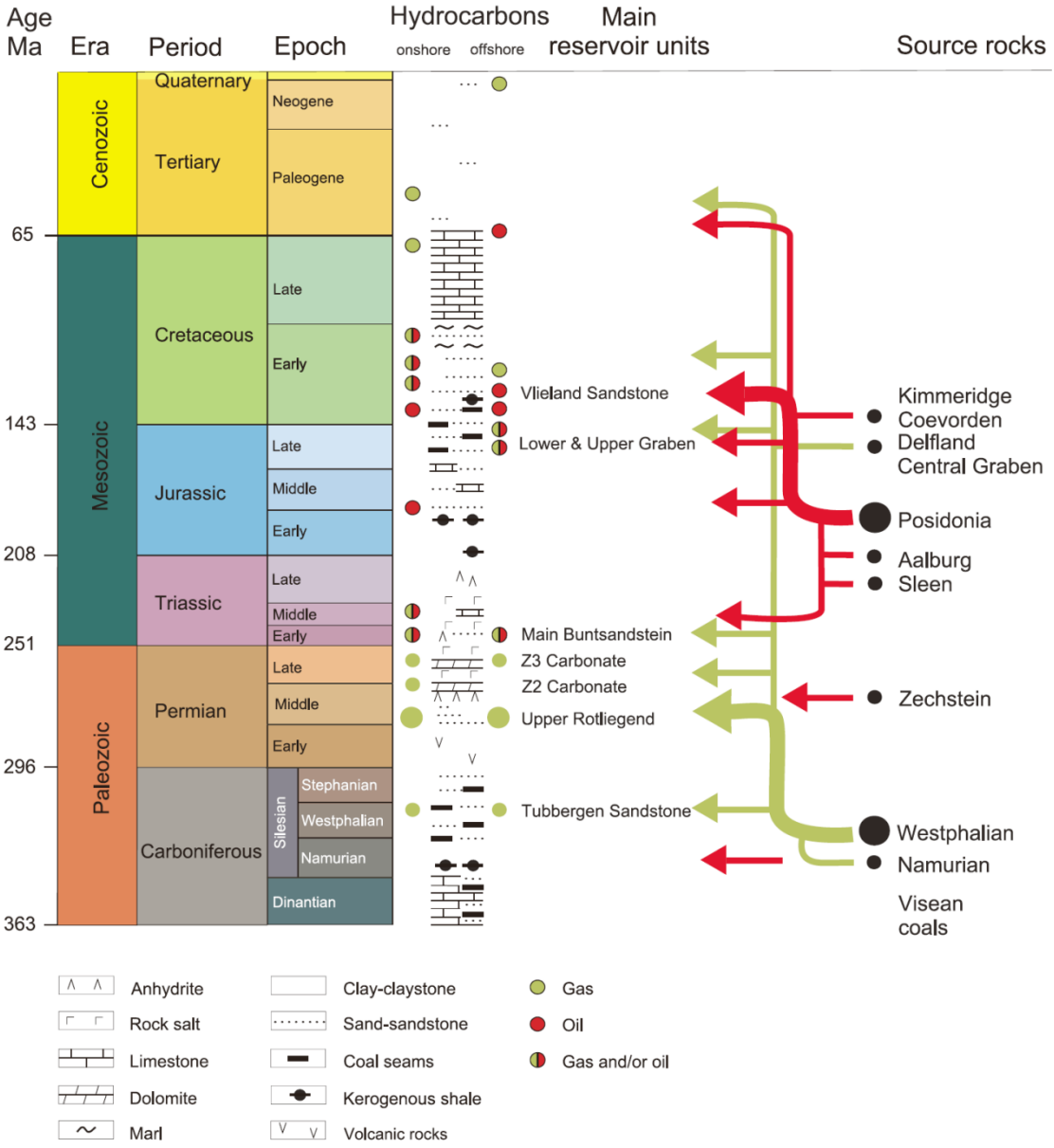

Figure 3 Hydrocarbon system in the Netherlands (from De Jager and Geluk, 2007)

Most gas fields in the WNB occur in sandstones of the Main Buntsandstein Subgroup and the Röt Fringe Sandstone Member, while the Early Cretaceous sandstones contain mainly oil. The Permian Zechstein Fringe Sandstone Members, the Middle Jurassic Middle Werkendam Member and Brabant Formation, the Late Cretaceous Chalk Group, and the Early Tertiary Dongen Sand Member also have reservoir quality and contain some oil or gas fields (Figure 2 and Figure 3). The hydrocarbon accumulations in Triassic reservoirs occur in tilted fault block structures. The traps depend on top sealing by Late Triassic evaporites, tight sandstones, siltstone, shales and dolomites and lateral sealing by faulting-induced juxtaposition of the reservoir against Early and Middle Jurassic shales (De Jager et al., 1996). The hydrocarbons in reservoirs of the Early Cretaceous are trapped in anticlinal structures formed during the inversion events, above reversed normal faults. The reservoirs along the northern and eastern rim of the WNB are mainly filled by biodegraded oil. This could have been caused by exposition of the Lower Cretaceous and Jurassic formations to the surface during the inversion phases (De Jager et al., 1996), which implies that these reservoirs were filled before or during the inversion events. A detailed description of the hydrocarbon system in the WNB is given by Van Balen et al. (2000b)

1.3 Parameters for geothermal energy

Geothermal energy in the Netherlands can be used for a number of applications, such as heating of greenhouses or office buildings. To assess the amount of energy that can be extracted from the earth using current technology, the ThermoGIS tool was developed that displays available sandstone reservoirs, depth, temperature and flow properties of the layers (www.thermogis.nl). So far, the generated information is based on the present-day burial, a temperature gradient for the entire Netherlands. Temperature and porosity measurements are, however, only available at public well locations. The determination of these parameters on a regional level requires their estimation between the wells. Instead of an interpolation between the measured temperature and porosity values, basin modeling includes the effect of present and past burial, which has an important effect (Calignano, 2009). As described in chapter 1.1 the Netherlands encountered at least two phases of significant uplift and erosion important for the proper assessment of geothermal energy. The presented model was constructed to look into these past events and estimate the amount of erosion and its influence on the temperature and porosity/permeability of the reservoir horizons and thus geothermal potential.

2 Basin modeling

To model sediment parameters between well positions, basin modeling was performed with PetroMod v11 of Schlumberger. Basic data requirements for the modeling are the present-day geometry, lithological description of the layers and their properties, absolute ages for stratigraphic layers and times of non-deposition and erosion, boundary conditions such as paleo surface temperature, heat flow and water depth and temperature, maturity and compaction calibration data, to calibrate the model to actual measurements. No tectonic reconstruction was performed; the model therefore takes only vertical movement and compaction into account and does not address lateral compressive or extensive movements. All input maps must be continuous over the whole model and represent a chronostratigraphically described horizon. Chemical compaction is not included in the modeling. Pressure is calculated and calibrated to present-day pressure measurements. Fluid flow in the model is calculated, its effects on the temperature field are however not taken into account.

2.1 Present-day geologic model

The model is a refined version of the onshore maps published in the Geological Atlas of the Subsurface of the Netherlands in 2004. The layers of the model were tied to newly released and refined wells, the Pliocene and Pleistocene intervals were added based on the detailed shallow subsurface model, the reservoir horizons of the Rijnland, Upper and Lower Germanic Trias and Rotliegend were added and the Carboniferous layers as described in the PetroPlay project were included. The full model for the whole of the Netherlands onshore is published as part of ThermoGIS (www.thermogis.nl).

In total 46 depth maps served as the basic stratigraphic input of the model, 18 depth maps for the larger stratigraphic groups and 28 maps on member and formation level for reservoir horizons. The member and formation maps were generated in the context of the ThermoGIS project and are interpreted maps of the main reservoir sandstone horizons. However these maps are only determined for the areas where the sandstone is present and are not continuous chronostratigraphic maps, which can cause problems with respect to the paleo-geometry of the model. A detailed list of all maps is given in Table 1.

2.2 Ages

A consecutive age is assigned to all events/horizons in the model. This includes times of non-deposition and erosion. The ages are based on the international geologic time scale of Gradstein et al. (2004) and adjusted for the Netherlands.

Table 1 Conceptual model of deposition, non-deposition and erosion

Stratigraphic layer	Deposition		Erosion		Color
	from	to	from	to	
Holocene	0.01	0	0	0	
Upper Pleistocene	0.13	0.01	0	0	
Middle Pleistocene	0.78	0.13	0	0	
Base Quatenary	3.1	1.8	0	0	
Pliocene	5.8	3.1	0	0	
NU	20.1	5.8	0	0	
NM	35.4	20.4	0	0	
NL	58	40	40	35.4	
CKEK	65.5	62	62	58	
Top CKGR	73	65.5	0	0	
Rest of CK	99.1	80	80	78	
KNGL	121.8	99.1	0	0	
KNNSL	125.4	124.3	0	0	
KNNCU	125.8	125.4	78	76	
KNNSY	127.2	125.8	0	0	
KNNCA	127.4	127.2	0	0	
KNNSB	129	127.4	0	0	
KNNSC	131.1	129	0	0	
KNNSR	137.4	131.1	0	0	
KNNC	138.7	137.4	0	0	
S_Jurassic erosion	151	149	149	144	
S_Cretaceous erosion	156.4	151	76	74	
AT_Jurassic erosion	170	156.4	144	141	
AT_Cretaceous erosion	203.6	170	74	73	
RNKP and RNMU	244	203.6	141	138.7	
RNROF	245.6	244	0	0	
RNSO	246.2	245.6	0	0	
RBMH	247.2	246.2	0	0	
RBMDU	247.6	247.2	0	0	
RBMDL	247.8	247.6	0	0	
RBMVU	248.5	247.8	0	0	
RBMVL	249	248.5	0	0	
RBSH	250	249	0	0	
ZE	258	250	0	0	
ROCL top	259	258	0	0	
ROSL	264	259	0	0	
ROCL bot	267.5	264	0	0	
DCH	308.7	299	290	285	
DCD	311	308.7	285	280	
DCCU	312.3	311	280	275	
DCCR	313.1	312.3	275	270	
DCCB	313.6	313.1	270	268	
DCGE2	315	313.6	0	0	
DCGE1	316.4	315	0	0	
DCGEG	326.4	316.4	0	0	

2.3 Lithology

Table 2 Lithology of the stratigraphic horizons. The numbers in the second column indicate the composition of the mixed lithology

Name	Lithology	Name	Lithology
Holoceen	50_Sand_50_Shale	RNRO1	90_Salt_10_Anhy
Upper Pleistocene	50_Sand_50_Shale	RNROF	75_Sand_25_Shale
Middle Pleistocene	50_Sand_50_Shale	RNSO	50_Sand_50_Shale
Lower Pleistocene	50_Sand_50_Shale	RBMH	75_Sand_25_Shale
Pliocene	75_Sand_25_Shale	RBMDU	50_Sand_50_Shale
NU	75_Sand_25_Shale	RBMDL	75_Sand_25_Shale
8_n_nosand	80_Shale_10_Sand_ 10_Silt	RBMVU	100_Sandstone
8_n_sandshale	75_Shale_25_Sand	RBMVL	100_Sandstone
8_n_withmarl	50_Shale_25_Marl_ 25_Sand	RBSH	45_Shale_25_Sand_ 25_Silt_5_Lime
CK	100_Chalk	43_ze_withanhy	80_Shale_10_Anhy_ 10_Lime
KNGL	50_Shale_25_Marl_ 25_Sand	43_ze_withlime	75_Shale_25_Lime
KNNSL	75_Sand_25_Shale	43_ze_onlyshale	100_Shale
KNNCU	100_Shale	43_ze	75_Shale_25_Marl
KNNSY	100_Sandstone	ROCL_top	75_Shale_25_Sand
KNNCA	75_Shale_25_Marl	ROSL	100_Sandstone
KNNSB	100_Sandstone	ROCL_bot	75_Shale_25_Sand
KNNSC	75_Sand_25_Shale	DCH	75_Shale_25_Sand
KNNSR	100_Sandstone	DCD	60_Sand_20_Silt_ 18_Shale_2_Coal
KNNC	100_Shale	DCCU	80_Shale_15_Sand_ 5_Coal
25_s_moresand	34_Shale_33_Sand_ 33_Silt	DCCR	78_Shale_20_Sand_ 2_Coal
25_s	48_Shale_25_Sand_ 25_Silt_2_Coal	DCCB	48_Shale_25_Sand_ 25_Silt_2_Coal
ATWD	75_Shale_25_Silt	DCGE2	75_Shale_25_Sand
ATPO	100_Shale	DCGE2	75_Shale_25_Sand
ATAL	75_Shale_25_Silt	DCGEG	80_Shale_10_Sand_ 10_Silt
RNKP_RNMU	70_Shale_15_Anhy_ 15_Marl		

The assigned lithology in the basin model (Table 2) determines the physical parameters and relations during the modelling such as mechanical compaction, thermal conductivity, permeability and heat capacity of the layer. Mixed lithologies based on the standard PetroMod lithologies were used for all layers. The definition of the lithology is based on the description of the Groups, Formations and Members from Van Adrichem Boogaert and Kouwe (1993). To achieve a more detailed view the lithology of three horizons was specified using the stratigraphic information from the wells (Figure 4).

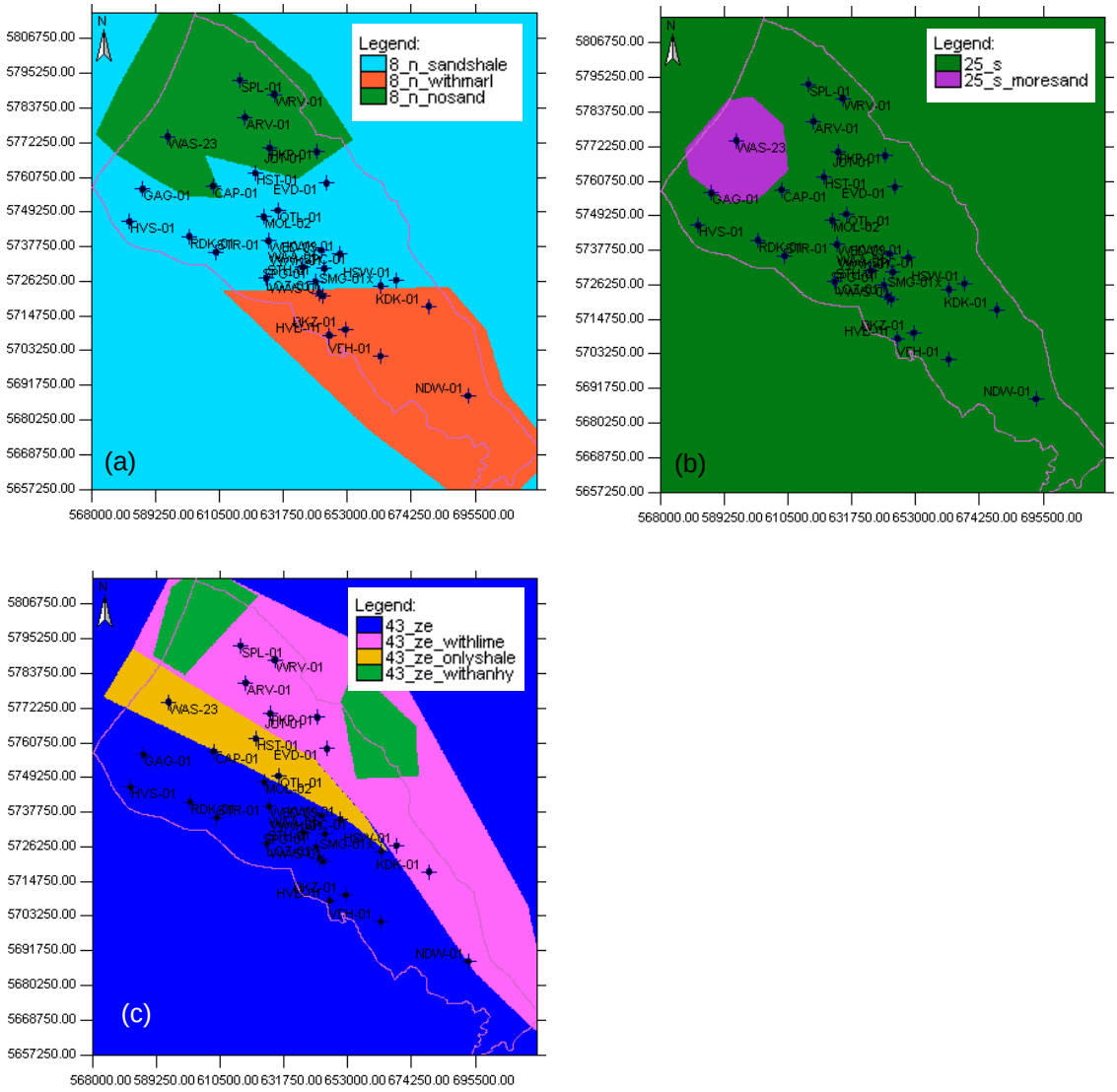

Figure 4 Lithology map for the Middle and Lower North Sea Group (a), the Schieland Group (b) and the Zechstein Group (c)

2.4 Calibration data

Vitrinite reflectance measurements of 22 wells were used for calibration of the model. The quality of the values was assessed based on the availability of measuring information and the number of measurements. A color code was used to display the quality with green representing good values, orange representing values with a limited amount of measurements per value and red indicating values with no information or a very limited number of measurements. Temperature measurements in different qualities from 27 wells were available for calibration of the simulated present-day temperature field. The same color code as for the vitrinite reflectance measurements was used. 23 wells that had porosity and permeability measurements were used for calibration. Well NDW-01 in the Roer Valley Graben had fission track measurements, that could be used to date uplift and erosion in the area.

2.5 Boundary conditions

Boundary conditions include the sediment-water interface temperature, the water depth and the basal heat flow. They define the upper and lower temperature boundary of the model.

Sediment-water interface temperature
The evolution of the sediment-water interface temperature used for the model was defined using the standard model from PetroMod with a refined curve for the Tertiary and Quaternary (Figure 5). The refined curve was determined using geochemical and geobiological proxies (Donders et al., 2009 Verweij et al. in press).

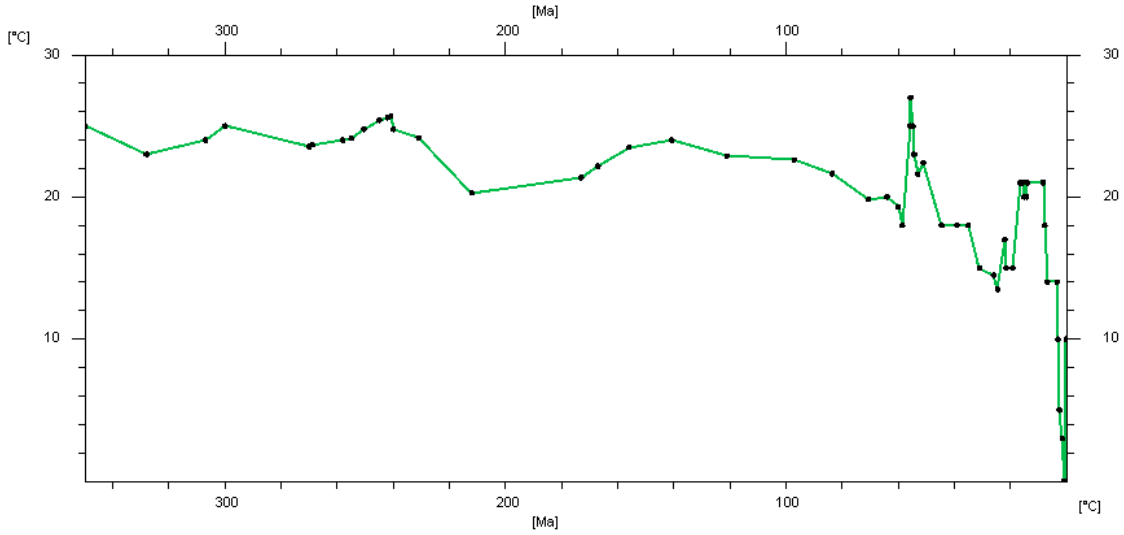

Figure 5 Sediment-water interface temperature as used in the model

2.5.1 Water depth

The water depth is necessary to determine the depth below sea-floor through time and the temperature at the top of the sediments if only surface temperatures are available. The water

depth was determined from the sedimentological desctiptions of Van Adrichem Boogaert and Kouwe (1993) and from micropaleontological studies (Figure 6). The water depth at a certain time was kept constant for the whole area as no more detailed information was available.

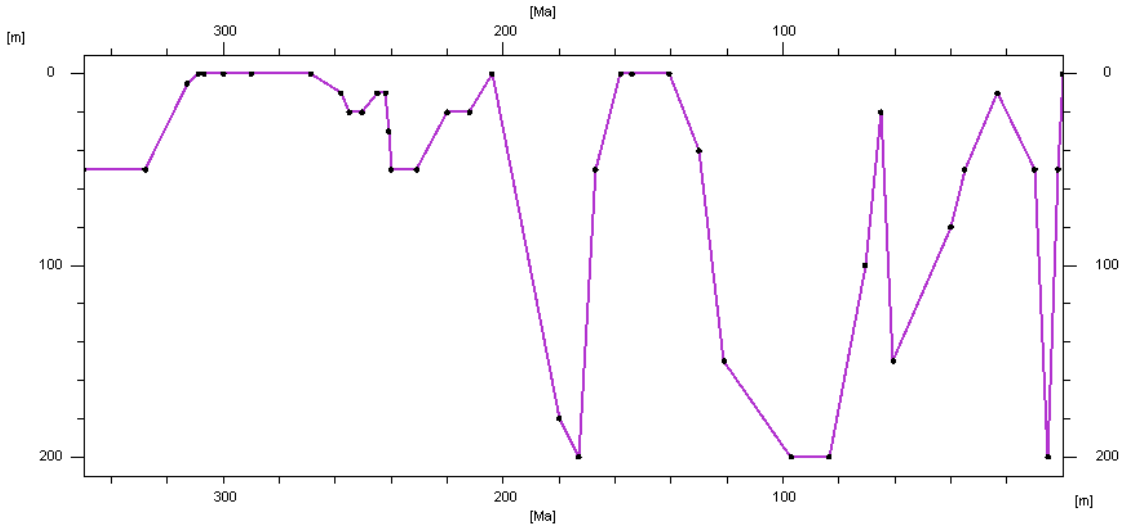

Figure 6 Water depth through time used in the model

2.5.2 *Basal heat flow*

The basal heat flow through time describes the lower thermal boundary of the model. It is difficult to measure. Only present-day well temperatures give an indication of the present-day basal heat flow. However the paleo evolution is mostly based on assumptions calibrated to paleo temperature indicators such as vitrinite reflectance, fluid inclusions or fission track measurements. However, with the exception of fission track measurements, these measurements give no indication of the time of the measured temperature and in the case of vitrinite reflectance only the maximum temperature ever experienced is recorded. In addition we used tectonic subsidence modeling to derive the evolution of the paleo heat flow with PetroProb (see Van Wees et al., 2009 for detailed explanation).

In the basin modeling four different heat flow scenarios were used. The first scenario uses a constant heat flow of 60 mW/m^2 for the whole model. The second scenario uses a heat flow map calibrated on the measured present-day temperatures for the whole time. The third scenario uses heat flow maps for 25 time steps created with PetroProb. The fourth scenario uses the heat flow maps created for the third scenario and calibrated them to temperature and vitrinite reflectance measurements from wells. All maps include the spatial variation of the heat flow. To visualize the differences between the scenarios and also their spatial and temporal variation, a comparison of the four different scenarios for 5 different well positions is shown in Figure 7 a-e.

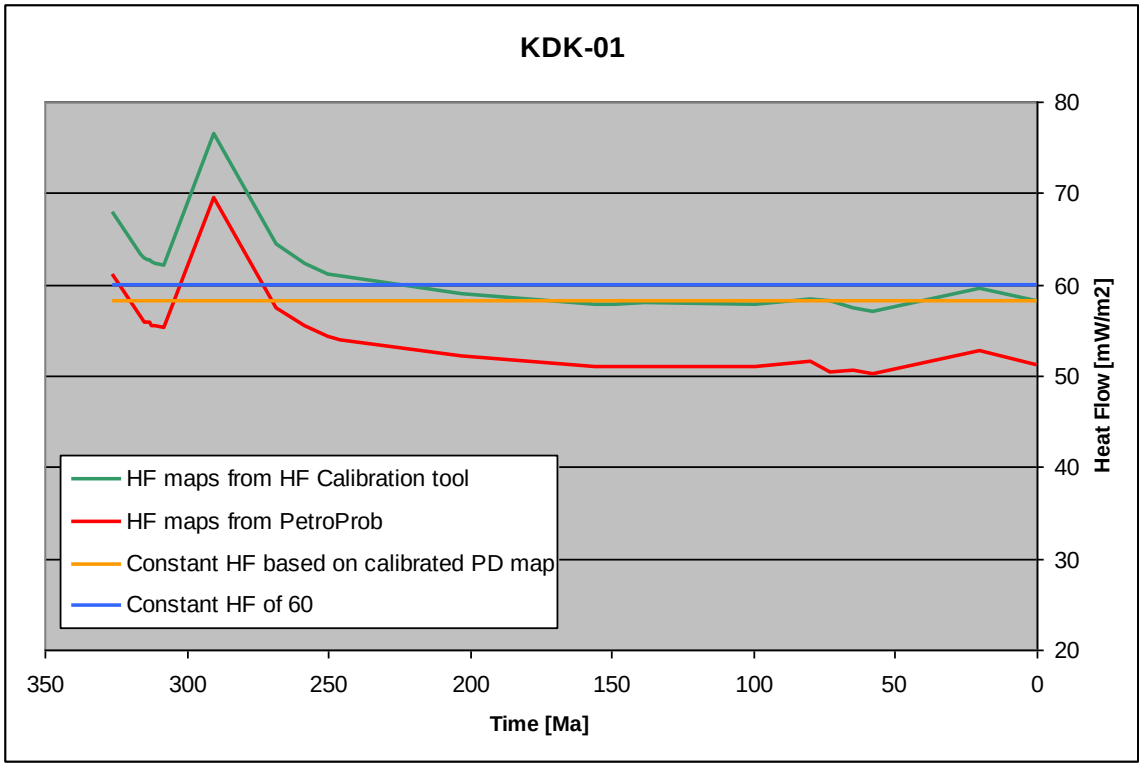
KDK-01
80
70
60
50
40
30
20
Heat Flow [mW/m2]
350
300
250
200
150
100
50
0
Time [Ma]
HF maps from HF Calibration tool
HF maps from PetroProb
Constant HF based on calibrated PD map
Constant HF of 60

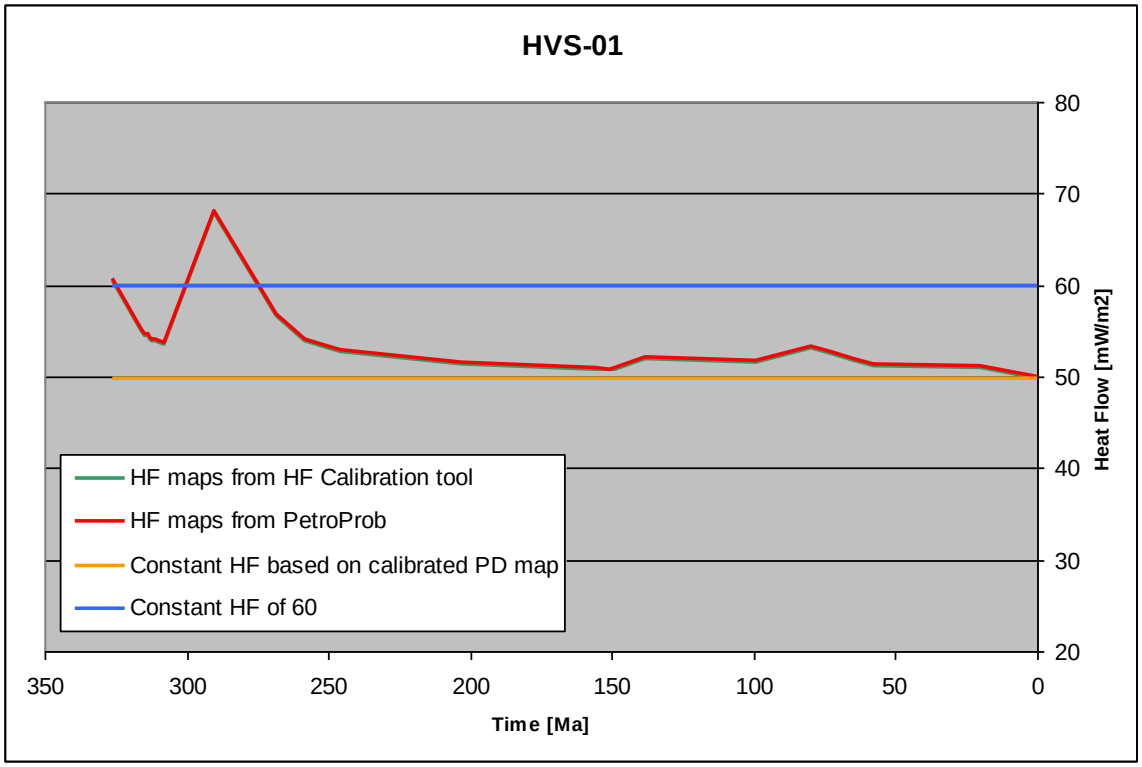
HVS-01
80
70
60
50
40
30
20
Heat Flow [mW/m2]
350
300
250
200
150
100
50
0
Time [Ma]
HF maps from HF Calibration tool
HF maps from PetroProb
Constant HF based on calibrated PD map
Constant HF of 60

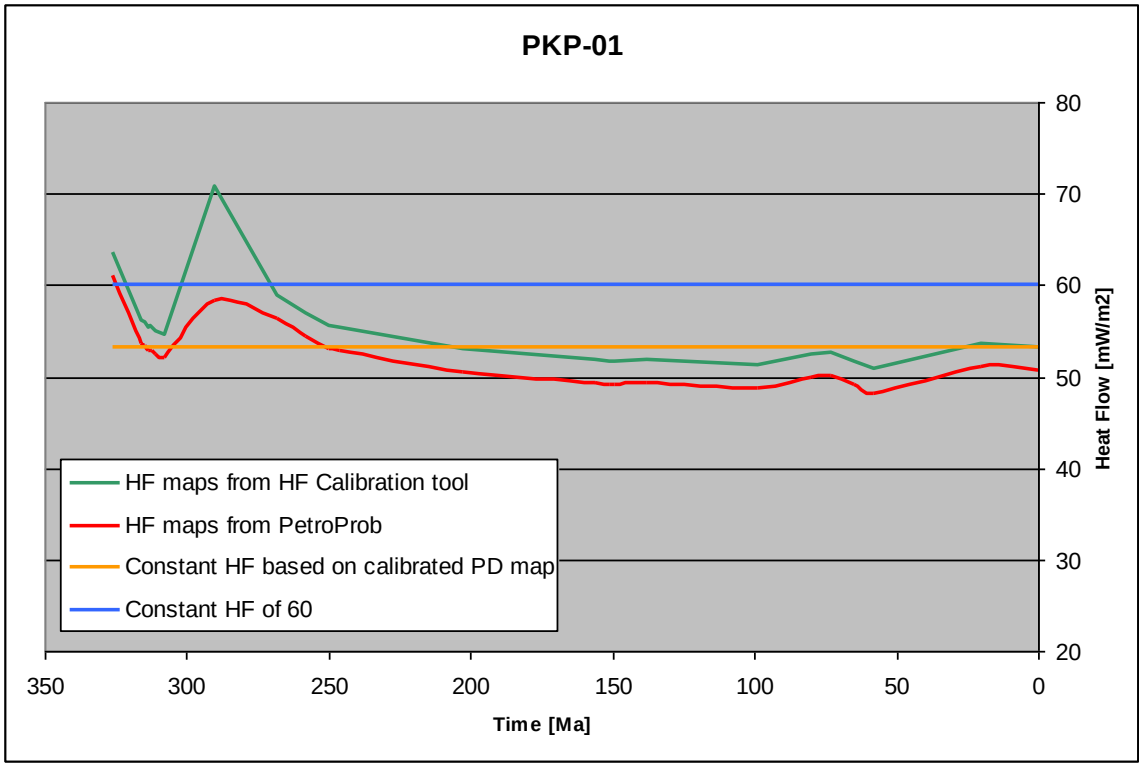
PKP-01
80
70
60
50
40
30
20
Heat Flow [mW/m2]
350
300
250
200
150
100
50
0
Time [Ma]
HF maps from HF Calibration tool
HF maps from PetroProb
Constant HF based on calibrated PD map
Constant HF of 60

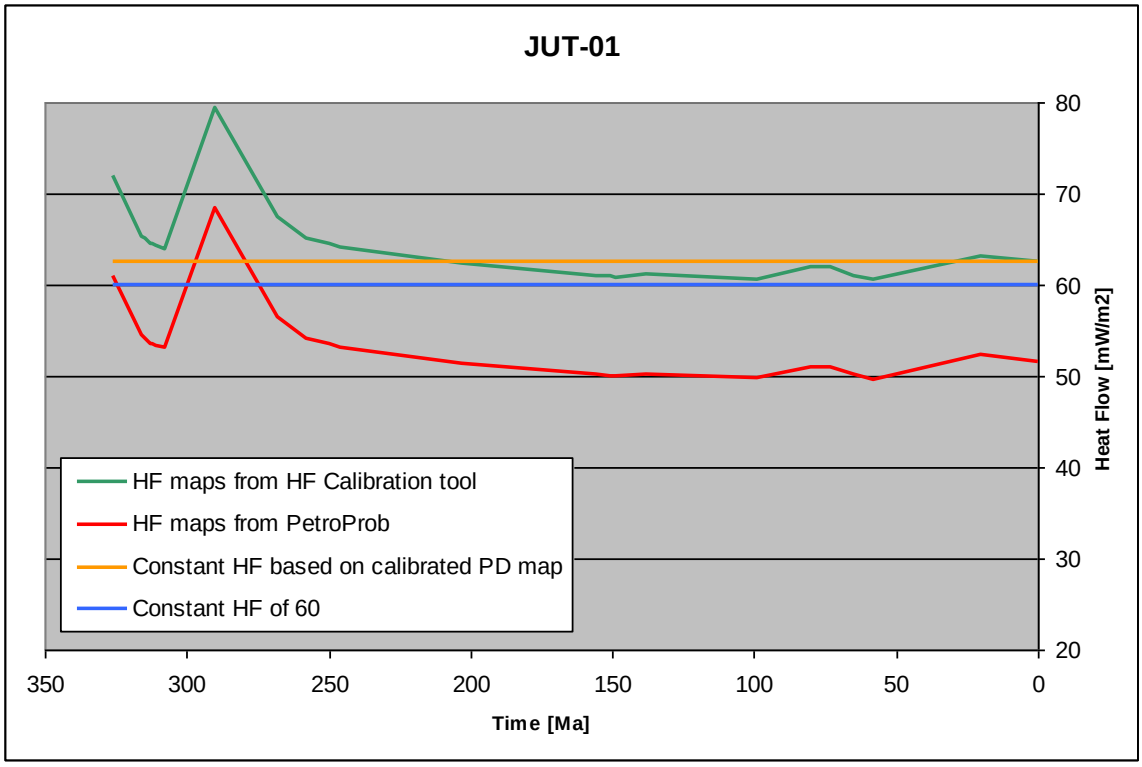
JUT-01
80
70
60
50
40
30
20
Heat Flow [mW/m2]
350
300
250
200
150
100
50
0
Time [Ma]
HF maps from HF Calibration tool
HF maps from PetroProb
Constant HF based on calibrated PD map
Constant HF of 60

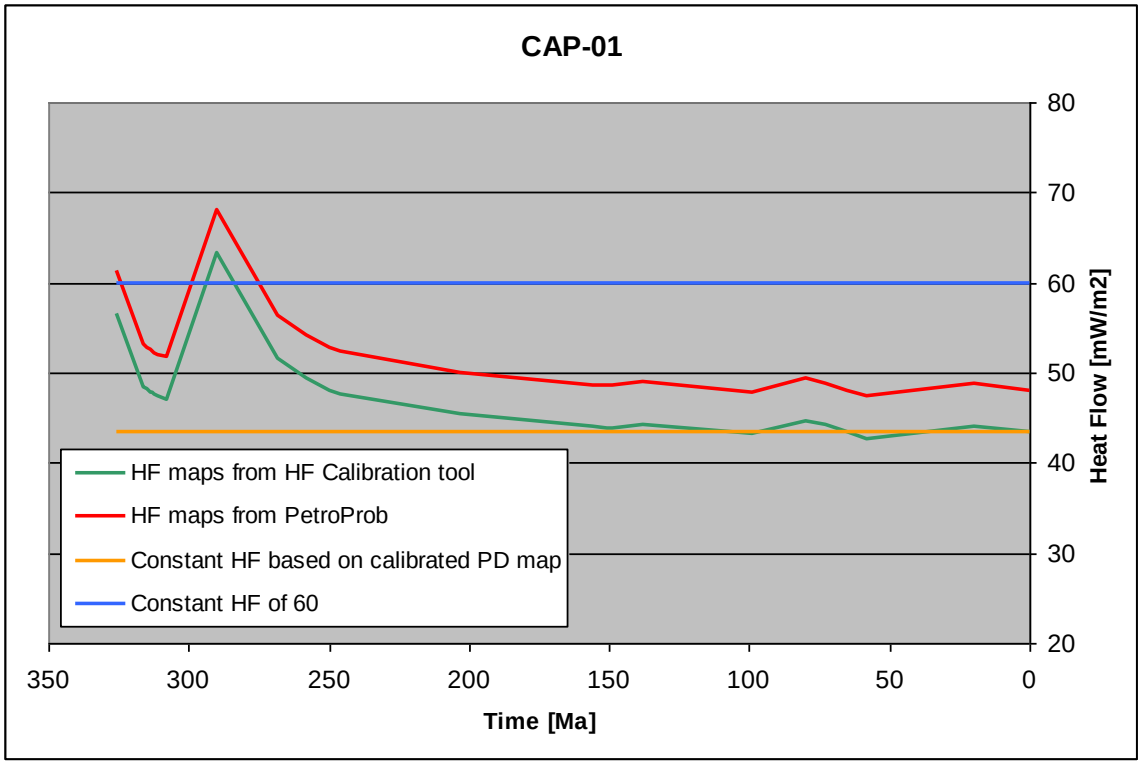

Figure 7a-e Four applied heat flow scenarios at different well locations

3 Work flow

3.1 Modifications of depth maps

The maps of four lithostratigraphic groups were modified and subdivided. This was done to get a more realistic time of deposition and erosion.
The original map of the combined Middle and Lower North Sea Group was subdivided into the Middle and Lower North Sea Group. The upper 15% of the layer were assigned to the Middle North Sea Group and the lower 85% to the Lower North Sea Group. The subdivision is based on average values for these two groups in the Netherlands as taken from detailed stratigraphic interpretation of well logs.

A detailed analysis of well logs in the Roer Valley Graben show that the sediments of Late Cretaceous age, that are still present in the graben, were deposited after the Sub-Hercynian phase and are situated above an unconformity. It was therefore concluded that the Sub-Hercynian inversion had a bigger effect in the Roer Valley Graben than the Laramide phase at the Cretaceous/Tertiary boundary (Luiendijk et al. 2011). To be able to include the correct timing of the Sub-Hercynian inversion phase, the layer of the Late Cretaceous Chalk Group was subdivided into 3 layers, the Ekofisk Formation, the upper part of the Ommelanden Formation and the rest (lower Ommelanden and Texel Formation). The maps of the Chalk Group show a maximum of ~100 m Chalk deposits in the Roer Valley Graben overlying an unconformity. Based on the present-day thickness of the Chalk Group in the Roer Valley Graben and the detailed subdivision of the Chalk Group in wells and from biostratigraphic analyses it was concluded that the Ekofisk Formation can be best described as the uppermost 50 m of Chalk deposits.

The same detailed analyses of logs and biostratigraphic data also show, that Maastrichtian to Santonian sediments sometimes underlie the Danian Ekofisk Formation. It was therefore decided to assign another 50 m to Upper Ommelanden Formation, also deposited after the Sub-Hercynian inversion phase.

In the West Netherlands Basin the influence of the Laramide inversion phase was bigger and no sediments of Campanian to Danian age are preserved. Apart from that it is difficult to tell which layers were eroded in what phase. Along the margins of the West Netherlands Basin the inversion phases did not remove all of the Chalk Group and sediments of Cenomanian age were still found.

The applied method to subdivide the layer uses the top 50 m of the original layer. It cannot distinguish between areas where the top 50 m are of Danian or Cenomanian age. It can therefore be that at the margins of the West Netherlands Basin 100 m of sediments deposited during the Cenomanian were assigned to the Maastrichtian or Danian. This error however can be considered to be smaller than the error that would result from not subdividing the Chalk Group layer.

The last modification results from restrictions of the modeling software. Two erosion phases have influenced the study area (see geological setting) and eroded the same layers at different times. This however is not possible to include into the software.

The Altena Group and Schieland Group layers that were affected by the two erosion phases were therefore subdivided and an erosion map was assigned to each subdivision. The upper,

artificial layers have no thickness at present-day but are considered to be completely eroded during the Jurassic erosion phase.

3.2 Erosions

In total four erosion phases were included into the model (Saalian, Kimmerian, Sub-Hercynian and Laramide). The process of erosion determination is similar for all erosion phases. 1D models were created based on well data and calibrated for temperature and vitrinite reflectance. Erosion values were estimated based on the calibration but also based on the structural setting of the well. A detailed explanation of the method is given in Appendix 1. The erosion maps were then created by creating original thickness maps for each eroded layer. The original thickness of a layer was determined from the present-day thickness maps. On these maps the area of erosion was identified. If the depositional system of the layer was more or less continuous, all areas with less than average thickness were probably eroded. For each layer a cut-off thickness was defined and everything that is thinner than the cut-off was deleted. For those layers where an estimation of erosion from the 1D modeling was available these values were added to the map. Then an interpolation between the values still present on the map was done using Inverse Distance Weighting (IDW, Trend Degree: linear, Trend Radius: 2 grid, Average Radius: 100 grid, Sector Points: 10, Weight Exponent: 2). From the created original thickness maps the present-day thickness was subtracted and negative values set to zero. If the eroded layer is situated stratigraphically underneath another horizon, which was eroded during the same event, the possible area of erosion was set to the area where the overlying layer has zero thickness.

The first erosion phase is the Saalian (Late Carboniferous/Early Permian) erosion phase. In this phase the collapse of the Variscan orogeny caused uplift and erosion of the sediments deposited in the Variscan foreland basin. In the study area the base Permian subcrop map (Figure 8) shows sediments of the Ruurlo Formation to the Hunze Subgroup underlying the base Permian unconformity. The maps included in the model show a similar distribution with the exception of the Hunze Subgroup (Figure 9– Subcrop map based on model). The available depth map of the base of the Permian does not properly fit to the depth map of the Hunze Subgroup and creates a distorted image of the present-day thickness of the layer and therefore of the extent of the erosion. Because of that, the Hunze Subgroup has been excluded from the erosion map building process.

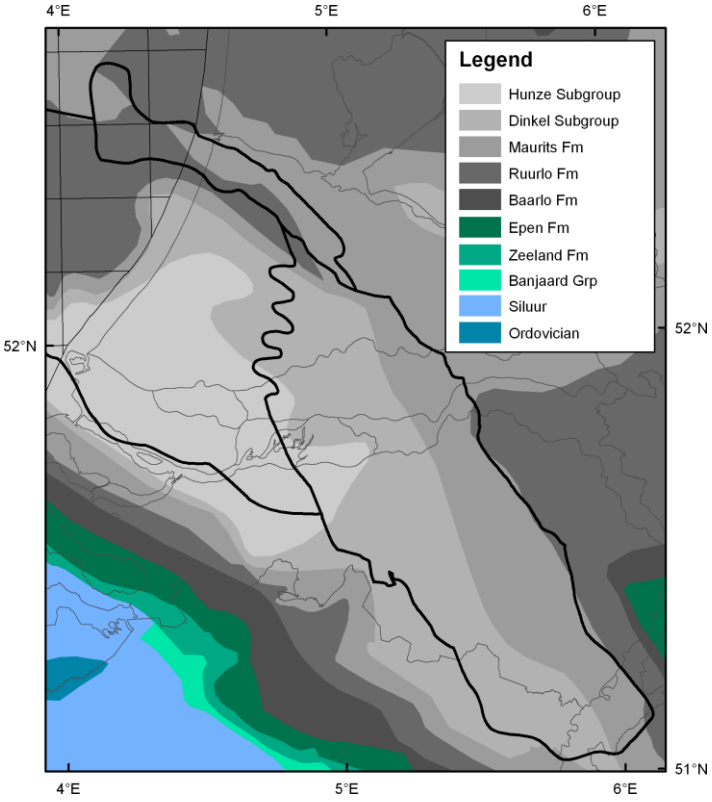

Figure 8 Subcrop map below the Base Permian unconformity (from www.nlog.nl)

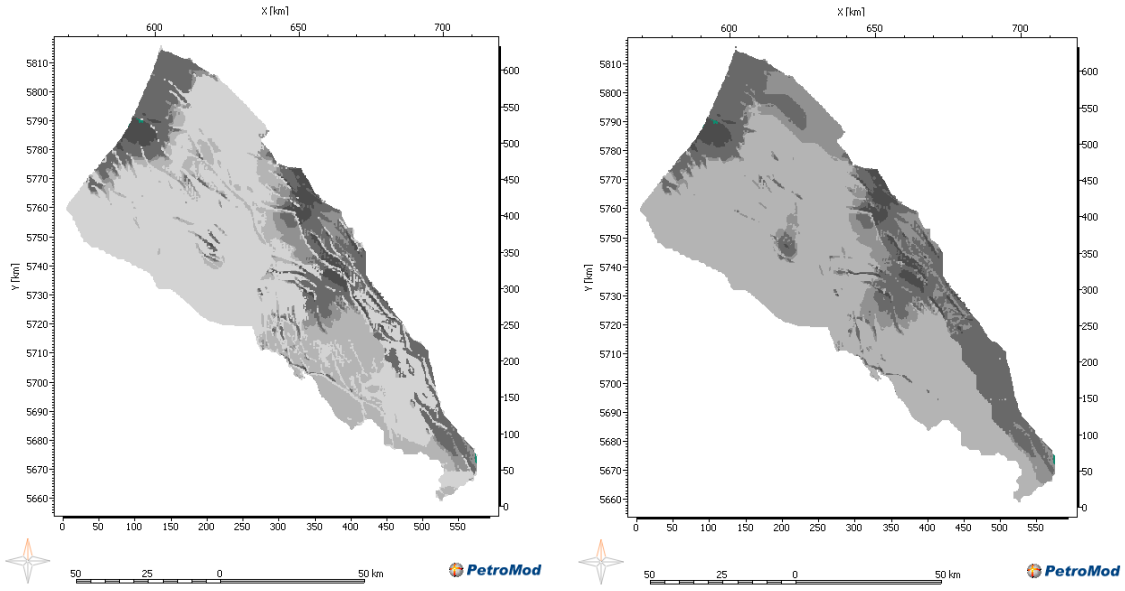

Figure 9 Subcrop map below the Base Permian unconformity in the model. (left) with the Hunze Subgroup, (right) without the Hunze Subgroup. Note the absence of the Dinkel Subgroup below the Hunze Subgroup in the north. For an explanation of the colors see Table 1.

The second erosion phase, related to the Mid- to Late Kimmerian tectonic phase, occurred at the end of the Jurassic and affected mostly the platform and high areas (Figure 10). Since at least two layers were affected by this and the third, the Late Cretaceous erosion phase, it was difficult to determine the amount of erosion for the individual phases. It was decided to reduce

the area of Jurassic erosion to the structural highs and platforms and the southern Roer Valley Graben and assume that everything within the basin was removed during the Late Cretaceous inversion.

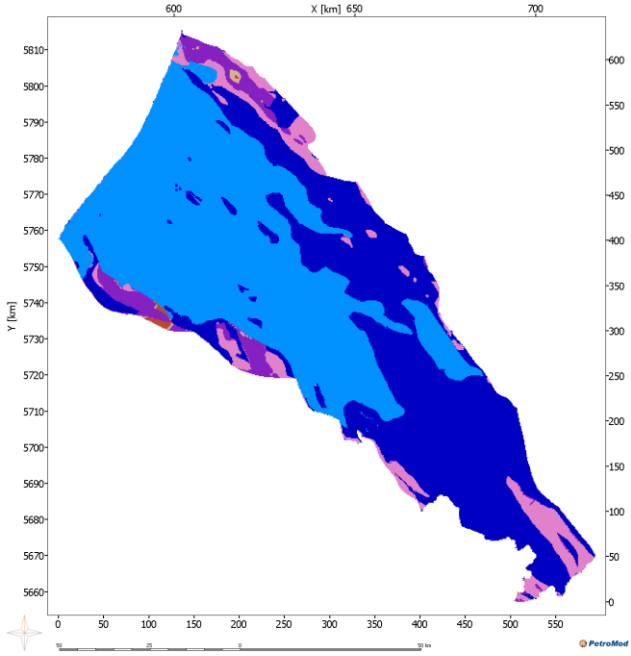

Figure 10 Subcrop map below the Mid- to Late Kimmerian unconformity. For an explanation of the colors see Table 1.

The most important erosion event is the Late Cretaceous inversion (Figure 11). The inversion and subsequent erosion is related to the collision of the African plate with the Eurasian plate. The compressive movements caused reverse reactivation of normal faults, doming of larger areas (De Jager, 2003). These movements happened in distinct pulses which influenced different areas differently.

In the Roer Valley Graben the first inversion pulse during the Campanian, the so called Sub-Hercynian event, had the most influence, which can be seen from well logs. In the West Netherlands Basin a distinction between these two events is difficult because no Danian or Late Cretaceous sediments are preserved. Therefore it was assumed that the Sub-Hercynian event also eroded most of the sediments while the Laramide event affected only the Danian deposits.

A fifth phase of erosion, the Pyrenean phase that occurred during the Late Eocene, was not included in the model. During this phase Paleocene and Eocene sediments were eroded in the area of the WNB. The erosion phase had no influence on the RVG (De Jager, 2003). It was not included into the modeling because of the rough subdivision of the Lower and Middle North Sea Group layer (Chapter 3.1). Since this subdivision is not based on seismic interpretation, it is not possible to determine the area affected by the erosion. In addition, the amount of erosion that occurred during this time is believed to be limited and not exceeding present-day or Late Cretaceous burial. It therefore does not influence the determination of the burial anomaly.

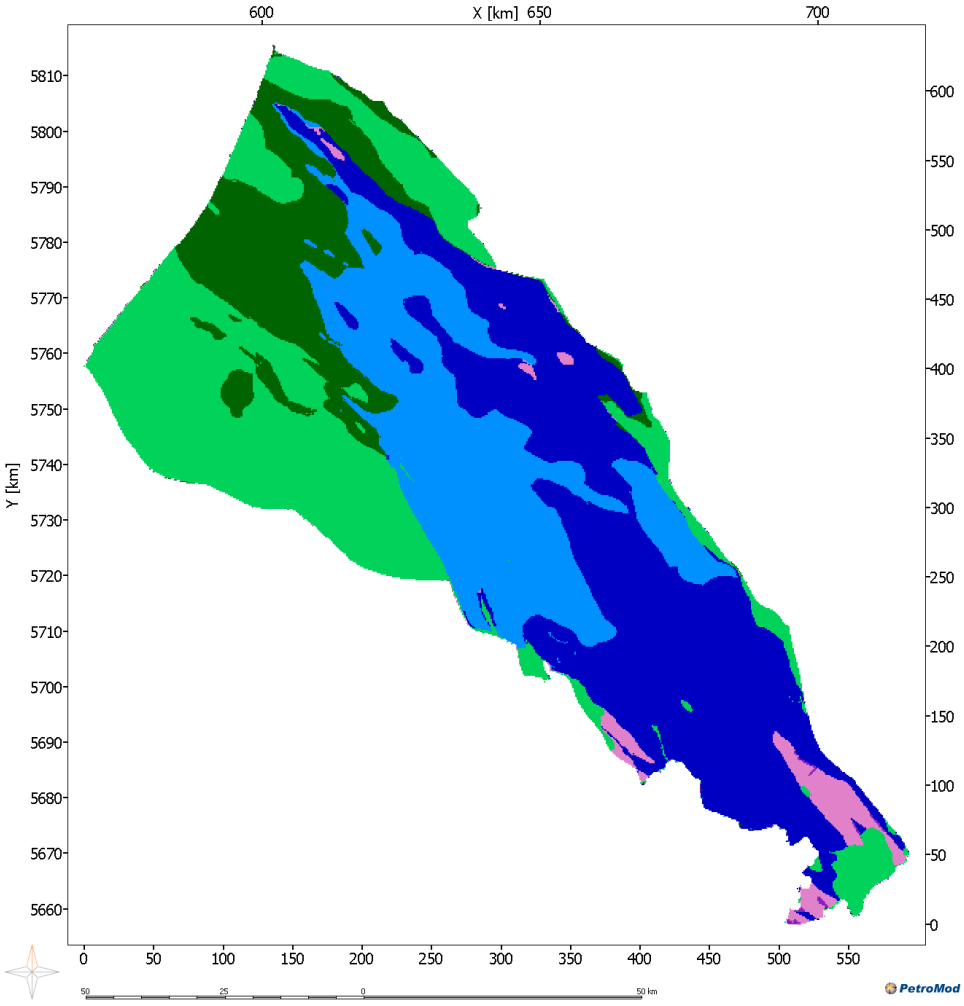

Figure 11 Subcrop map below the Subhercynian unconformity. For an explanation of the colors see Table 1.

3.3 Calibration to Porosity

To be able to model porosity and permeability of the sand and shale layers a calibration to measured values was performed. To adjust the mechanical compaction curve (porosity vs depth) to better fit the measured values, a user-defined porosity-depth curve needs to be defined. For this curve a total of 790 porosity values were available in the study area. These are average values of measured porosity in different wells per stratigraphic layer. Based on the lithological description of the individual stratigraphic layers of Van Adrichem Boogaert and Kouwe (1993) an average lithology was assigned to each measurement. The X-error was estimated based on the calculated P10 and P90 values as well as a Y-error, based on the length of the interval over which the average value was determined. The measured depth of each value was corrected for true vertical depth based on the well deviation report and wells situated in the projected area with burial anomaly were excluded from the creation of the adjusted porosity-depth curve.

One problem that occurred is due to the rough lithological description for the measurements. The average lithology does not always reflect the true composition of the layer at the drilled position. The actual lithology of the measurement might be more shaly or more sandy than

other measurements with the same description. This makes the definition of a porosity-depth trend difficult because the resulting graph looks more like a cloud than a line (Figure 12).

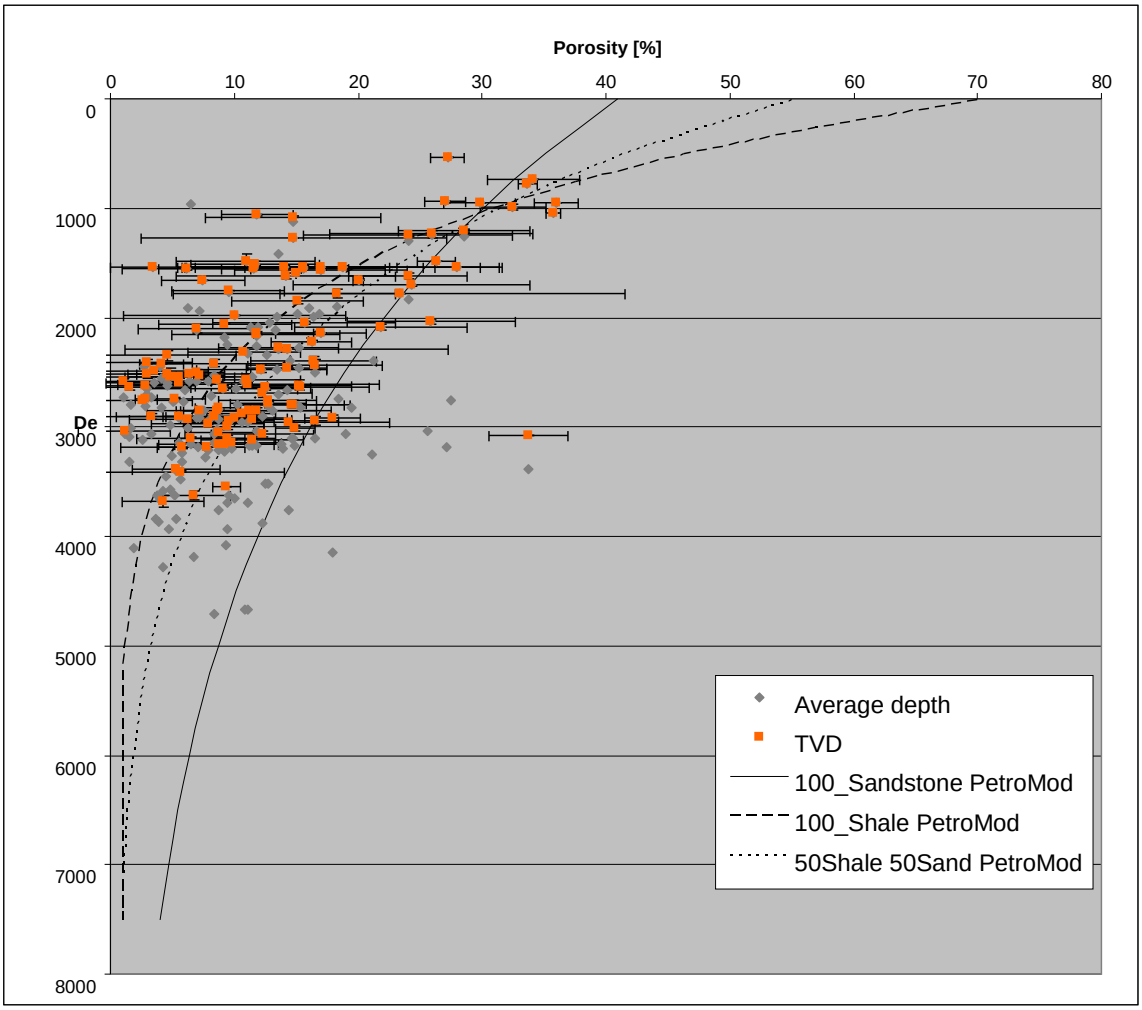

Figure 12 Measured average porosity for layers with a pure sandstone description

To be able to determine a trend line for shale and for sandstone the measurements were filtered using the X- and Y-error. The X-error describes the total spread of measurements that were included in the average value. To reduce the error introduced by averaging values measured in very different lithologies the X-error value was set to a maximum of +/-5 % porosity. The Y-error describes the length of the interval that was included into the average value. As porosity decreases with depth the average porosity value of a long interval does not give a good representation of the actual porosity. The Y-error value was therefore set to a maximum of 10 m. The set of values with the description “75% Sand and 25% Shale” gave the best trend line for both lithologies, sand and shale (Figure 13). The inclusion of net/gross as indicator for sandstone/shale relationship could have helped in the determination of the porosity depth relationship by giving a better description of the real lithology. This will be included in further studies.

Another issue with the porosity is the exclusion of chemical compaction and cementation in the model. The measured values are probably influenced by chemical compaction and cementation as well as mechanical compaction. By including only one mechanism

(mechanical) in the modeling, areas strongly influenced by other mechanisms cannot be calibrated. The definition of a custom porosity depth relationship will however cover the average amount of porosity reduction caused by chemical compaction and/or cementation.

Figure 13 also shows the new adjusted mechanical compaction curves for pure sand and pure shale based on the trend observed in the measurements. The original pure sand and pure shale lithologies of PetroMod were modified with these new mechanical compaction curves. Using the modified lithologies, new mixed lithologies were created and applied to the model.

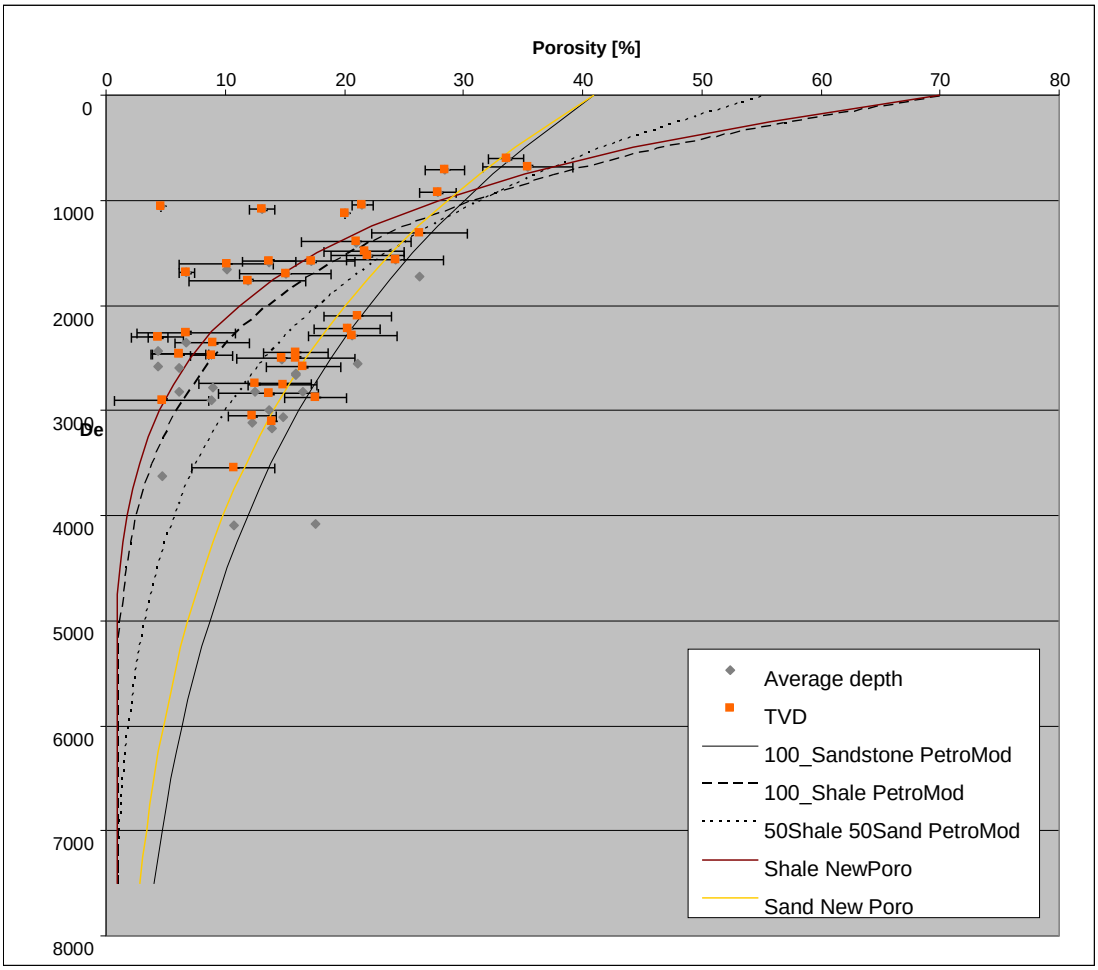

Figure 13 Measured average porosity for layers with an average lithology of 75% Sand and 25% Shale, porosity depth curve of the PetroMod standard lithologies Sand, Shale and a mix with 50% Sand and 50% Shale and modified Sand and Shale porosity depth curves based on measurements

4 Results

4.1 Burial history

The burial history of the 3D model was reconstructed and calibrated to vitrinite reflectance, temperature and porosity values. The results presented here are based on the fourth heat flow scenario, using the modified PetroProb maps as they gave the best calibration results.

The burial history of the area is presented using two 2D cross sections, one running SW to NE crossing the West Netherlands Basin and one running NW-SE, along the Roer Valley Graben (Figure 14, Figure 15, Figure 20). Along these sections two wells were selected, one at each end of the section, to present the differences in burial history and the temperature, vitrinite reflectance and porosity calibration.

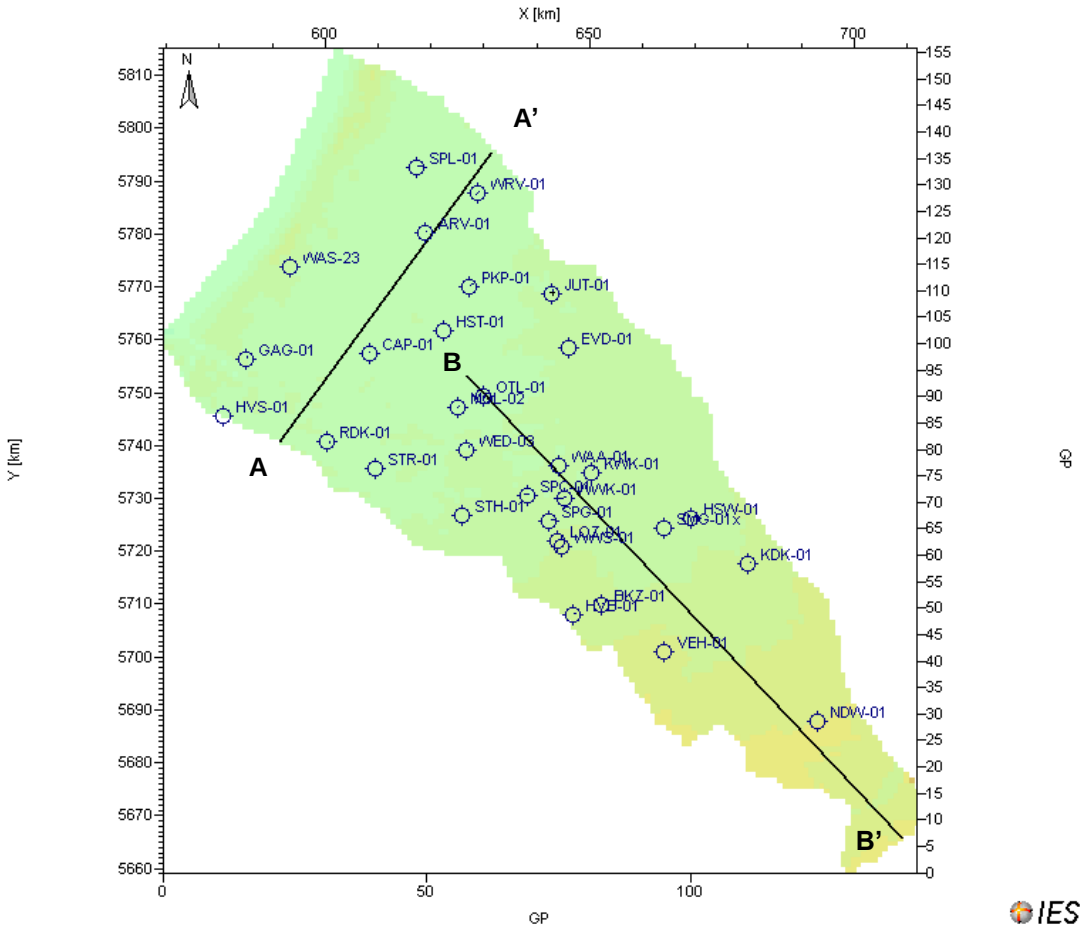

Figure 14 Position of the 2D sections

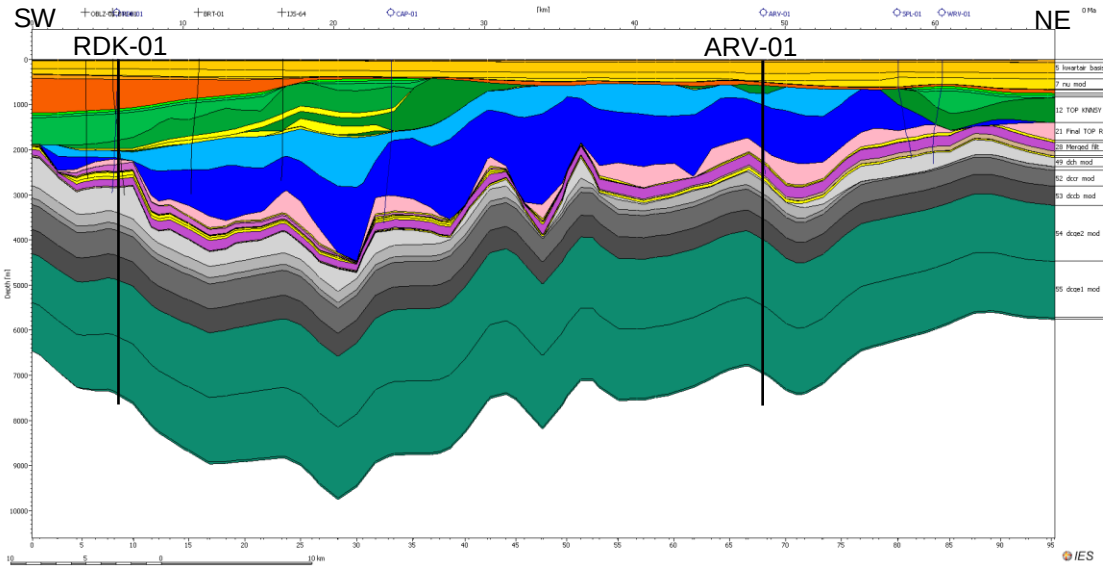

Figure 15 2D extraction A-A' through the West Netherlands Basin from SW to NE. For the position of the section see Figure 14. For an explanation of the colors see Table 1

2D section A-A' is situated in the West Netherlands Basin, crossing the main structures from SW to NE (Figure 15). The inverted basin is visible in the center of the section, clearly defined by the missing Cretaceous sediments and the thinned Lower Tertiary succession. Most erosion occurred along the northeastern border of the basin. This can also be seen in the burial history diagrams of the wells. Well RDK-01 situated in the southeast has deepest burial at present day and Cretaceous and Early Tertiary sediments are present in the stratigraphic succession (Figure 16, Figure 17).

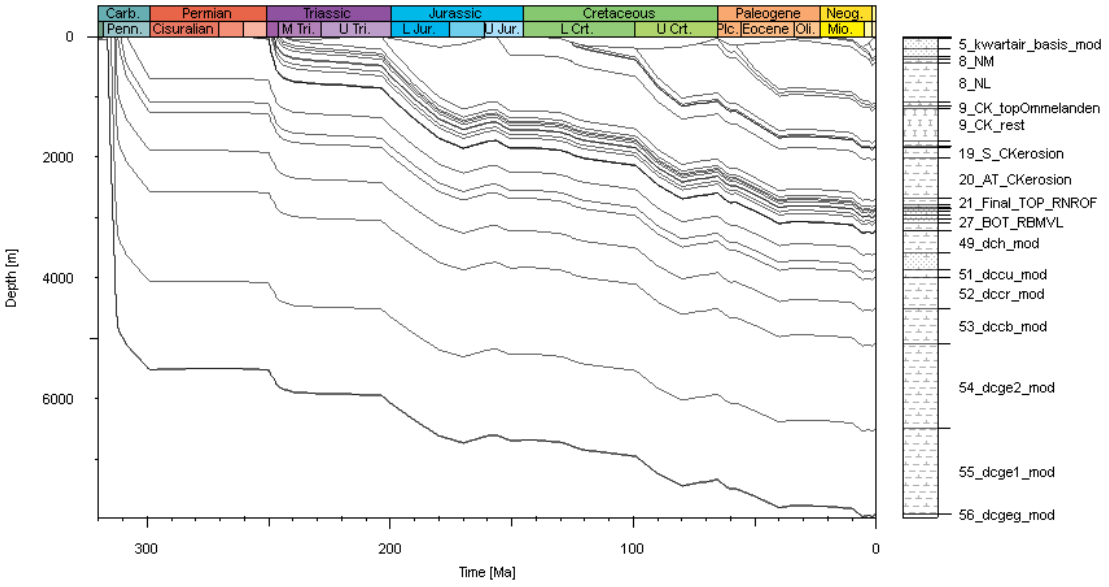

Figure 16 Burial history plot of well RDK-01, situated in the western part of the West Netherlands Basin. For the position of the well see Figure 14 and Figure 15

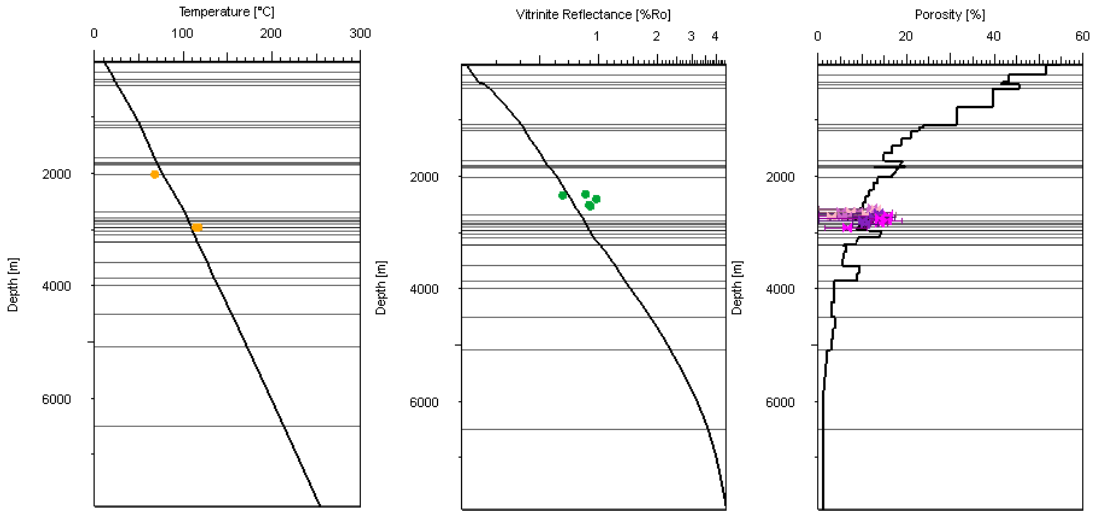

Figure 17 Temperature, Vitrinite reflectance and Porosity calibration of well RDK-01

On the other hand, well ARV-01 situated in the northeast has experienced significant erosion and deepest burial during the Late Cretaceous (Figure 18). Only a thin layer of Early Cretaceous sediments can be found in the stratigraphic succession, the Late Cretaceous sediments are completely missing and the Lower Tertiary is very thin. The influence of the erosion on the temperature evolution as indicated by vitrinite reflection can be seen in Figure 19, where a jump in modeled vitrinite reflectance is seen at about 500 m depth.

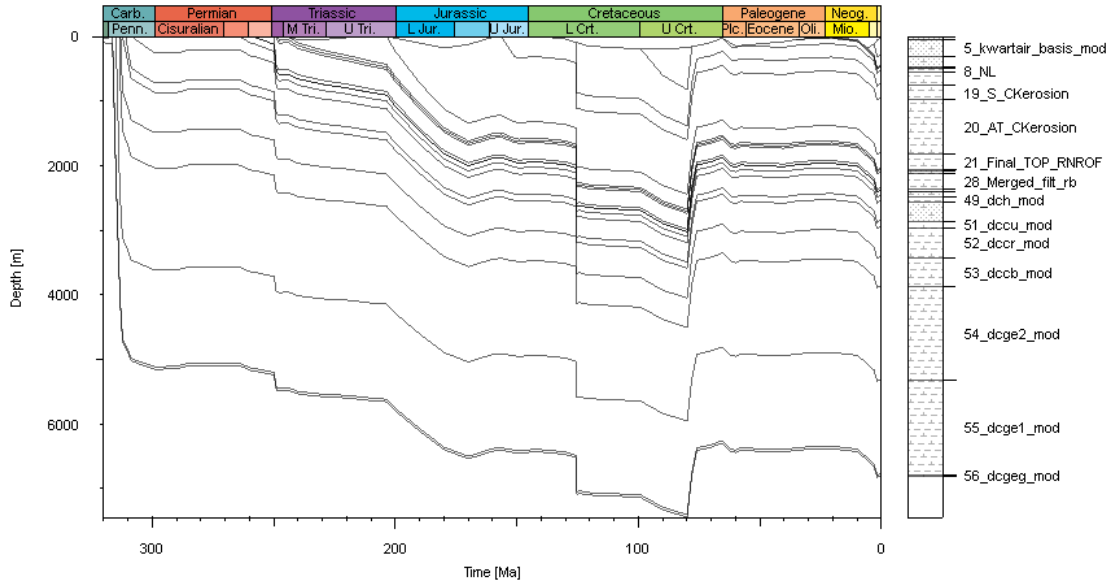

Figure 18 Burial history plot of well ARV-01, situated in the eastern part of the West Netherlands Basin. For the position of the well see Figure 14 and Figure 15

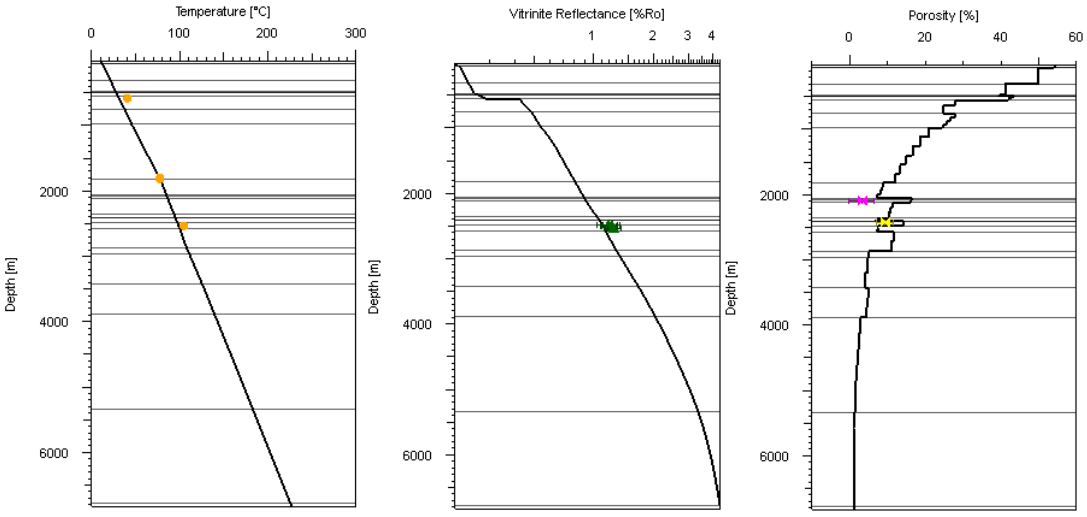

Figure 19 Temperature, Vitrinite reflectance and Porosity calibration of well ARV-01

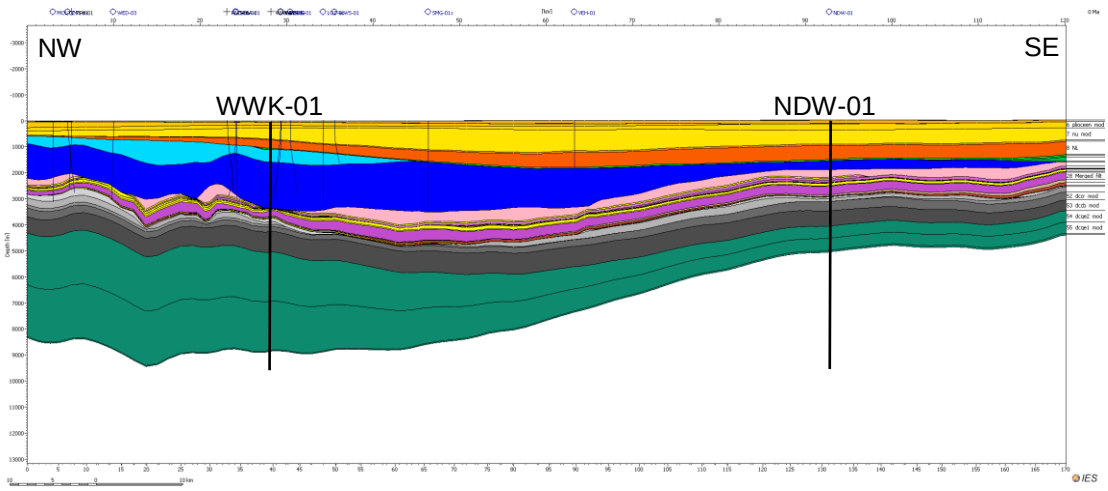

Figure 20 2D extraction B-B' through the Roer Valley Graben from NW to SE. For the position of the section see Figure 14. For an explanation of the colors see Table 1

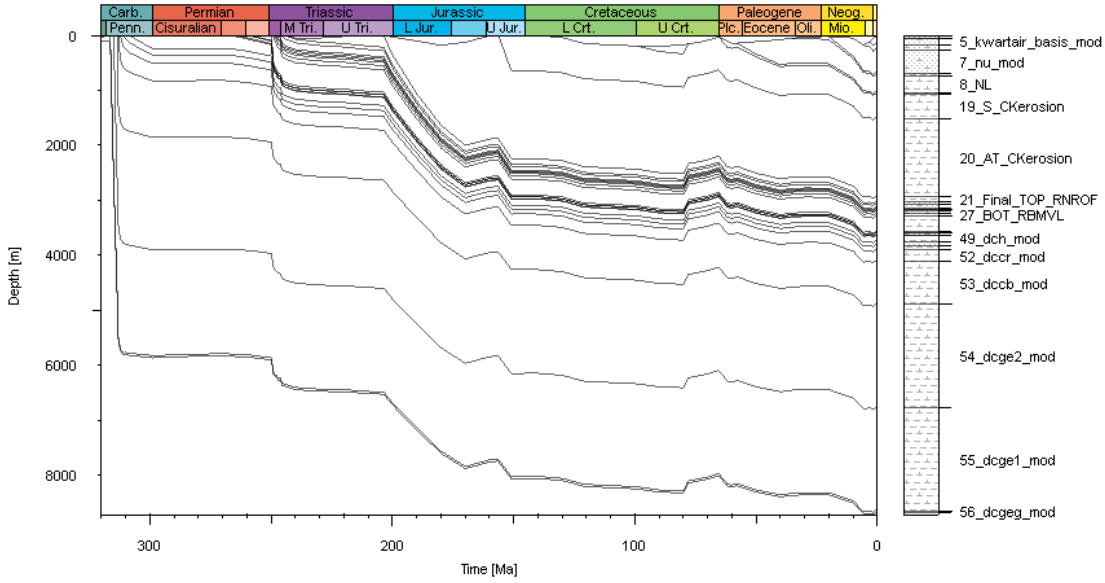

Figure 21 Burial history plot of well WWK-01, situated in the northern part of the Roer Valley Graben. For the position of the well see Figure 14 and Figure 20

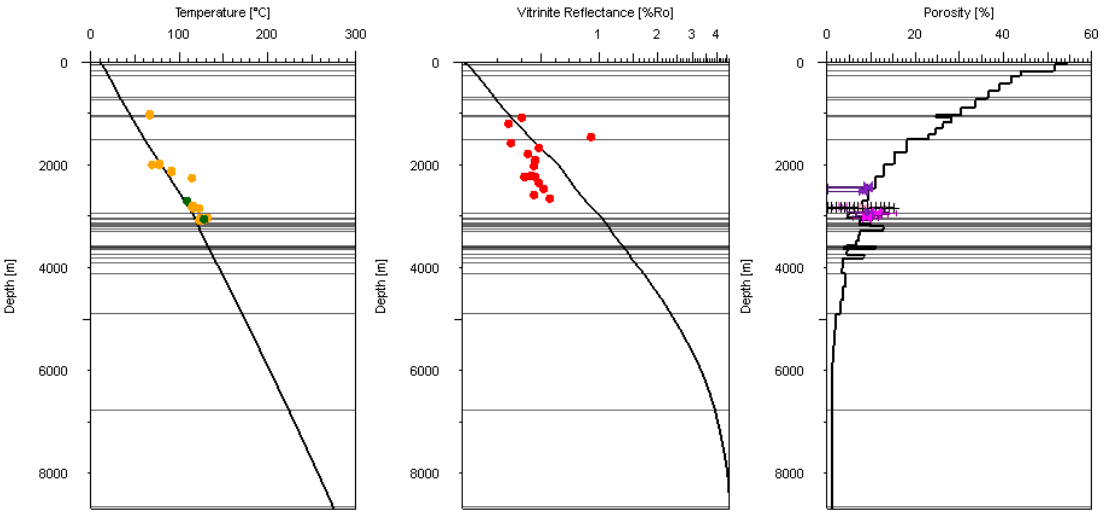

Figure 22 Temperature, Vitrinite reflectance and Porosity calibration of well WWK-01

The 2D section in the Roer Valley Graben runs from the NW to the SE along the length of the graben (Figure 20). The unconformity underneath the Tertiary is very visible, cutting into increasingly older sediments towards the southeast. Two erosion phases are represented by this unconformity, the Late Cretaceous inversion and the Late Jurassic uplift. In the southernmost part of the section, a thin layer of Cretaceous sediments is present, subdividing the two erosion phases. Due to the absence of a subdividing layer in the rest of the area, it is difficult to estimate how much sediment was deposited and eroded during the two phases.

Deepest burial in the Roer Valley Graben is almost everywhere at present-day. However in the northwest of the graben, the depth did not vary a lot since the Late Jurassic (Figure 21). Tertiary burial amounts to about 500 m of sediment. In the southeast of the graben Tertiary sediments are twice as thick, burial in the Tertiary was therefore faster (Figure 23). The temperature and maturity calibration is difficult in the Roer Valley Graben (Figure 22). In the

northwest several wells with vitrinite reflectance and temperature measurements are available; however the quality of the vitrinite reflectance measurements is questionable. In this area deepest burial is present-day, and the calibration of maturity and temperature is not possible because the measured vitrinite reflectance values are too low to be calibrated using the measured present-day temperatures which are deemed more reliable. One possible explanation is that the present-day temperature is not equilibrated due to Pleistocene cooling or that large scale fluid flow influences the system. In the south east only one well with temperature and vitrinite reflectance measurements of varying quality is available for calibration (NWD-01, Figure 14, Figure 23). In this well high vitrinite reflectance values were measured in Carboniferous rocks, which can be related to large scale erosion and/or abnormal past-temperatures in the area (Figure 24).

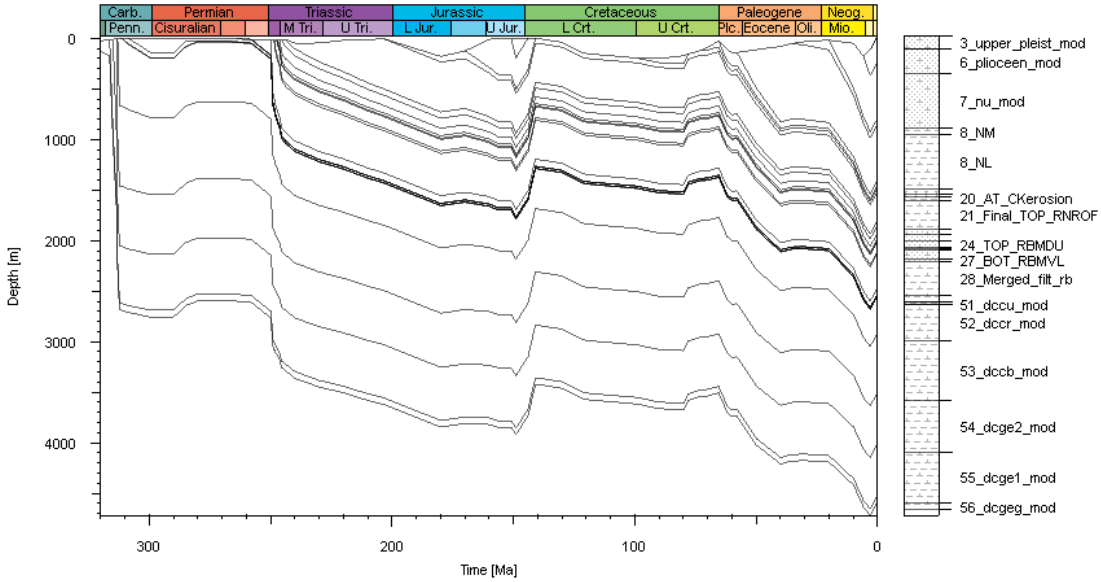

Figure 23 Burial history plot of well NDW-01, situated in the southern part of the Roer Valley Graben. For the position of the well see Figure 14 and Figure 20

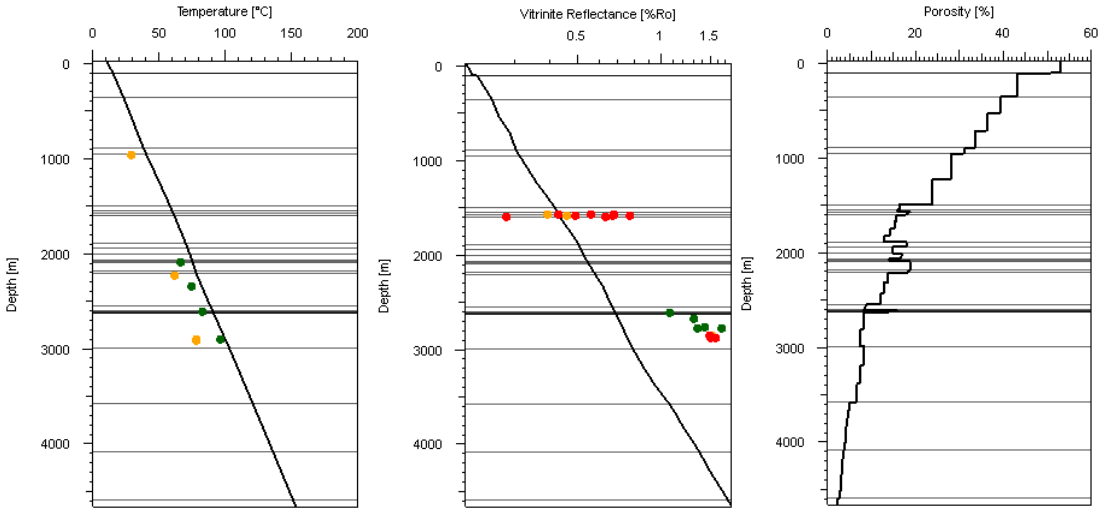

Figure 24 Temperature, Vitrinite reflectance and Porosity calibration of well NDW-01

4.2 Erosion reconstruction

4.2.1 Cretaceous

The erosion maps were created by interpolation between the areas estimated to have not experienced erosion and the well locations for which an estimate of erosion was available (Appendix 1, Worum, 2004). Using this technique the Late Cretaceous Chalk Group was estimated to have been eroded in most of the study area. Reconstructed pre-erosion thicknesses are in the range of less than 100 m to ~600 m (Figure 25). Underneath the Chalk Group the Early Cretaceous Rijnland Group was eroded. The Rijnland Group, situated underneath the Chalk Group was assumed to have not been deposited in the south of the model. Reconstructed erosion values go up to 550 m in the northeast of the model. The Late Jurassic Schieland Group was assumed to have been deposited in the whole study area. It is assumed that in the south the Schieland Group was already eroded in the Late Jurassic. Vitrinite reflectance and fission track measurements in the south of the Roer Valley Graben show high paleo-temperatures in the Middle to Late Jurassic (see chapter 5.5). The reconstructed erosion values for the Schieland Group vary between 0 and 600 m. The highest erosion values occur along faults in the western part of the study area. The Altena Group was significantly eroded during the Middle to Late Jurassic, however along big faults in the western part of the study area, large scale erosion with values of up to 1200 m also occurred during the Late Cretaceous.

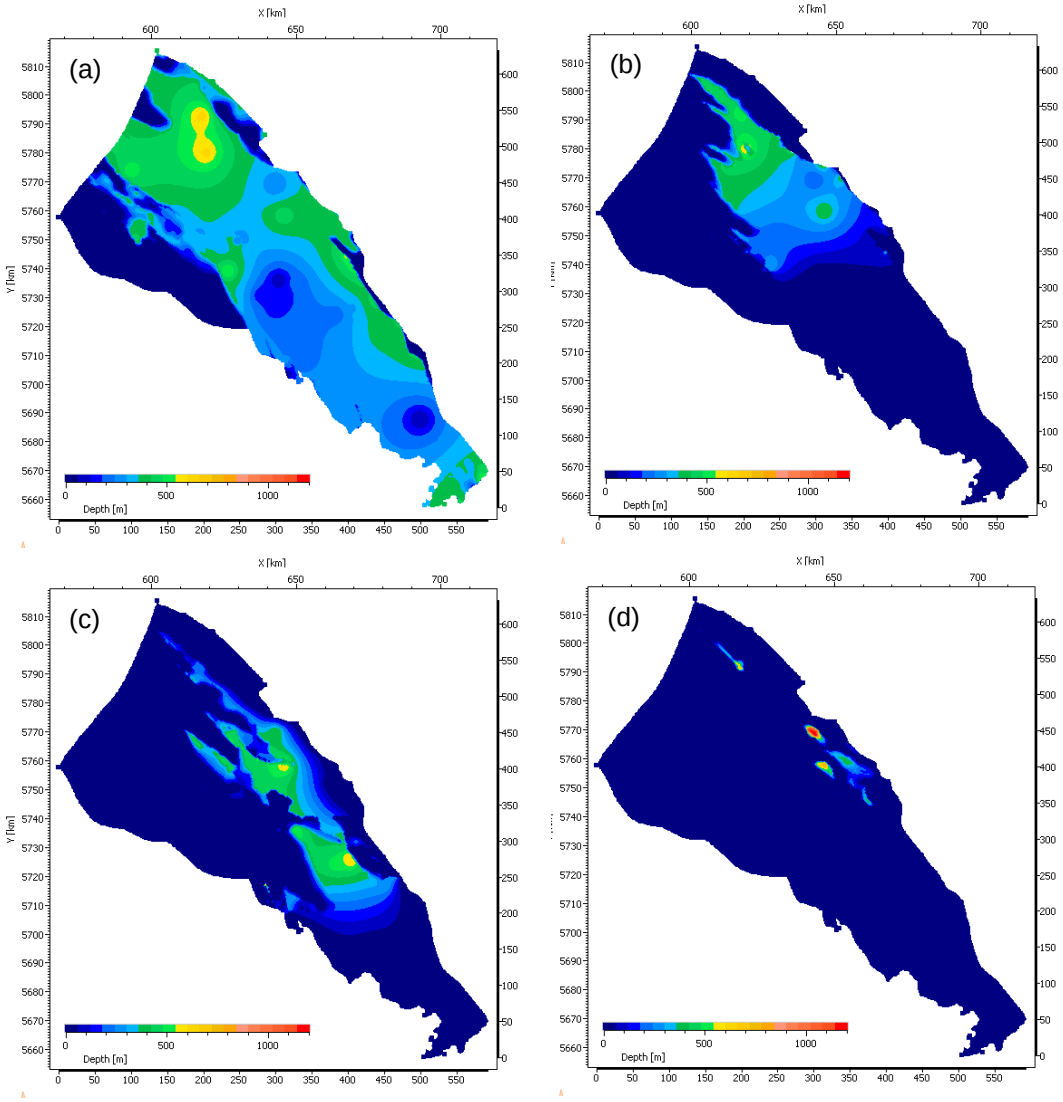

Figure 25 Erosion maps of the Subhercynian erosion of the Chalk (a), Rijnland (b), Schieland (c) and Altena Group (d)

4.2.2 *Jurassic*

The Schieland and Altena Group, but also the Upper Germanic Trias Group, were eroded during the Middle to Late Jurassic. This erosion was localized along the margins of the basins and in the south of the Roer Valley Graben. For this erosion phase three scenarios were created, one low erosion scenario with average erosion values of around 200 m (Figure 26), one high erosion scenario with an initial thickness of the Schieland Group of 300 m, erosion of the Altena Group of up to 1000 m and Upper Germanic Trias Group erosion of up to 400 m (Figure 27) and based on fission track scenarios, the third scenario, with erosion of the Schieland and Altena Groups on the platform areas during the Jurassic but continuous deposition in the Roer Valley Graben until the Late Cretaceous and erosion of the Schieland and Altena Group during the inversion (Figure 28). These scenarios are based on vitrinite reflectance and fission track measurements analysed in well NWD-01 in the south of the Roer Valley Graben.

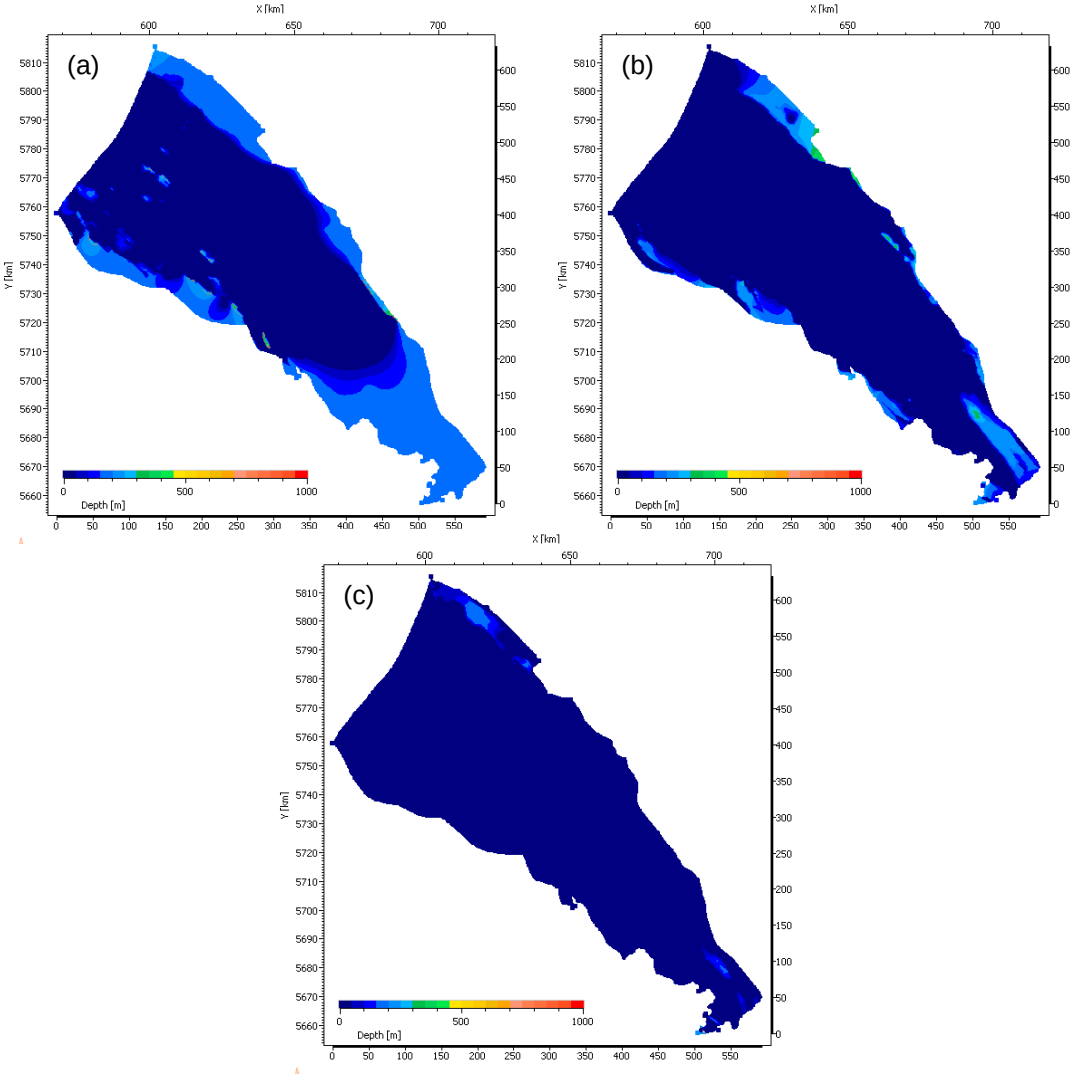

Figure 26 Erosion maps of the Middle to Late Jurassic erosion of the Schieland (a), Altena (b) and Upper Germanic Trias Group (c) of scenario 1

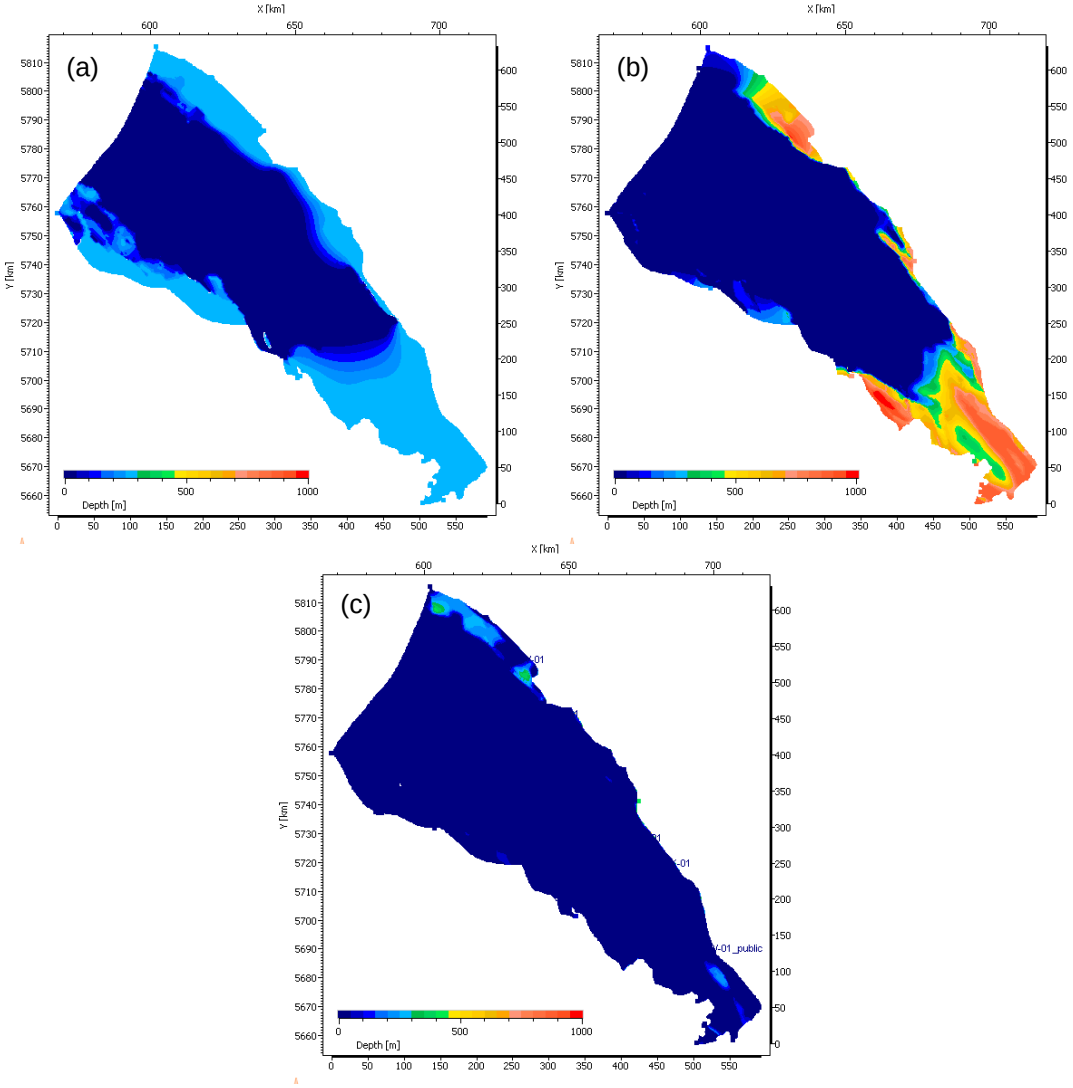

Figure 27 Erosion maps of the Middle to Late Jurassic erosion of the Schieland (a), Altena (b) and Upper Germanic Trias Group (c), assuming higher erosion values of scenario 2

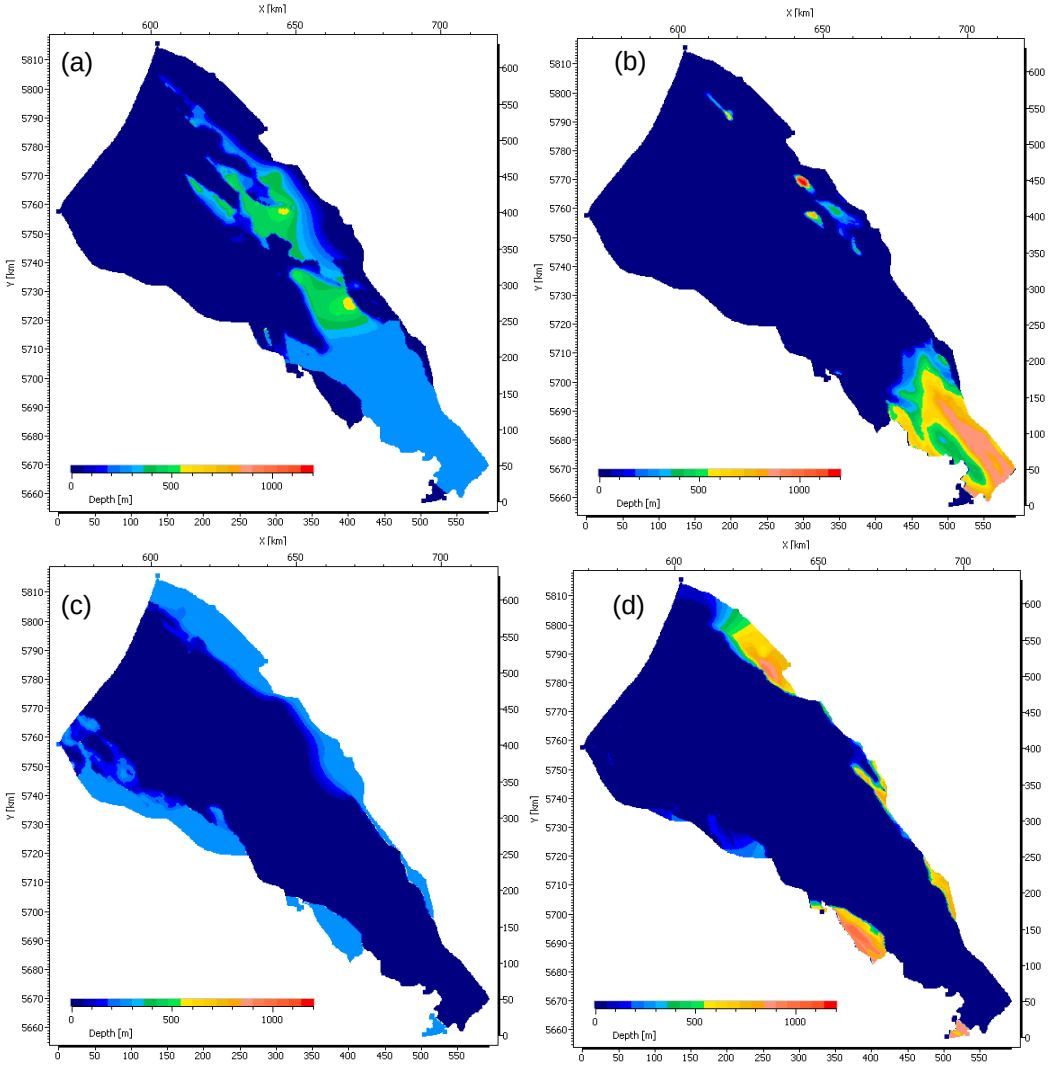

Figure 28 Erosion maps of the Schieland (a, c) and Altena (b, d) Formation for the Cretaceous (a, b) and the Jurassic (c, d) erosion phase of scenario 3

4.2.3 *Jurassic erosion in the Roer Valley Graben 1D models and fission track measurements*

In the southern part of the Roer Valley Graben only one well had maturity measurements as calibration for the model (NWD-01). These vitrinite reflectance measurements show very high, reliable values in rocks of Carboniferous age. Furthermore measurements were done on Lower Jurassic rocks that show a very large scatter but generally lower values. Present-day temperature measurements show a normal to low present-day temperature distribution. Based on these measurements three different erosion scenarios are possible, deep burial and erosion at the end of the Carboniferous, deep burial and erosion during the Late Jurassic or continued deep burial and erosion during the Late Cretaceous. To test these scenarios four 1D models were created based on an extraction from the 3D model. The first model uses the low erosion scenario from the 3D model which fits the Jurassic vitrinite reflectance measurements but not the Carboniferous ones (Figure 29). The second model assumes a very deep burial (1850 m) from Early Jurassic until Late Cretaceous and rapid erosion at the end of the Late Cretaceous. Together with an enhanced heat flow of around 80 mW/m^2 this model was able to fit the Jurassic and the Carboniferous measurements (Figure 30).

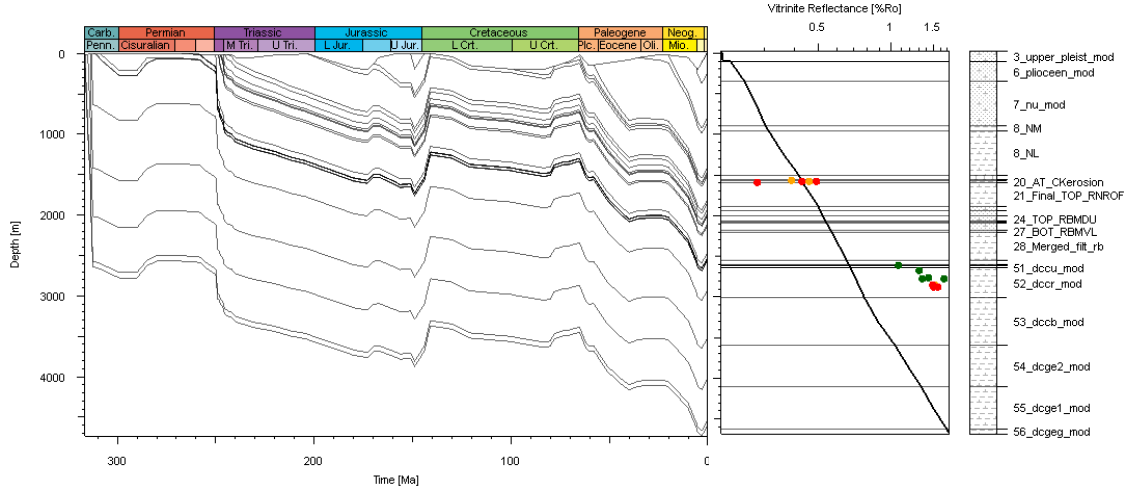

Figure 29 Burial history and maturity calibration of well NDW-01 as extracted from the 3D model

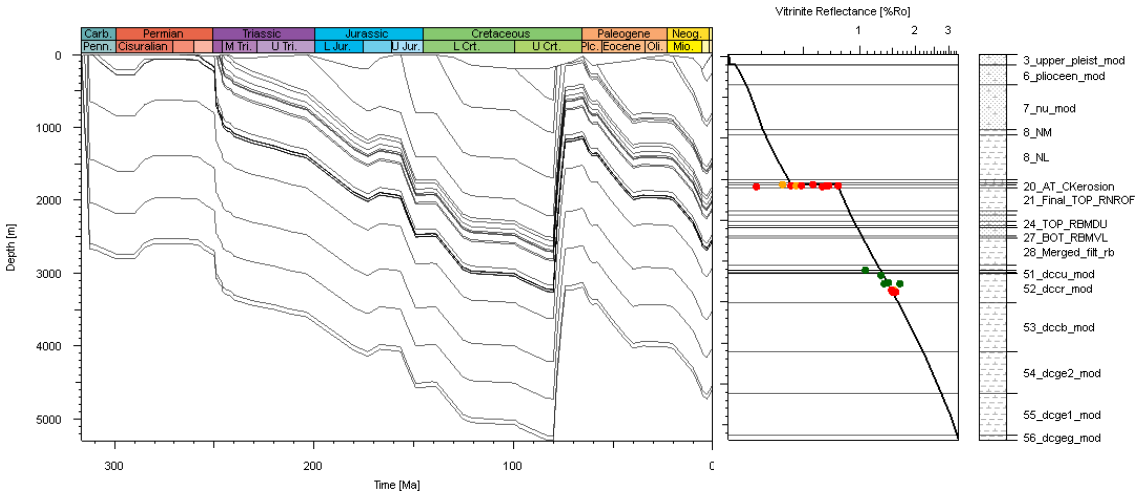

Figure 30 Burial history and maturity calibration of well NDW-01 with 1850 m erosion during the Late Cretaceous and elevated heat flow of 80 mW/m2 during the Late Jurassic

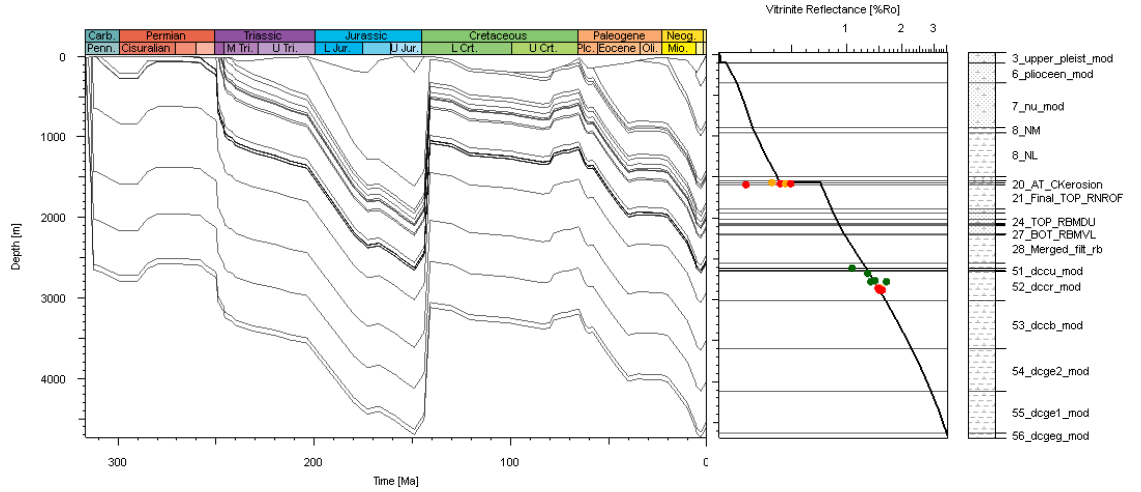

Figure 31 Burial history and maturity calibration of well NDW-01 with 1400 m erosion and elevated heat flow of 80 mW/m2 during the Late Jurassic

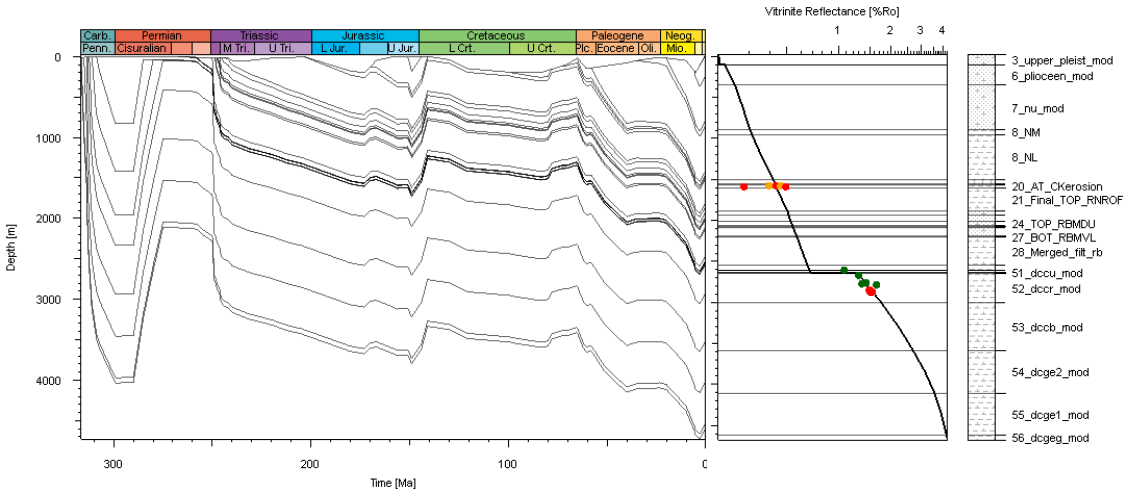

Figure 32 Burial history and maturity calibration of well NDW-01 with 1500 m erosion during the Late Carboniferous and elevated heat flow of 105mW/m2

The third model uses 1400 m of erosion during the Jurassic and high basement heat flow values of 80 mW/m^2. This combination was able to calibrate all data points (Figure 31). The fourth model assumes deep burial in the Carboniferous and subsequent erosion (1500 m) along with high heat flows of 105 mW/m^2. This scenario was also able to calibrate all data points (Figure 32).

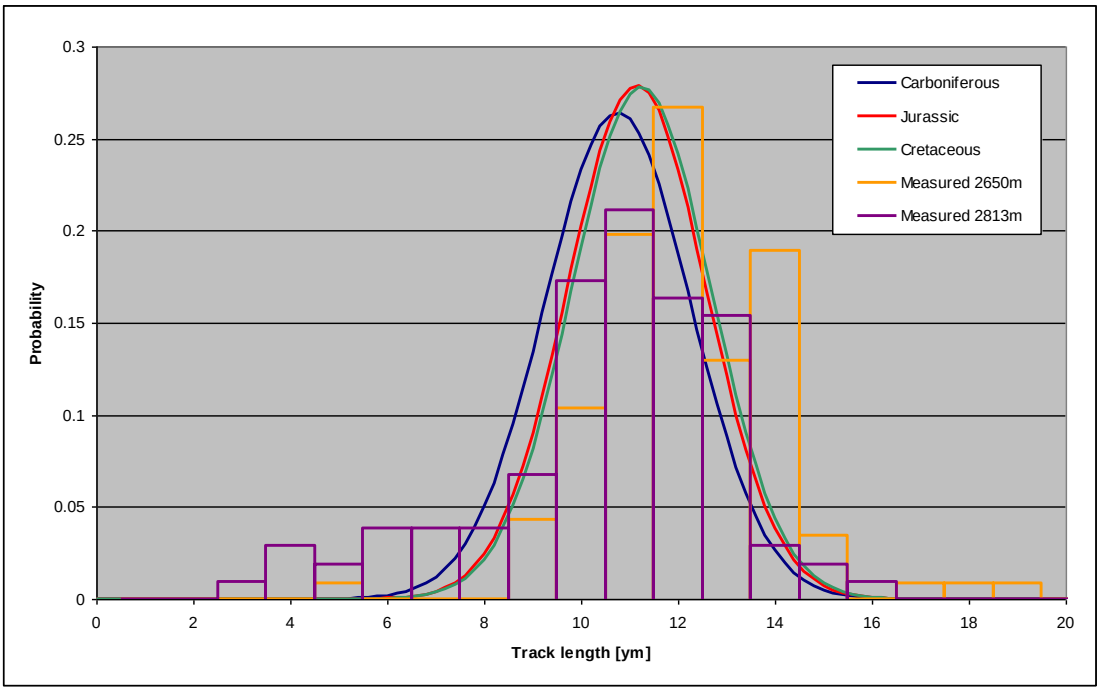

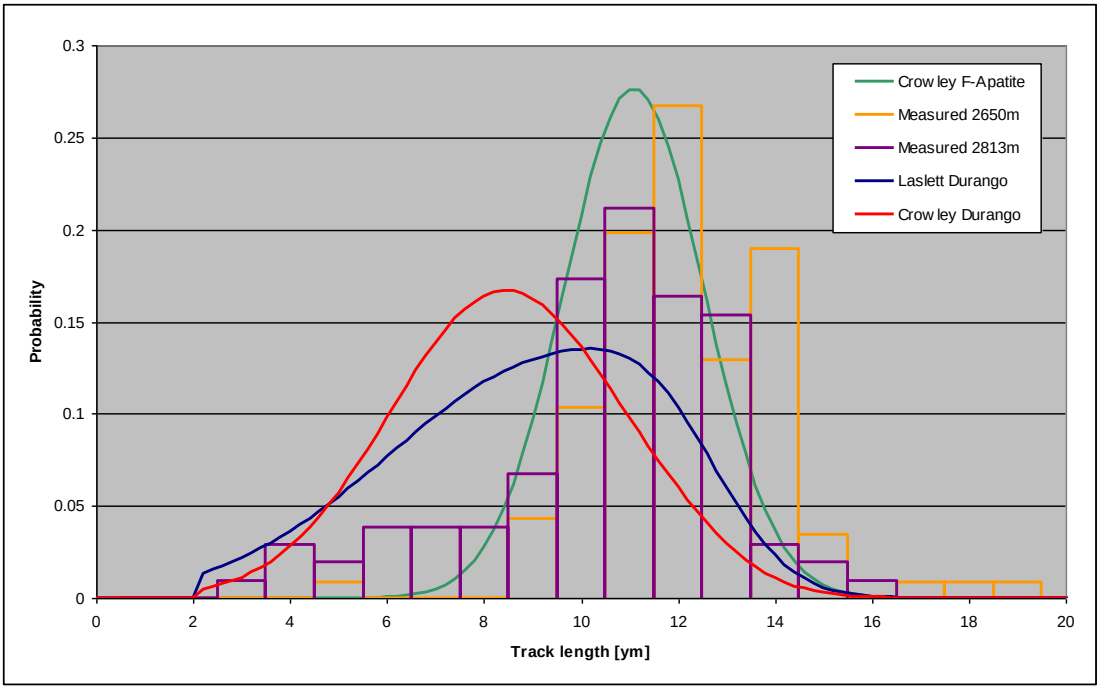

Figure 33 Fitting of calculated apatite fission track length distribution with measured values for (a) different burial histories and (b) different calculation models

To distinguish between the model with Carboniferous deep burial and erosion, Jurassic deep burial and erosion and Cretaceous deep burial and erosion, fission track measurements were used (Green and Moore, 1992). Sandstone samples were taken from the well and measured for two depths in the Carboniferous (Table 3). Using the fission track calculation tool of PetroMod (PetroTracks®) the fission track length distribution and mean track length and age were calculated for the three erosion scenarios using different calculation methods. The Crowley F-Apatite method showed the best fit with the measured length distribution (Figure 33) and the Jurassic and Cretaceous models showed the best fit with measured age and mean track length.

Table 3 Measured apatite fission track length and age compared to calculated length and age using different models and burial histories

Measurement	Model	Depth [m]	Age [Ma]	Mean track length [ym]
GC393-13		2650	103.4 +/- 10	11.51 +/- 0.18
GC393-14		2813	59.8 +/- 6.6	10.02 +/- 0.25
3D extraction	Crowley F-Apatite	2641	209.8	10.7 +/- 1.5
1850 m Cretaceous and high HF	Crowley F-Apatite	2641	59.4	11.2 +/- 1.4
1400 m Jurassic and high HF	Crowley F-Apatite	2641	106.9	11.1 +/- 1.4
1500 m Carboniferous	Crowley F-Apatite	2641	194.4	10.8 +/- 1.5
1400 m Jurassic and high HF	Crowley Durango	2641	50.4	8.5 +/- 2.3
1400 m Jurassic and high HF	Laslett Durango	2641	8.9	9 +/- 2.7

4.2.4 Carboniferous

The Carboniferous maps are not based on seismic interpretation but on interpolation between wells. The layers therefore show a very uniform thickness. This was used to reconstruct the eroded thickness. Maximum erosion values for the individual Carboniferous layers are between 100 and 450 m. Most erosion occurred in the northwest of the model along the coast line (Figure 34).

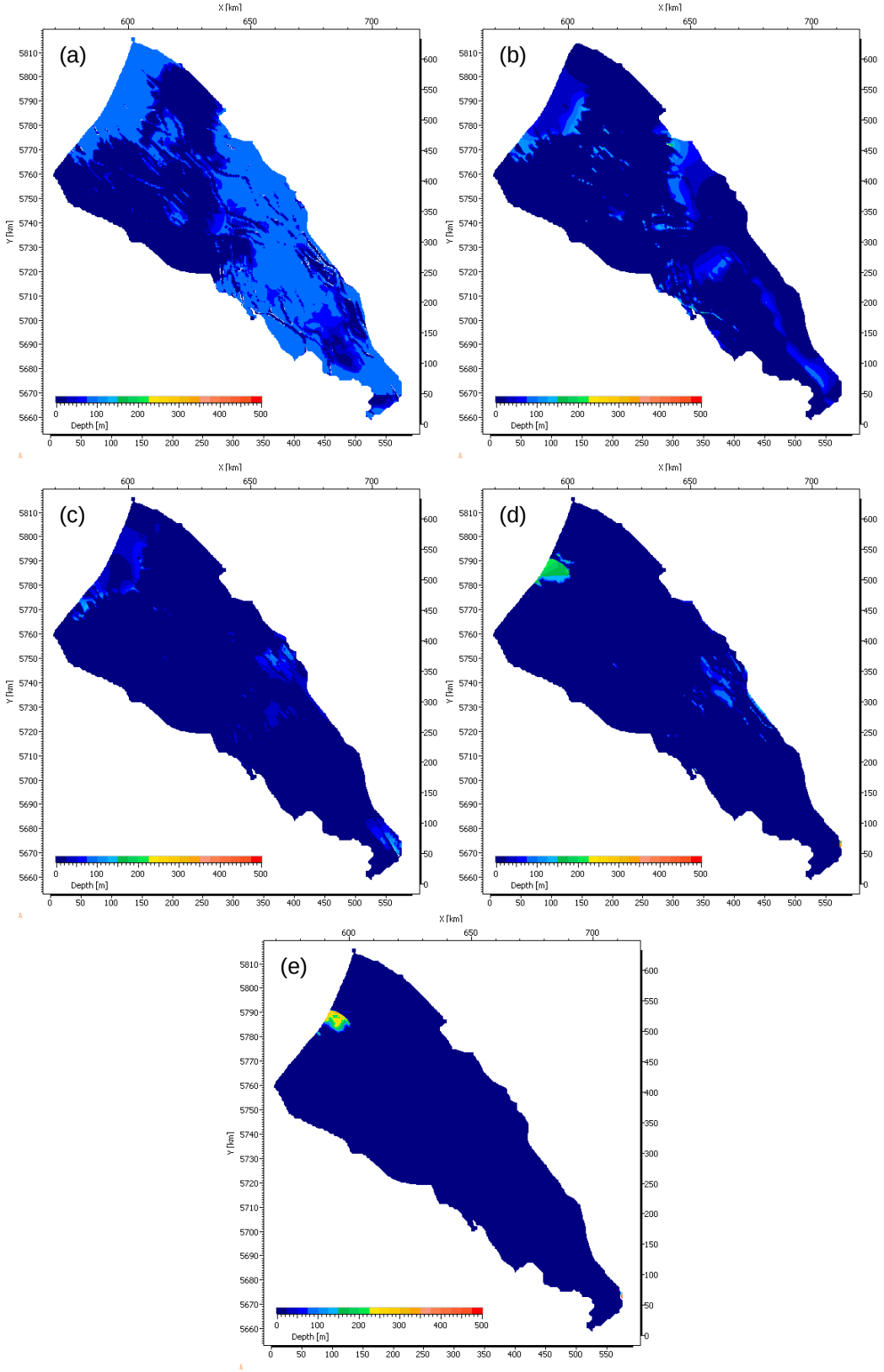

Figure 34 Erosion maps of the Late Carboniferous/Early Permian erosion of the Hunze (a) and Dinkel (b) Subgroup and Maurits (c), Ruurlo (d) and Baarlo (e) Formations

4.3 Burial Anomalies

A burial anomaly exists if past burial depth of an area exceeded present-day burial depth due to uplift which influenced the physical and chemical parameter of the rock, such as porosity, permeability, thermal conductivity and maturity (Figure 35). In the West Netherlands Basin and Roer Valley Graben a burial anomaly has been described by several authors (e.g., Van Balen et al., 2004), however the exact magnitude and extension of the anomaly is debated. Within this study a burial anomaly map was created using the reconstructed thicknesses from the erosion maps and running a forward basin model. The burial anomaly is mainly related to the Late Cretaceous inversion event. In some areas the difference in burial compared to present-day is more than 1500 m, indicating that significant differences in rock properties could occur (Figure 36). The burial anomaly is restricted to the northern part of the study area where highest values coincide with large inverted faults.

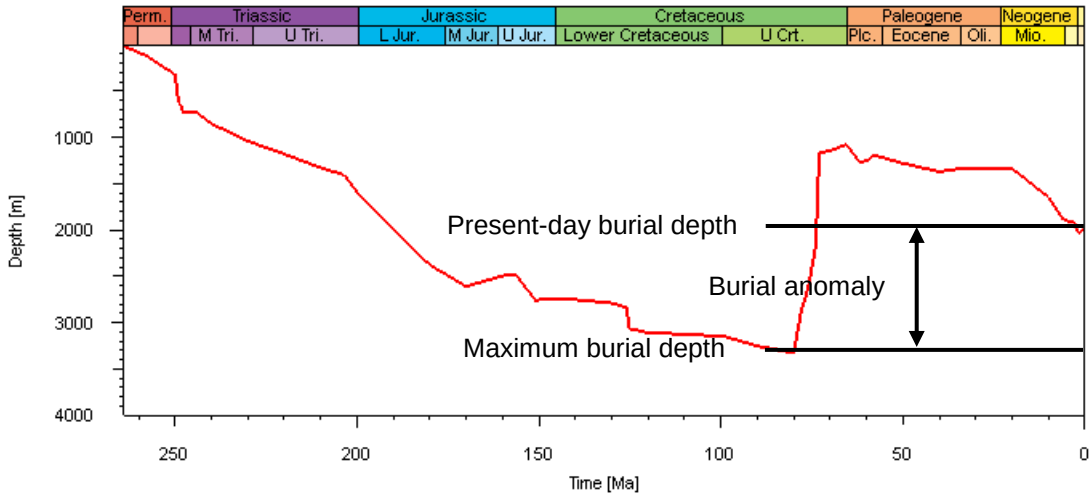

Figure 35 Burial depth extraction through time and definition of burial anomaly

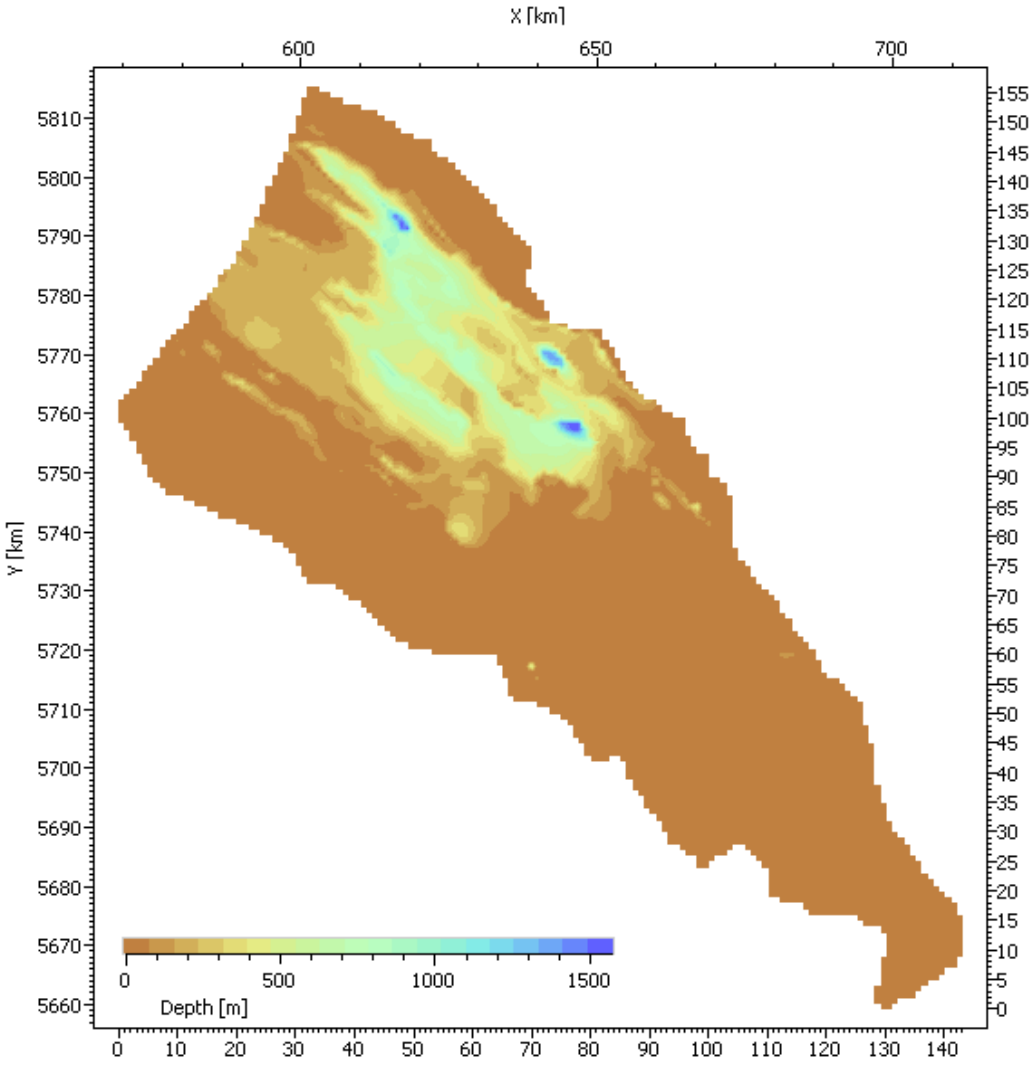

Figure 36 Burial anomaly of the Upper Cretaceous, calculated difference between Late Cretaceous burial and present-day (scenario 1)

Using higher erosion values for the Middle to Late Jurassic erosion phase of scenario 2 (up to 1400 m), a burial anomaly was also modeled in the south of the model (Figure 37). This burial anomaly is restricted to the sides of the model and mostly less than 300 m. If 200 m erosion more is assumed, the burial anomaly will expand towards the center of the southern end of the Roer Valley Graben but will have values of less than 200 m.

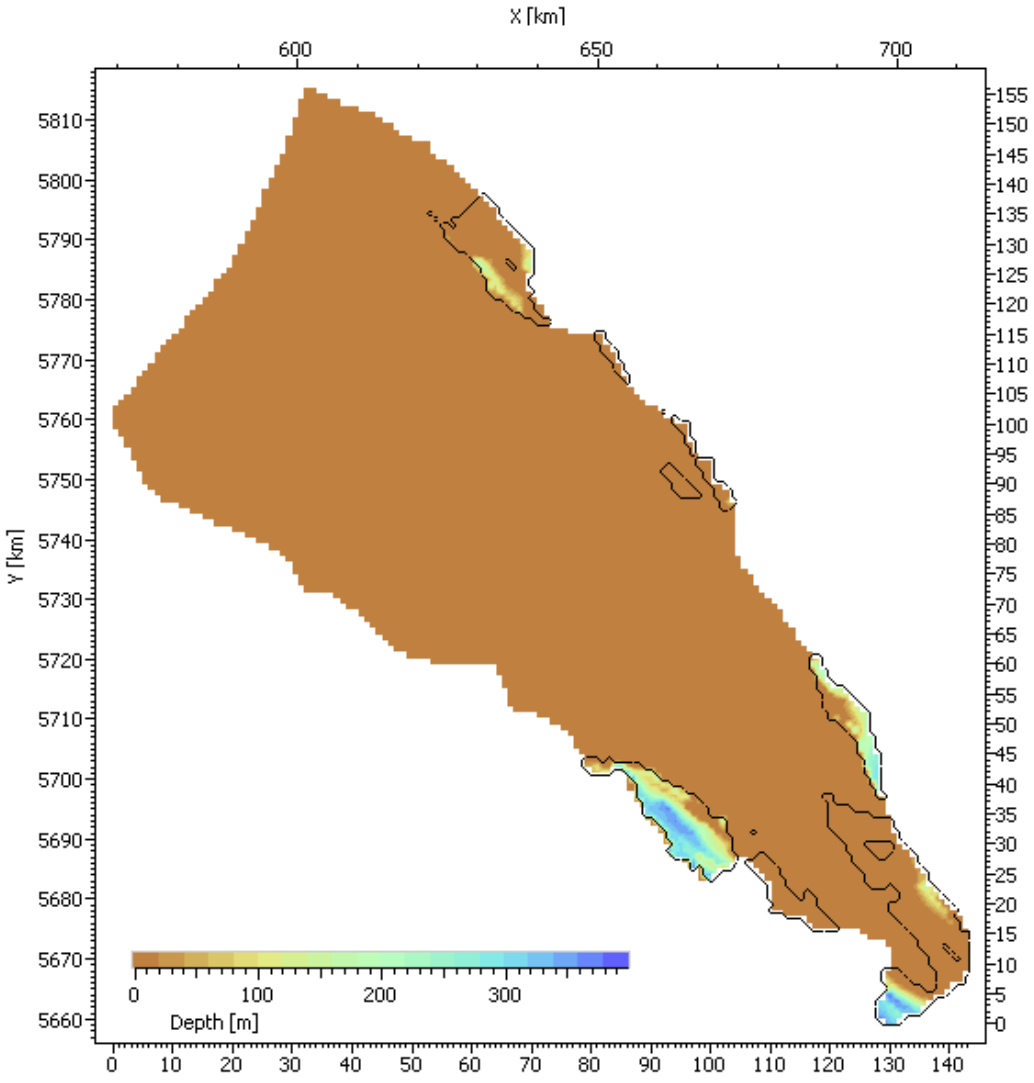

Figure 37 Burial anomaly of the Jurassic deep burial model (scenario 2) before erosion compared to present-day burial. Black outlines represent the extent of the burial anomaly if the eroded thickness is increased by another 200 m

For the third erosion scenario a combined burial anomaly map was created, showing the total present-day burial anomaly of the Late Jurassic erosion on the platforms and of the Late Cretaceous inversion in the basins (Figure 38). In this scenario, the burial anomaly in the northern part of the model does not change compared to previous scenarios. The burial anomaly in the southern part of the model, in the Roer Valley Graben however is higher than in the previous scenarios.

For the observations of the effect of the burial anomaly on the porosity and temperature, the first model with scenario 1 was used.

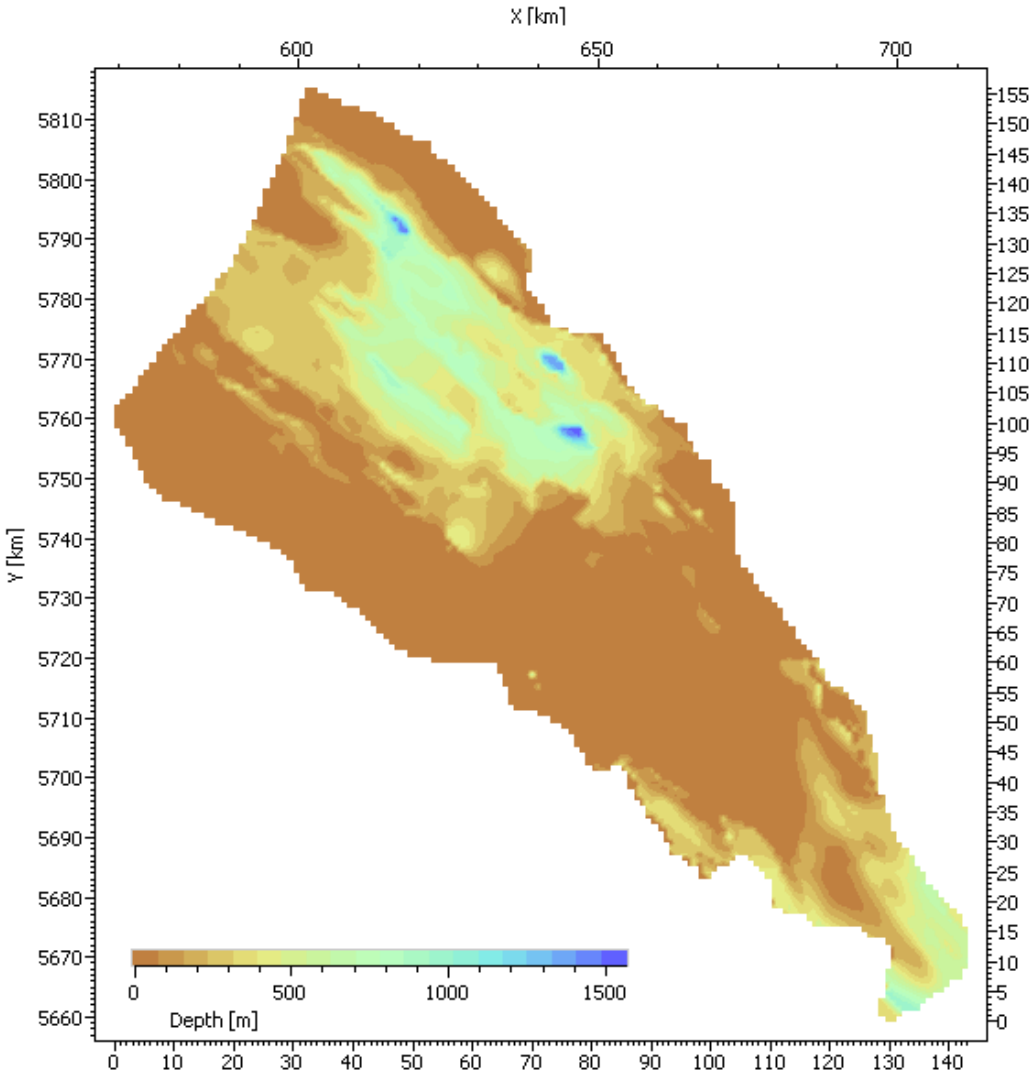

Figure 38 Burial anomaly of the Late Jurassic erosion on the platform areas and the Late Cretaceous inversion of the basin areas of scenario 3

4.4 Porosity calibration

Porosity was calibrated for sandstone/shale mixed lithologies based on measured porosity-depth trends (see chapter 3.3). Individual measured values from the wells fit reasonably well with the calculated porosity after the calibration (Figure 17, Figure 19, Figure 22 and Figure 24). Figure 39 gives an overview of the calculated porosity distribution for the reservoir horizons in the model area. The sandstone layers of the Early Cretaceous Rijnland Group show the highest values, between 16 and 38% porosity with lowest values in the southwest and highest values in the northeast. The reservoirs of Upper and Lower Triassic have lower porosities. Three layers have 25% shale in their lithology. These layers have porosities between 5 and 27%. Slightly higher porosities were calculated for the two pure sandstone reservoirs, ranging between 8 and 28%. The lowest values occur in the northwest of the model and the center of the Roer Valley Graben. The Permian sandstone layer shows similar values and distribution as the Early Triassic sandstone layers.

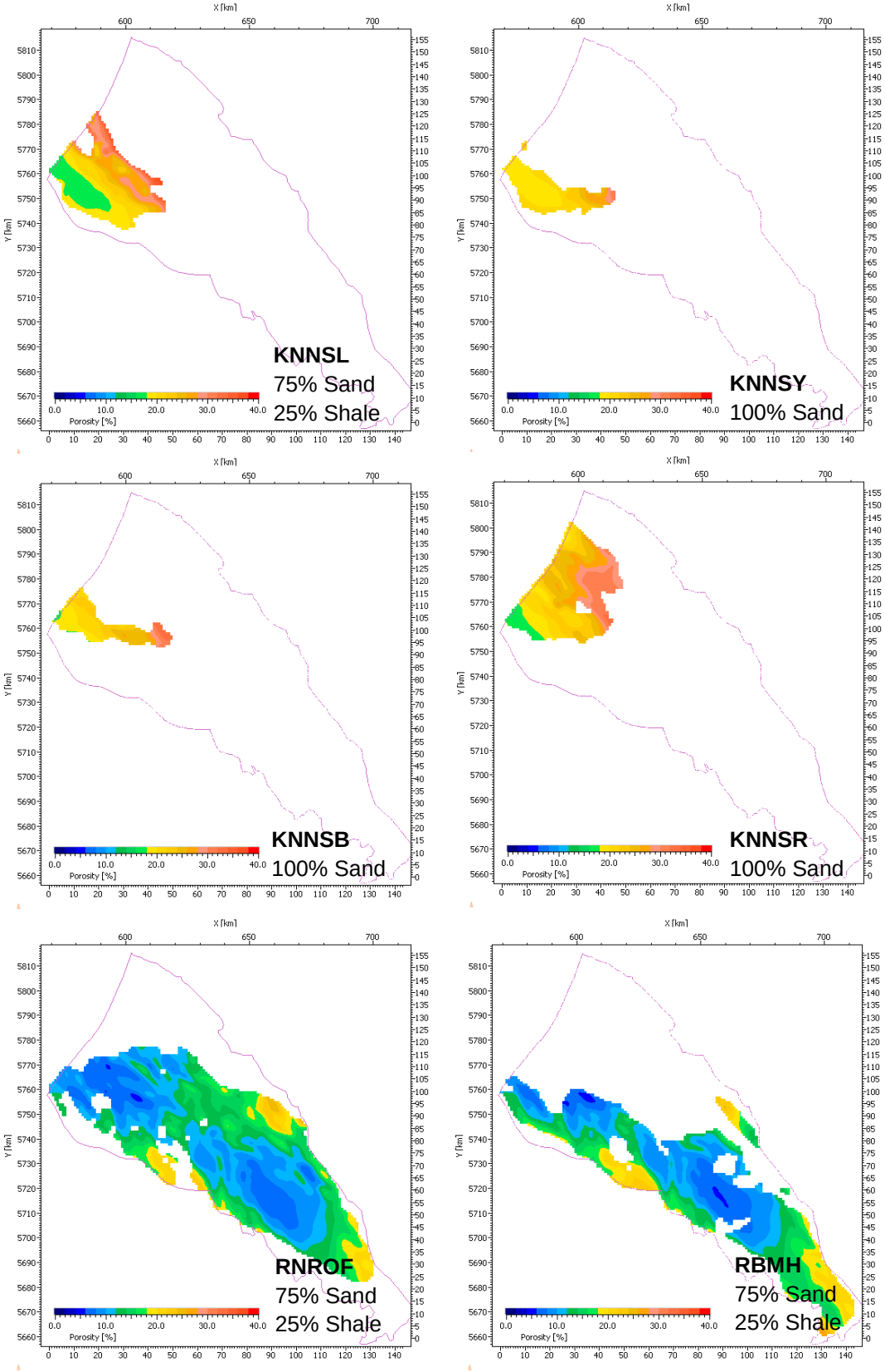
KNNSL
75% Sand
25% Shale
KNNSY
100% Sand
KNNSB
100% Sand
KNNSR
100% Sand
RNROF
75% Sand
25% Shale
RBMH
75% Sand
25% Shale
X [km]
Y [km]
Porosity [%]

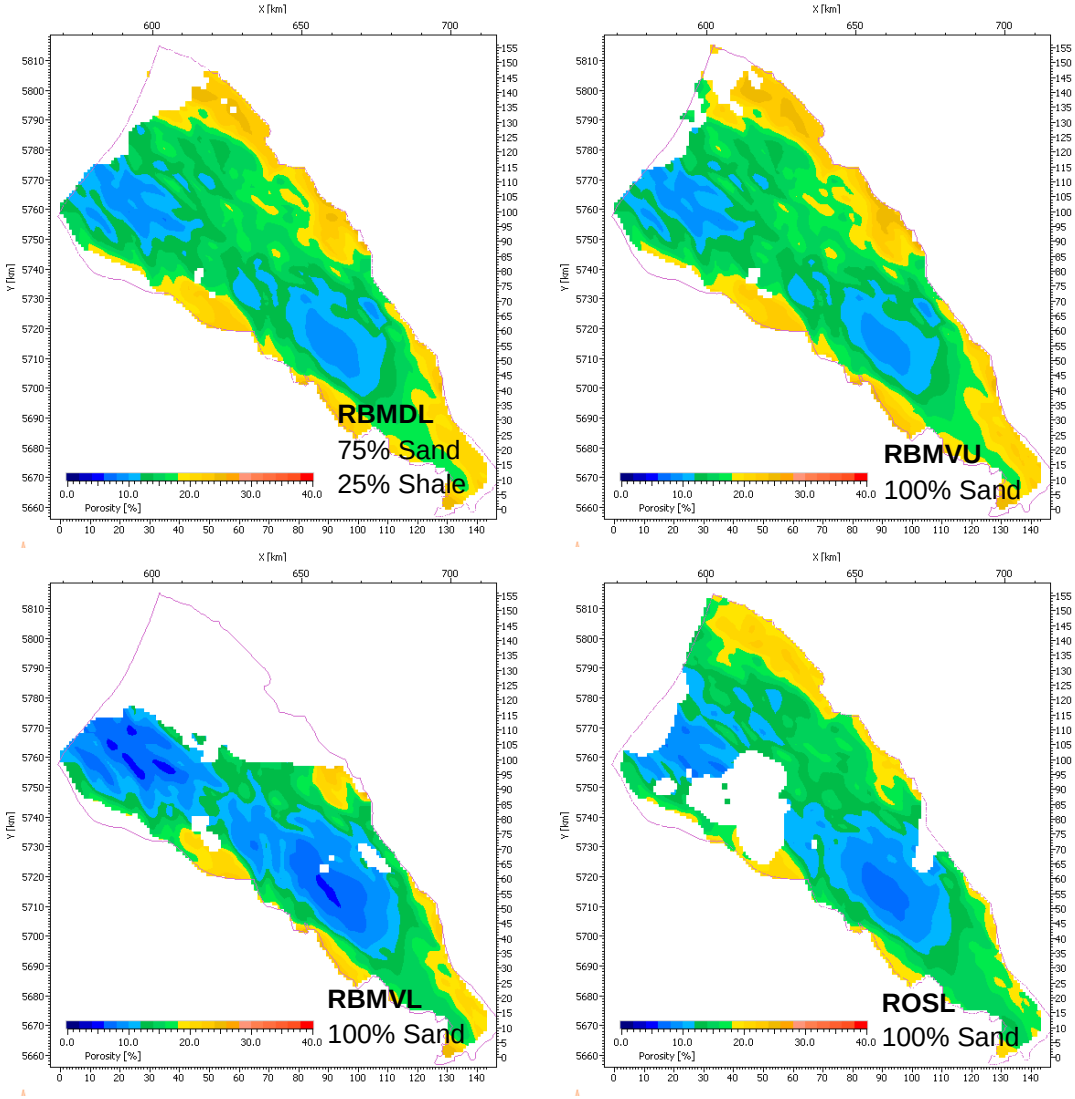

Figure 39 Calculated porosity of the reservoir layers

4.5 Influence of the burial anomaly on calculated porosities

One scenario of the model was calculated without erosion to compare the porosity with and without erosion and to check how much the burial anomaly influences the physical parameters of the layer. Figure 40 shows the difference in porosity of a pure sandstone layer and a 75% shale, 25% silt layer between the two scenarios. The difference in porosity can be up to 15%. Shale rich layers show higher differences in porosity than pure sandstone layers. The different porosity is positively correlated to the burial anomaly; however the burial anomaly needs to exceed 300 m to change the porosity significantly. Figure 41 shows porosity/depth extractions of three different well positions for both scenarios. The wells are situated in areas with burial anomalies of different magnitude. Figure 41a shows the difference in porosity for the location of well JUT-01 which is situated in the northeast of the model along a large reverse fault along which inversion took place. It was drilled through the fault and the doubled part of the stratigraphy indicates at least 1500 m of uplift (Nelskamp et al., 2008). In this study a burial anomaly of 1300 m was modeled. The biggest difference is

modeled in the Early Jurassic Altena Group, situated directly underneath the unconformity. The shale rich rocks have up to 15% lower porosities if the erosion is included in the modeling.

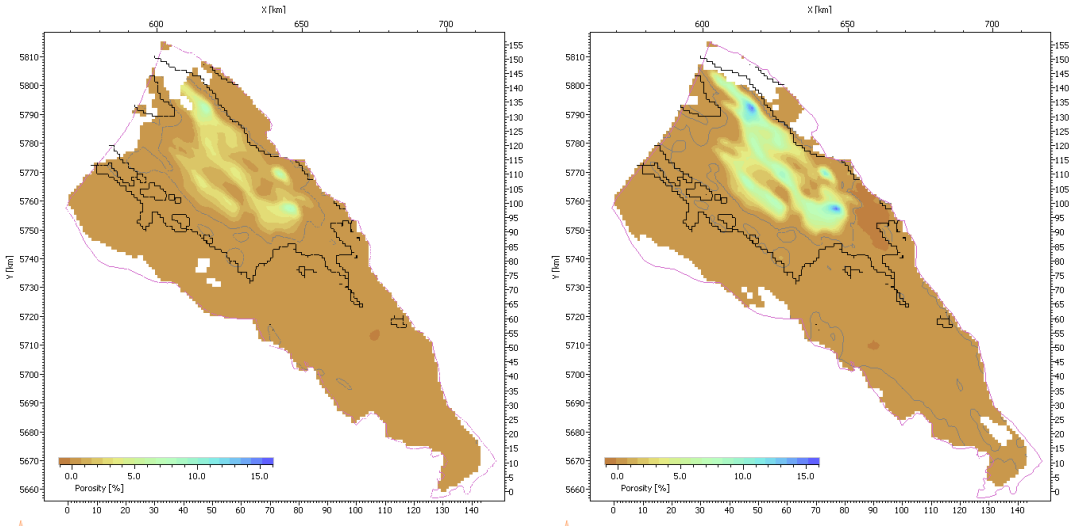

Figure 40 Porosity difference of layer RBMVU (a) and ATAL (b) between a model calculated with erosion and one model without.

Figure 41b is an extraction at the position of well ARV-01 in the center of the West Netherlands Basin. The modeled burial anomaly at this position is ~600 m. In the Early Jurassic Altena Group a difference in porosity of approximately 5-10% is modeled. The third extraction point is situated at the position of well WAS-23 in the northwest of the model. At this point the modeled burial anomaly is ~250 m. Almost no influence of the burial anomaly on the porosity is visible. The same observation could be made with other physical properties such as permeability and thermal conductivity.

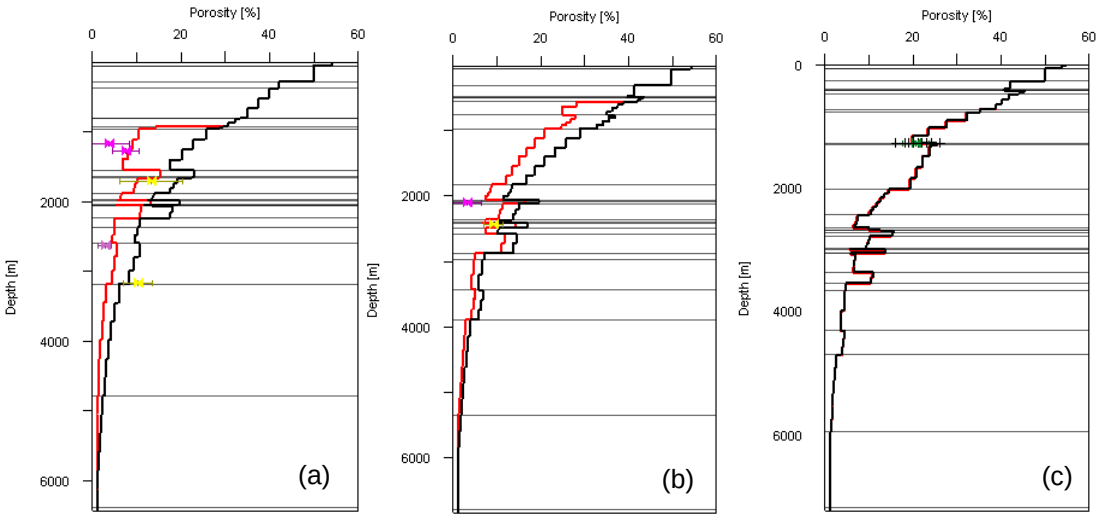

Figure 41 Comparison of different porosity-depth curves (red with erosion, black without) for the location of well JUT-01 (a, ~1300 m burial anomaly), well ARV-01 (b, ~600 m burial anomaly) and well WAS-23 (c, ~250 m burial anomaly)

4.6 Temperature

The calculated temperature for the individual reservoirs depends on the depth of the layer, the physical parameter of the rocks, the under- and overlying sediments, the burial anomaly and the temperature of the lower and upper thermal boundary (surface temperature and basal heat flow). It was calculated for the model with burial anomaly and calibrated porosities. The temperature of the Rijnland reservoirs ranges between 25 and 80°C, the Triassic reservoirs have temperatures between 50 and 150°C and the temperature of the Rotliegend sandstone varies between 60 and175°C (Figure 42). The highest temperatures of the layers are situated at the position of deepest present-day burial.

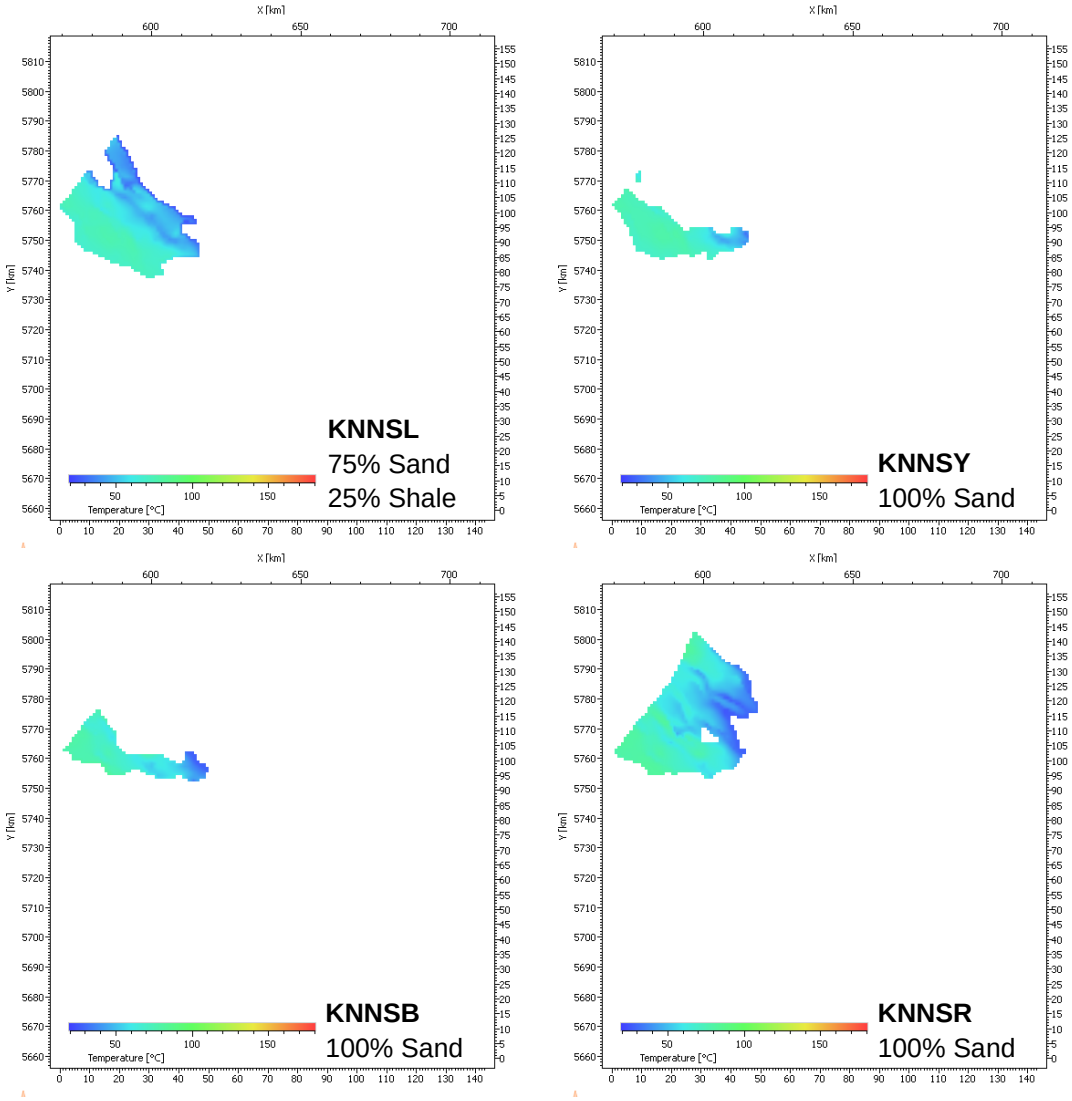

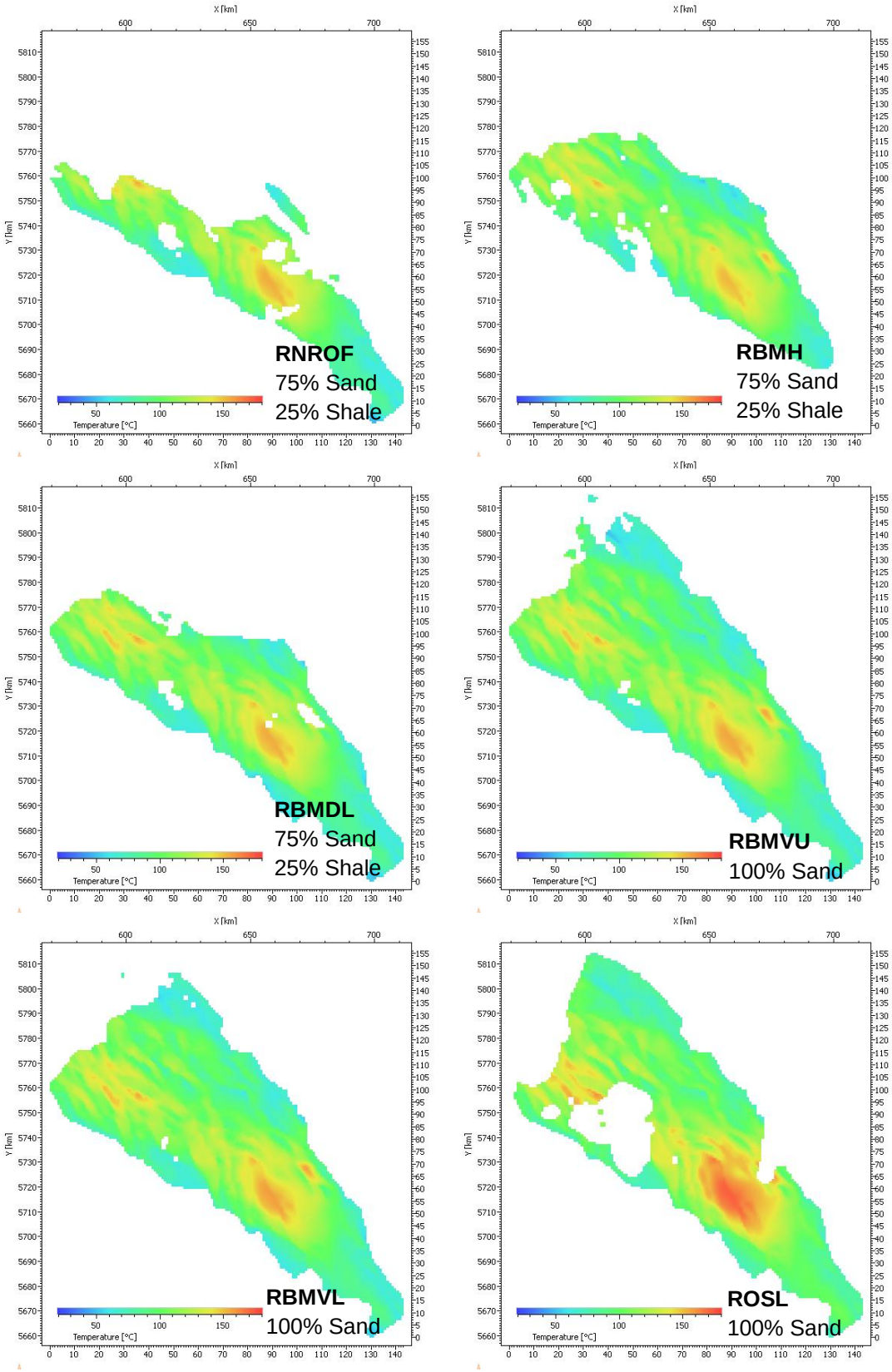

Figure 42 Temperature of the reservoir layers

5 Discussion

The presented model has some inconsistencies that could not be resolved in a reasonable amount of time. In the following the shortcomings and uncertainties of the model are discussed and the effects of general modeling assumptions and conditions are presented.

5.1 Burial history

The maps, the model is based upon, are the result of a detailed 3D mapping project, performed at TNO in the years 1991 to 2004. In this project ten maps from the depth of the Permian to ground surface were interpreted. The model was refined in the context of the ThermoGis project in 2010 and sandstone reservoir horizons of the Early Cretaceous, Triassic and Early Permian were included in the model. These reservoir horizons are based on well and log interpretations and interpolation between wells. With this method sandstone layers are interpreted and a subdivision of the layer at the position of the sandstone is implemented but in between the sandstones or outside the depositional area of the sandstones no subdivision of the layer has been interpreted. Maps in basin modeling represent layers of similar deposition time rather than lithological differences. Furthermore only one time of deposition can be assigned per layer and the times may not overlap. Therefore this method leads to incorrect depositional geometries and speed of burial. This issue can only be resolved by detailed seismic mapping of the reservoir horizons and chemo- or biostratigraphic dating of the wells where no reservoir was found. On the other hand the inclusion of these reservoir layers adds to the value of the model, as the thermal conductivity, porosity and temperature at the position of the sandstone layer can be calculated. This is especially important for the geothermal purpose this model was created for. These parameters are only marginally affected by the wrong geometries and speed of deposition because the influence of later processes such as maximum burial is more important.

Another problem with the stratigraphic model is the erosion. Due to limitations in the basin modeling software a stratigraphic horizon cannot be affected by more than one phase of erosion. If areas with different structural evolutions are included in the model and erosion of the same layer occurred at different time steps, the horizon needs to be subdivided. For this, the deposition time of the layer needs to be split as well because each of the new layers must have a distinct deposition time. The deposition time of the layer is therefore shortened compared to the real situation. This cannot be avoided in structurally complex areas. The newest version of the modeling software (Petromod v. 2011.1, Schlumberger) is able to calculate the effects of more than more phase of erosion and solves this problem and will be used in further studies.

Because each layer must have a distinct deposition time, one layer cannot have different depositional times. If deposition of one layer starts earlier in one part of the model compared to another, this is difficult to include in the model without detailed stratigraphic information for the whole model area that would allow mapping out the depositional thickness for the layer for each timestep.

The Paleozoic layers of the model were built in the context of the Petroplay study, which was performed at TNO in 2004 and 2005. They are based on well data and a few deep lines with seismic interpretation. The depth map of the uppermost layer (base Hunze Formation),

produced in this study, does not fit well with the depth map of the lowermost layer of the original model (base Permian). The distribution and thickness of the Hunze Formation is therefore not the original one. This creates some problems with the definition of the extent of the Late Carboniferous/Early Permian erosion phase. It was, however, decided that the addition of the Paleozoic layers was more important for the temperature calculation of the model than the correct distribution and thickness of one layer.

For the modeling of the West Netherlands Basin and the Roer Valley Graben no 3D tectonic reconstruction was carried out. This is usually necessary for basin models in compressive settings, as normal 3D basin models account for only vertical movements and do not include lateral movements. The study area experienced several phases of compression that caused the reverse activation of faults and stratigraphic doubling of some layers (De Jager, 2003; Nelskamp et al., 2008). This effect could not be included into the model.

5.2 Erosion

The reconstruction of eroded thicknesses and timing of erosion is usually a challenge. The quality and reliability of the reconstruction strongly depends on the quality and amount of available data. In the West Netherlands Basin, in the north of the model, the data availability is quite good. The area is of interest for the petroleum industry since gas and oil fields were found and are produced which created a good database. On the other hand the main exploration and production activity in the Roer Valley Graben took place in the first half of the last century and was mainly focused on coal. Especially in the south very few wells are available which are quite old and have only limited logs or other data of poor quality. The southernmost part of the model relies on data from one well with calibration data and detailed stratigraphy. 3D seismic is also not available in the south of the model. It is therefore assumed, that the measured maturity (Vitrinite reflectance and Fission Track) and temperature from this well are representative for the regional history of the southern RVG instead of local effects at the same time.

One main uncertainty in the model is the original depositional thickness of the Late Cretaceous sediments in the basins. Especially in the West Netherlands Basin no Late Cretaceous sediments are present in the basin at present-day. There are three different possible scenarios for the deposition of the Chalk Group. One possibility is that the basins continued to subside until the onset of inversion and therefore accumulated a significant amount of sediments. The second scenario is that subsidence in the basins was reduced or even stopped due to the compressive movements and the thickness of the sediments is limited. The third option is that inversion and uplift started earlier and no Late Cretaceous sediments accumulated in the basins. Based on average sedimentary thicknesses of the underlying layers and calibration data (Vitrinite reflectance) the first two options are more likely. 1D modeling showed that without burial in the Late Cretaceous the measured maturity data could not be calibrated. Worum (2004) identified, based on anomalies in seismic velocity and geometrical reconstruction, an increasing depositional thickness of the lowermost Upper Chalk unit towards the NE and an average thickness for the rest of about 300 m. These results were used in this study.

The determination of the exact timing of the main erosion in the Late Cretaceous/Early Tertiary is also difficult. The inversion occurred in distinct pulses (De Jager, 2003) and each pulse had a different extent per basin. From well logs in the Roer Valley Graben it is evident, that the preserved Late Cretaceous sediments are of Campanian to Danian age and

apparently deposited after the main inversion of the basin. The Sub-Hercynian inversion pulse, occurring during the Mid-Campanian, had therefore more influence in the Roer Valley Graben than the Laramide pulse. In the north of the model no Late Cretaceous sediments are preserved. Several studies assume that the Laramide inversion pulse (Latest Cretaceous/Paleocene) had a bigger influence there (De Jager, 2003; Worum, 2004). However assigning different erosion times to one layer was not possible. It was therefore decided to place the main erosion in the Sub-Hercynian and only erode the uppermost layer of the Upper Cretaceous during the Laramide phase.

In the northern part of the Roer Valley Graben the present-day burial masks the uplift and erosion of the Late Cretaceous inversion phase. An exact determination of this erosion is therefore not possible. In the south of the Roer Valley Graben vitrinite reflectance and fission track data show the influence of an erosion phase. A Late Jurassic as well as a Late Cretaceous erosion age is possible, based on the data. Tectonic processes such as uplift and erosion of the basin flanks during an extension are more in favor of a Late Cretaceous erosion age (e.g. Barr, 1987) and the detailed analysis of fission track data from the northern part of the Roer Valley Graben by Luijendijk et al. (2011) also suggests that the Late Cretaceous inversion caused the erosion. The study of Luijendijk et al. (2011) also includes the possibility of false ages and overprinting by hinterland ages. This is not taken into account in this study.

A different issue is the reproducibility of fission track measurements and the selection of the right model for calibration. (Ketcham et al., 2009) describe an experiment where the same samples were given to different interpreters, resulting in significantly different models. He states that a standardized length calibration schema is necessary to ensure comparability of measurements from different sources. Another problem is the correct selection of the calibration model. Several models have been published that calculate fission track length distributions for apatites of different composition (Laslett et al., 1987; Crowley et al., 1991; Ketcham et al., 2007). It is necessary to select the model, that describes the composition of the measured apatite the best as the model gives a higher uncertainty than the temperature history (Figure 33). No detailed description of the apatite composition was available in the context of this study and only the models of (Laslett et al., 1987) and (Crowley et al., 1991) are implemented in the modeling software, so the model with the best fit of calculated fission track length distribution in combination with average length and age was selected. A more detailed study of the fission track measurements in combination with different models and sensitivity analysis of the data is published by (Luijendijk et al., 2011).

5.3 Burial anomaly

The final burial anomaly is the result of the reconstruction of erosion of the case considered most likely. It resembles in magnitude and extent the burial anomaly created by Worum (2004) for the north of the model. For the south two different 3D and 3 different 1D models were tested. The 3D high erosion model, leads to a burial anomaly of up to 350 m along the sides of the model (Figure 37). If the erosion is increased by another 200 m, a minor burial anomaly would also show in the center of the graben. This does not influence the calculated thermal properties of the layers because no influence of a burial anomaly of less than 300 m on the physical parameter of the layers could be observed (Figure 41).

5.4 Porosity

The correct calibration of porosity has a big effect on the correct calculation of thermal properties of the reservoirs and can influence the effect a burial anomaly has on the porosity. For example, shale rich sediments compact faster during the first 2000 m of burial while the influence of depth on the porosity beneath 3000 m is reduced (Figure 13). Sand rich sediments have a less steep porosity reduction with depth but compaction continues up to 7000 m burial depth. This effect can be seen in the comparison of the effect or the burial anomaly on a layer with sandstone lithology and a layer with shale lithology (Figure 40). Shales are therefore influenced stronger by burial anomalies when buried less than 3000 m and burial anomalies of less than 300 m might still have an influence while the effect of a burial anomaly in a sandstone layer is less strong but can be still visible in very deeply buried sandstones.

5.5 Temperature

The present-day temperature is calibrated to the corrected temperature measurements from wells in the study area. The past heat flow evolution was generated using tectonic modeling and calibration to maturity parameters. This method is very sensitive to the burial history of the model, especially in times of erosion. In the case of past maximum temperature or deep burial events, the inclination of the vitrinite reflectance curve can give an indication whether the high temperature is related to high heat flow or deep burial, but there is an uncertainty attached to. If the erosion event was not the one causing maximum temperature or if present-day temperatures exceed past ones, this method cannot be used and the heat flow and erosion values are estimates, influencing each other.

For the south of the study area, fission track and vitrinite reflectance data indicate high temperatures during the Late Jurassic. Calibration data could be fitted using an erosion of 1400 m in the Late Jurassic or 1850 m in the Late Cretaceous and elevated heat flows of 80 mW/m^2. These elevated heat flows are also reported for the adjacent area in Germany (Littke et al., 2000) and further north in the study area volcanic intrusions dated around 130 Ma (but believed to be altered and could therefore be around 140-150 Ma old, Van Bergen and Sissingh, 2007) are found. Alternatively local high temperatures could be related to large scale fluid flow along high permeable fault zones as has been modeled for the Variscan thrust front in Belgium (Lünenschloss et al. 2008). The study area was influenced by Jurassic rifting events, caused by the breakup of Pangea. During Middle Jurassic the Central North Sea dome caused uplift and elevated heat flows in large parts of the Dutch North Sea (e.g., Herngreen et al., 2003). The Zuidval volcano just offshore The Netherlands is also dated Late Jurassic (Sissingh, 2004). The area experienced significant tectonic extension and elevated heat flows are a reasonable assumption for that time.

Table 4 Geothermal gradient, basal heat flow and heat flow in sediments for different depth extracted from the model for three different locations in the Roer Valley Graben and comparison to values determined by (Luijendijk et al., 2010)

AND-06	Geothermal Gradient [°C/1km]	Basal heat flow [mW/m^2]	Heat flow in sediments [mW/m^2]
Luijendijk et al. 2010	37.6*		63 +/- 6
This study			
1000 m	35.5	52	58
2000 m	38.8	52	62
3000 m	30.7	52	62
4000 m	29.8	52	61
5000 m	29.0	52	59
6000 m	28.1	52	57
7000 m	27.3	52	55
8000 m	26.4	52	53
Average value for 0-2300 m	36.5		59

WWK-01	Geothermal Gradient [°C/1km]	Basal heat flow [mW/m^2]	Heat flow in sediments [mW/m^2]
Luijendijk et al. 2010	34.7*		60 +/- 8
This study			
1000 m	34.7	52	58
2000 m	37.8	52	61
3000 m	29.4	52	63
4000 m	31.1	52	60
5000 m	28.8	52	59
6000 m	28.0	52	57
7000 m	27.4	52	55
8000 m	26.7	52	54
Average value for 0-2700 m	35.4		59

WWS-01	Geothermal Gradient [°C/1km]	Basal heat flow [mW/m^2]	Heat flow in sediments [mW/m^2]
Luijendijk et al. 2010	35.7*		62 +/- 7
This study			
1000 m	35.0	52	59
2000 m	38.9	52	62
3000 m	23.3	52	64
4000 m	31.1	52	60
5000 m	28.9	52	59
6000 m	28.2	52	57
7000 m	27.2	52	55
8000 m	26.4	52	53
Average value for 0-2600 m	35.1		59

*The geothermal gradient was calculated using the deepest available temperature data and a surface temperature of 10 °C

A comparison of thermal gradient values calculated in this study with values from Luijendijk et al. (2010) shows a good fit (Table 4). In their paper Luijendijk et al. also looked at groundwater flow as a possible cause for temperature anomalies in the depth range of 1000 to 1500 m. Especially the shallow temperature measurement of well WWK-01 (Figure 43) is identified as possibly being influenced by hot groundwater. They concluded that the shallow thermal anomaly observed in the Roer Valley Graben might be a result of hot fluid flow along faults. This assumption could not be tested in this model, as the process of groundwater flow is not included in the software.

The reduction in heat flow from 2500 m to the top is caused by the rapid change in surface temperature after the ice ages (Figure 43). The sediment surface temperatures increase from around 0 to 10 in the last 0.1 Ma in the model, reducing the heat flow towards the surface.

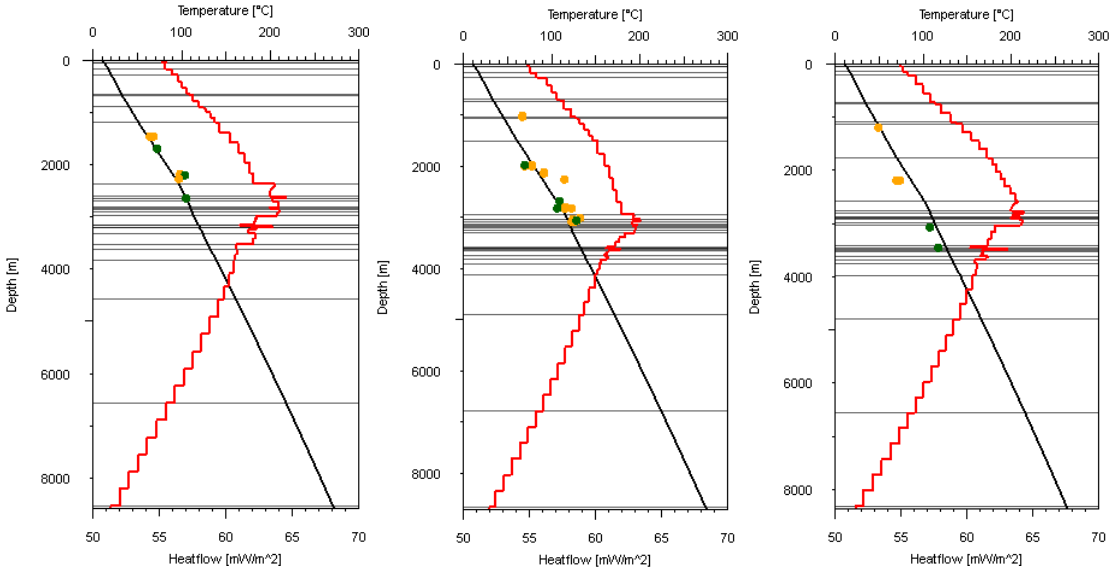

Figure 43 Temperature calibration and heat flow of wells AND-06 (a), WWK-01 (b) and WWS-01 (c)

5.6 Heat flow calibration

Four different heat flow scenarios were modeled in the context of this study. The first one assumed a constant heat flow of 60 mW/m^2 for the whole study area. The blue line in Figure 44 and Figure 45 shows the calibration result and temperature evolution for this scenario. It is evident, that a constant heat flow for the whole study area cannot be calibrated and that spatial differences in past and present heat flow exist. To account for the special differences that are related to structural differences and to create a reasonable heat flow evolution through time, calibrated to the tectonic subsidence of the model, a tectonic heat flow model was calculated using PetroProb (Van Wees et al., 2009). The resulting heat flow maps gave good calibration in some areas, but especially too low present-day temperatures in others (red line in Figure 44 and Figure 45). To fit the present-day temperature the PetroMod heat flow calibration tool was used. This tool uses heat flow maps and temperature and vitrinite reflectance measurements as input. It then calculates a number of runs, shifting the heat flow trend up and down for each calibration well and gives a map with the best calibration for all positions as result. This method shifts the whole of the trend; heat flow peaks are therefore also lifted or lowered if the present-day heat flow needs to be shifted to fit the temperature

measurements. If the reason for a higher or lower heat flow is related to the initial thickness of the crust and the mantle, this approach is reasonable. If the shift is related to local fluid flow or other spatially or temporally restricted effects, this approach gives wrong heat flow trends. Since the maps generated by the PetroMod heat flow calibration tool were calibrated against temperature and vitrinite reflectance measurements, they give the best calibration result, as can be seen in the green line in Figure 44 and Figure 45. To test the influence of the paleo heat flow evolution on the calibration result, a fourth model was calculated. For this model, the present-day heat flow map, generated in the third model, was used for the whole time. The result of the calibration and the temperature evolution can be seen in the orange line in Figure 44 and Figure 45. The resulting calibration does not differ from the previous model.

5.7 Pressure

The model was calculated including pressure effects and calibrated to present-day pressures. Faults are not included in the model. Modeled and measured pressures indicate no or very low overpressures in the study area. Reported pressure values can be influenced by the intense production that occurs in the area. Values below hydrostatic pressure have been excluded from the calibration data set, it is still possible, that values influenced by production but still above hydrostatic are part of it. The data set comprises pressures measured in water and in gas, but only measurements in water were used for calibration.

The highest overpressure of up to 7 MPa above hydrostatic was modeled in the Upper Triassic layer, which includes anhydrite layers that were deposited in the study area (Tno, 2001). The pattern of overpressure in this layer mimics the thickness distribution of the Early Jurassic Altena Group that is situated directly on top. No pressure measurements were available for this layer, it is therefore not clear whether this overpressure is a modeling artifact or represents real conditions.

In the Neogene Upper North Sea Group overpressures between 0 and 0.5 MPa were modeled. Pressures are slightly elevated in the area of the RVG and hydrostatic in the WNB. This is related to the higher sedimentation/subsidence rate in the RVG compared to the WNB. A pressure gradient therefore exists, causing fluid flow from the RVG towards the north. In addition to this pressure-driven fluid flow, a topography-driven fluid flow was identified in the RVG, from south to north (Luijendijk et al., 2010). This influences the pressure system as well as the temperature in the upper 1000 m, as described by Luijendijk et al. (2010), an effect that could not be included into the model.

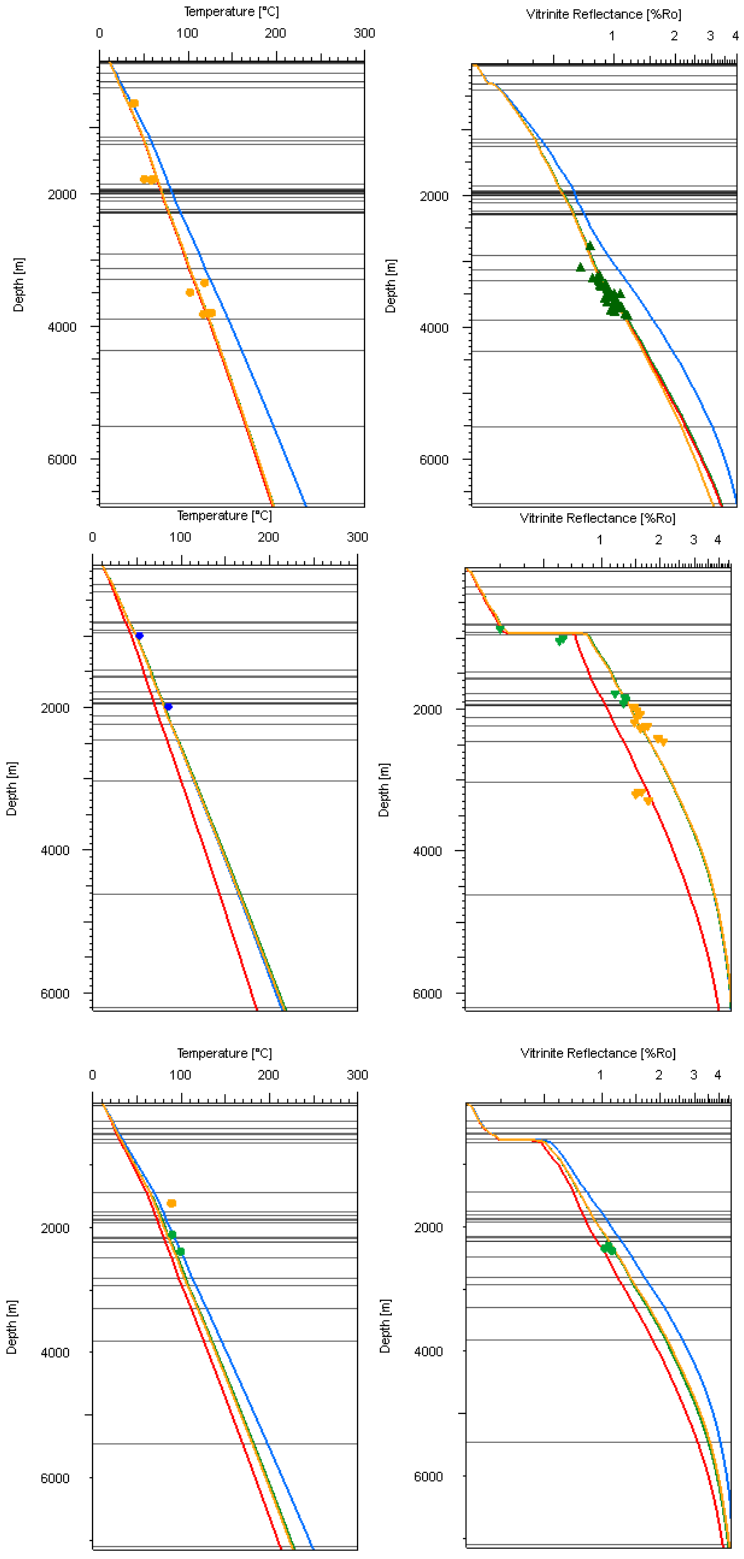

Figure 44 Present-day temperature and vitrinite reflectance calibration of well HVS-01 (a), JUT-01 (b) and PKP-01 (c) using the four different heat flow scenarios described in chapter 2.5.2

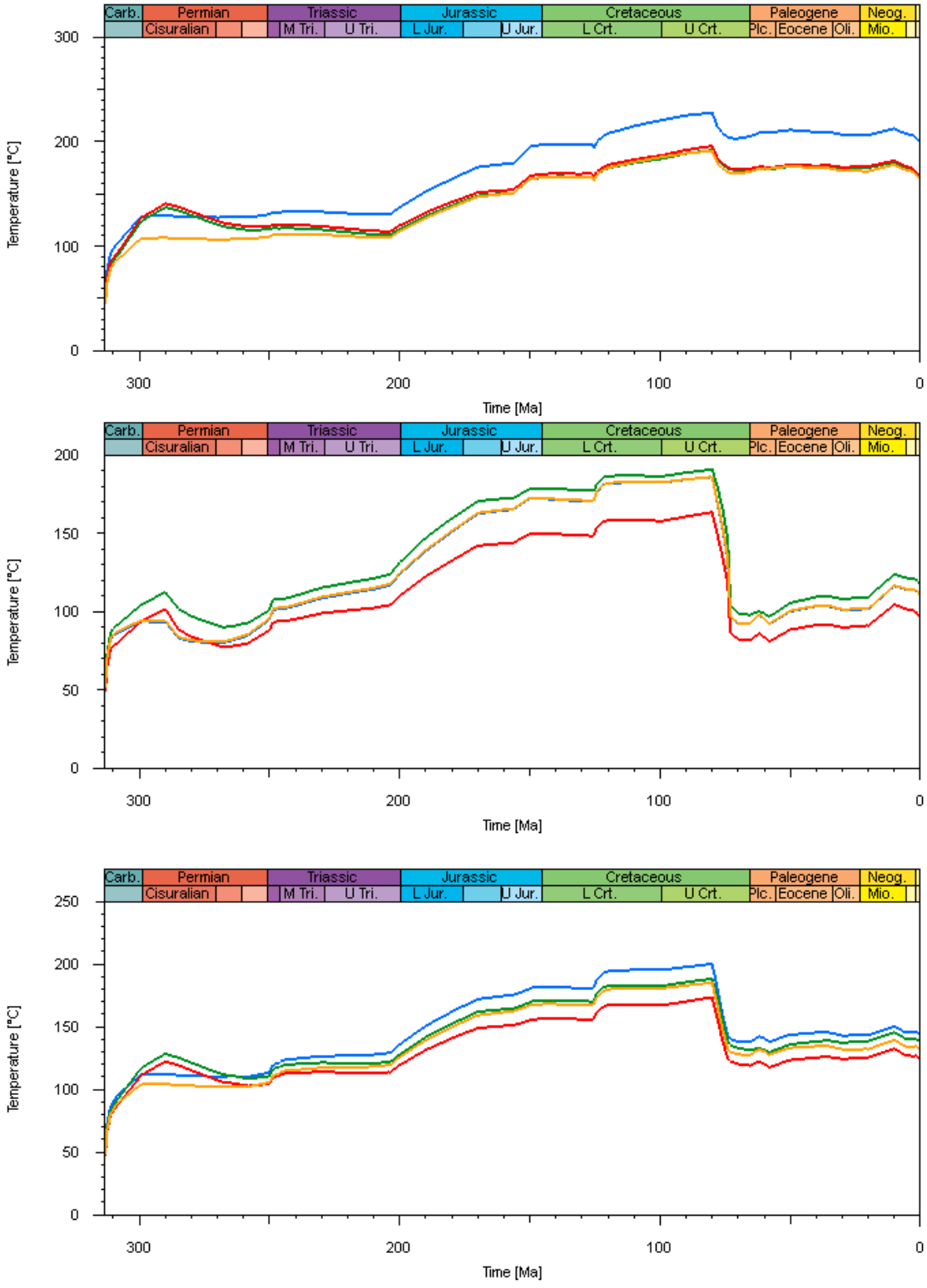

Figure 45 Temperature evolution of the base of the DCCB of well HVS-01 (a), JUT-01 (b) and PKP-01 (c) using the four different heat flow scenarios described in chapter 2.5.2

6 Conclusions

A 3D basin model was constructed of the West Netherlands Basin and the Roer Valley Graben to look at several parameters influencing the production of deep geothermal energy. A focus was put on the processes influencing the temperature and porosity of potential aquifers, such as compaction, overcompaction related to burial and erosion, overpressure, basal heat flow and surface temperatures.

The main factor influencing temperature and porosity is overcompaction. A detailed analysis of possible burial and erosion was made for the different erosion phases influencing the study area (Late Jurassic and Late Cretaceous). The Late Cretaceous erosion resulted in a burial anomaly of up to 1500 m in the northern part of the study area. Along the margins of the basins the Late Jurassic erosion phase had more influence and resulted in a burial anomaly of up to 400 m. The three different erosion scenarios for the Roer Valley Graben resulted in burial anomalies between 0 and 800 m.

The burial anomaly influences the calculated porosity, permeability and thermal conductivity. Due to the steeper compaction curve, the burial anomaly has a bigger effect in clay rich layers until a burial depth of 3000 m. In sand rich layers the effect of a burial anomaly is less but extends to burial depth of 7000 m. The modeling shows further, that a burial anomaly of less than 300 m has no significant effect on the physical properties of the rocks.

A detailed surface temperature evolution for the Tertiary was used in the modeling. In combination with a very detailed Pliocene to Pleistocene layer definition in the model, the effect of the rapid temperature change after the end of the ice ages can be seen. The temperature of the upper 2500 m is not yet equilibrated, resulting in an overall heat flow decrease in the upper part of the model.

7 Acknowledgements

We would like to thank Schlumberger for the opportunity to use their basin modeling software PetroMod in the context of this study.

8 References

Van Adrichem Boogaert, H.A., Kouwe, W.F.P., 1993. Stratigraphic nomenclature of the Netherlands, revision and update by RGD and NOGEPA. Mededelingen Rijks Geologische Dienst 50, 1-40.

Van Balen, R.T., Van Bergen, F., De Leeuw, C.S., Pagnier, H.J.M., Simmelink, E., Van Wees, J.-D., Verweij, H., 2000a. Modelling the evolution of hydrocarbon systems in the inverted West Netherlands Basin, the Netherlands. Journal of Geochemical Exploration 69-70, 685-688.

Van Balen, R.T., Van Bergen, G., De Leeuw, C., Pagnier, H.J.M., Simmelink, H., Van Wees, J.D., Verweij, J.M., 2000b. Modeling the hydrocarbon generation and migration in the West Netherlands Basin, the Netherlands. Netherlands Journal of Geosciences 79, 29-44.

Van Balen, R.T., Houtgast, R.F., Van der Wateren, F.M., Vandenberghe, J., 2002. Neotectonic evolution and sediment budget of the Meuse catchment in the Ardennes and the Roer Valley Rift System. Netherlands Journal of Geosciences 81, 211-215.

van Balen, R.T., Houtgast, R.F., Cloetingh, S.A.P.L., 2005. Neotectonics of The Netherlands: a review. Quaternary Science Reviews 24, 439-454.

Barr, D. 1987. Lithospheric stretching, detached normal faulting and footwall uplift. in: M. P. Coward, J. F. Dewey and P. L. Hancock (eds.) Continental Extensional Tectonics. 28. 75-94.

Van Bergen, F., 1998. Basin modelling and hydrocarbon generation in the WNB-an organic petrological and organic geochemical approach (Internal report No. 98-148B). Netherlands Institute fo Applied Geoscicence TNO - National Geological Survel, Utrecht.

Van Bergen, M.J., Sissingh, W., 2007. Magmatism in the Netherlands:expression of the north-west European rifting history, in: Wong, T.E., Batjes, D.A.J., De Jager, J. (Eds.), Geology of the Netherlands. Royal Dutch Academy of Arts and Sciences, Amsterdam, pp. 197-222.

Calignano, E., 2009 Terschelling Basin and southern Dutch Central Graben present-day heat flow modeling. TNO internal report

Crowley, K. d, Cameron, M., Schaefer, R. l, 1991. Experimental studies of annealing of etched fission tracks in fluorapatite. Geochimica et Cosmochimica Acta 55, 1449-1465.

Donders, T.H., Weijers, J.W.H., Munsterman, D.K., Kloosterboer-van Hoeve, M.L., Buckles, L.K., Pancost, R.D., Schouten, S., Sinninghe Damste, J.S., Brinkhuis, H., 2009. Strong climate coupling of terrestrial and marine environments in the Miocene of northwest Europe. Earth and Planetary Science Letters 281, 215-225.

Dusar, M., Bless, M.J.M., Burger, K., Demaret, M., Hardy, M., Langenaeker, V., Lie, S.F., Paproth, E., Piérart, E., Somers, Y., Streel, M., Wouters, L., 1998. De steenkool verkenningsboring Hechtel-Hoef (No. 286), Geological Survey Belgium Professional Paper.

Geluk, M.C., 1990. The Cenozoic Roer Valley Graben, southern Netherlands. Mededelingen Rijks Geologische Dienst 44, 65-72.

Geluk, M.C., Duin, E.J.T., Dusar, M., Rijkers, R.H.B., Berg, M.W. v d, Rooijen, P. v, 1994. Stratigraphy and tectonics of the Roer Valley Graben. Geologie en Mijnbouw 73, 129-141.

Gradstein, F.M., Ogg, J.G., Smith, A.G., 2004. A Geologic Time Scale 2004. Cambridge University Press, Cambridge.

Green, P.F., Moore, M.E., 1992. Thermal history reconstruction in four onshore netherlands wells using apatite fission track analysis and vitrinite reflectance (No. 393), Geotrack. Clyde Petroleum Exploratie BV, Den Haag.

Herngreen, G.F.W., Kouwe, W.F.P., Wong, T.E., 2003. The Jurassic in the Netherlands, in: Ineson, J.R., Surlyk, F. (Eds.), The Jurassic of Denmark and Greenland. Geological Survey of Denmark and Greenland Bulletin, -, pp. 217-229.

International Commission on Stratigraphy, 2009. International stratigraphic chart.

De Jager, J., 2003. Inverted basins in the Netherlands, similarities and differences. Netherlands Journal of Geosciences 82, 355-366.

De Jager, J., Doyle, M.A., Grantham, P.J., Mabillard, J.E., 1996. Hydrocarbon habitat of the West Netherlands Basin, in: Rondeel, H.E., Batjes, D.A.J., Nieuwenhuijs, W.H. (Eds.), Geology of gas and oil under the Netherlands. Kluwer Academic Publishers, Dordrecht, pp. 191-210.

De Jager, J., Geluk, M.C., 2007. Petroleum geology, in: Wong, T.E., Batjes, D.A.J., de Jager, J. (Eds.), Geology of the Netherlands. Royal Netherlands Academy of Arts and Sciences, Amsterdam, pp. 241-264.

Ketcham, R.A., Carter, A., Donelick, R.A., Barbarand, J., Hurford, A.J., 2007. Improved modeling of fission-track annealing in apatite. American Mineralogist 92, 799-810.

Ketcham, R.A., Donelick, R.A., Balestrieri, M.L., Zattin, M., 2009. Reproducibility of apatite fission-track length data and thermal history reconstruction. Earth and Planetary Science Letters 284, 504-515.

Kozur, H.W., Bachmann, G.H., 2008. Updated correlation of the Germanic Triassic with the Tethyan scale and assigned numeric ages. Berichte Geol. B.-A. 76, 53-58.

Laslett, G.M., Green, P.F., Duddy, I.R., Gleadow, A.J.W., 1987. Thermal annealing of fission tracks in apatite 2. A quantitative analysis. Chemical Geology: Isotope Geoscience section 65, 1-13.

Littke, R., Bueker, C., Hertle, M., Karg, H., Stroetmann Heinen, V., Oncken, O., 2000. Heat flow evolution, subsidence and erosion in the Rheno-Hercynian orogenic wedge of Central Europe, in: Franke, W., Haak, V., Oncken, O., Tanner, D. (Eds.), Orogenic processes; quantification and modelling in the Variscan Belt. Geological Society Special Publications, London, pp. 231-255.

Lünenschloss, B., Muchez, P., Bayer, U., 2008. Late-Variscan fluid migration at the Variscan thrust front of Eastern Belguim: numerical modelling of the paleothermal and fluid flow field. International Journal of Earth Sciences 97, 1201-1212.

Luijendijk, E., Van Balen, R.T., Ter Voorde, M., Andriessen, P.A.M., 2011. Reconstructing the Late Cretaceous inversion of the Roer Valley Graben (southern Netherlands) using a new model that integrates burial and provenance history with fission track thermochronology. J. Geophys. Res. 116, B06402.

Luijendijk, E., Ter Voorde, M., Van Balen, R., Verweij, H., Simmelink, H., 2010. Thermal state of the Roer Valley Graben, part of the European Cenozoic Rift System. Basin Research doi: 10.1111/j.1365-2117.2010.00466.x.

Munsterman, D.K., Verreussel, R.M.C.H., Mijnlieff, H.F., Witmans, N., Kerstholt-Boegehold, S. Abbink, O.A. (in prep) Revision and update of the Callovian-Ryazanian Stratigraphic Nomenclature in the northern Dutch offshore, i.e. Central Graben Subgroup and Scruff Group. Netherlands Journal of Geosciences

Nelskamp, S., David, P., Littke, R., 2008. A comparison of burial, maturity and temperature histories of selected wells from sedimentary basins in The Netherlands. International Journal of Earth Sciences 97, 931-953.

Sissingh, W., 2004. Palaeozoic and Mesozoic igneous activity in the Netherlands; a tectonomagmatic review. Netherlands Journal of Geosciences 83, 113-134.

Tno, N., 2001. Geological Atlas of the Subsurface of the Netherlands, Explanation to Map Sheets XIII and XIV: Breda-Valkenswaard and Oss-Roermond. Utrecht.

Van Wees, J.D., Van Bergen, F., David, P., Nepveu, M., Beekman, F., Cloetingh, S.A.P.L., Bonté, D., 2009. Probabilistic tectonic heat flow modeling for basin maturation: Assessment method and applications. Marine and Petroleum Geology 26, 536-551.

Verweij, J.M., Souto Carneiro Echternach, M., Witmans, N., Abdul Fattah, R. (in press) Reconstruction of Basal Heat Flow, Surface Temperature, Source rocj Maturity, and Hydrocarbon Generation in Salt-Dominated Dutch Basins, in; Peters, K., Curry, D., Kacewicz, M. (Eds.), Casin and Petroleum System Modeling: 2009 Napa Hedberg Conference/ Hedberg Series No. 4, pp. 1-22.

Winstanley, A.M., 1993. A review of the Triassic play in the Roer Valley Graben, SE onshore Netherlands, in: Parker, J.R. (Ed.), Petroleum Geology of Northwest Europe: Proceedings of the 4th conference. The Geological Society, London, pp. 595-607.

Worum, G., 2004. Modelling of fault reactivation potential and quantification of inversion tectonics in the southern Netherlands.

Worum, G., Michon, L., 2005. Implications of continuous structural inversion in the West Netherlands Basin for understanding controls on Palaeogene deformation in NW Europe. Journal of the Geological Society 162, 73-85.

Worum, G., Michon, L., Van Balen, R.T., Van Wees, J.D., Cloetingh, S., Pagnier, H.J.M., 2005. Pre-Neogene controls on present-day fault activity in the West Netherlands Basin and Roer Valley Rift System (southern Netherlands): role of variations in fault orientation in a uniform low-stress regime. Quaternary Science Reviews 24, 479-490.

Zijerveld, L., Stephenson, R., Cloetingh, S.A.P.L., Duin, E., Berg, M.W. v d, 1992. Subsidence analysis and modelling of the Roer Valley Graben (SE Netherlands). Tectonophysics 208, 159-171.

9 Appendix

9.1 **Appendix 1 Report Floris van Lieshout**

9.2 Appendix 2 Heat flow maps

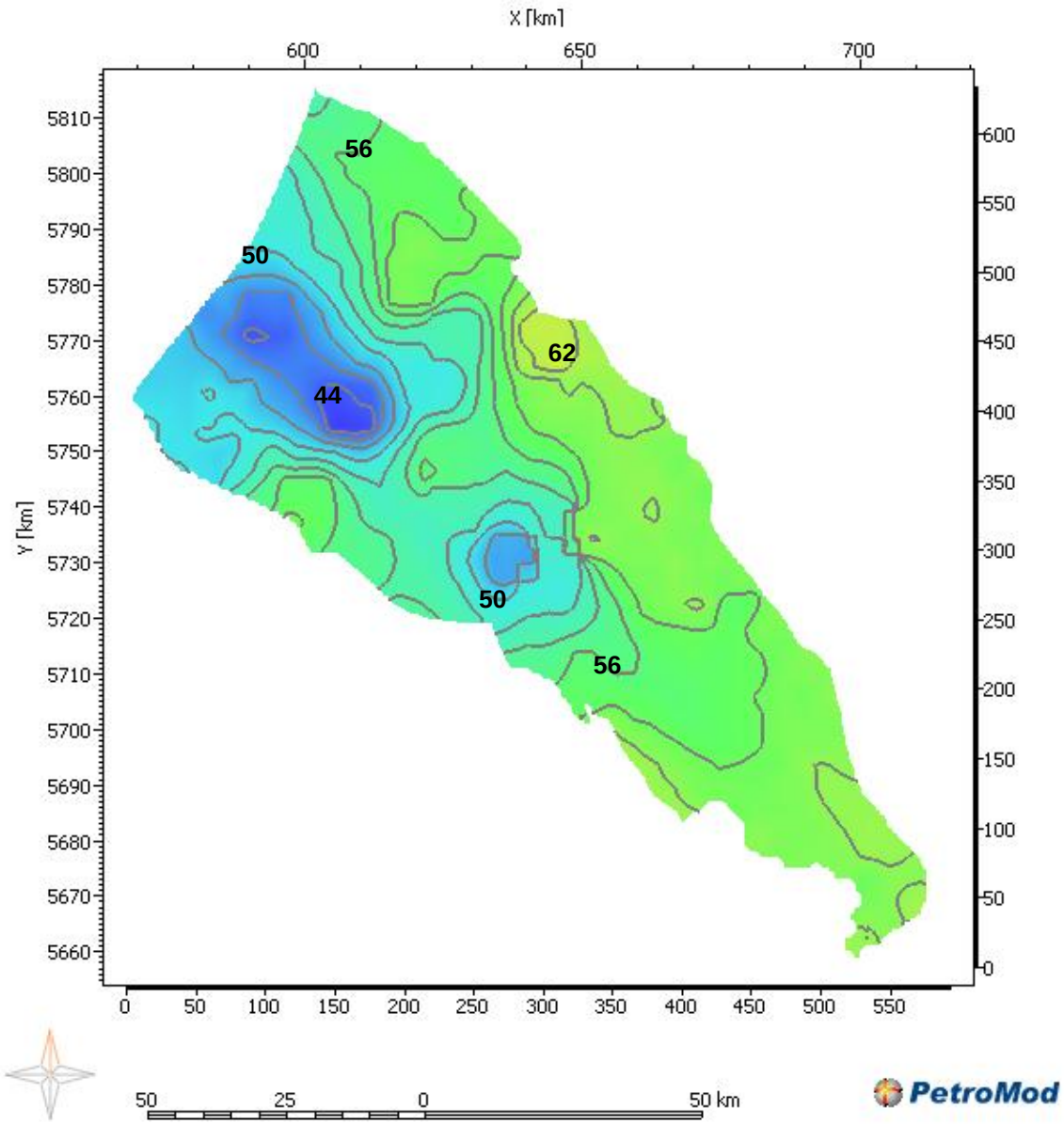

Figure 46 Heat flow map for the present-day situation

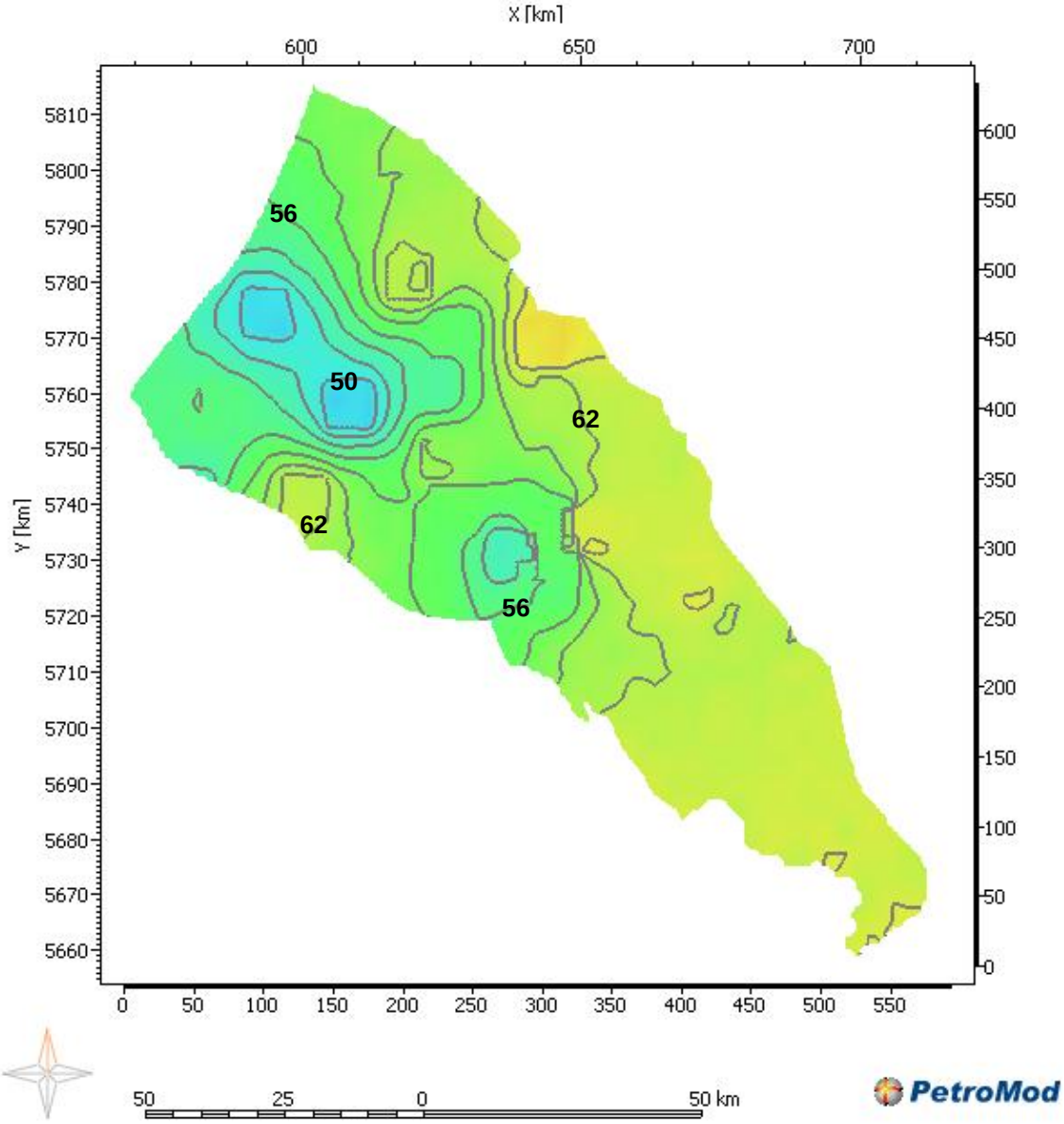

Figure 47 Heat flow map at 258 Ma

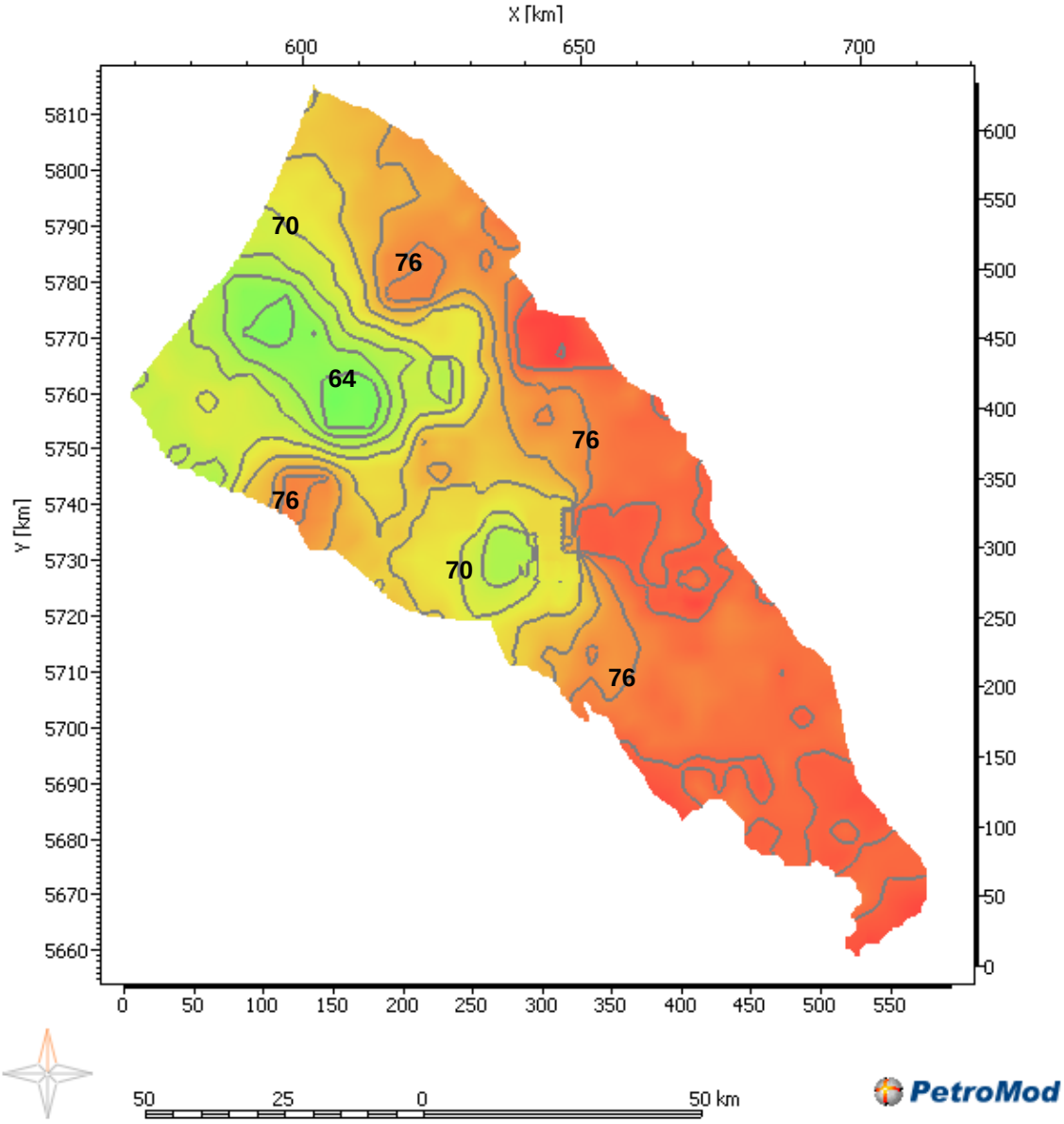

Figure 48 Heat flow map at 290 Ma

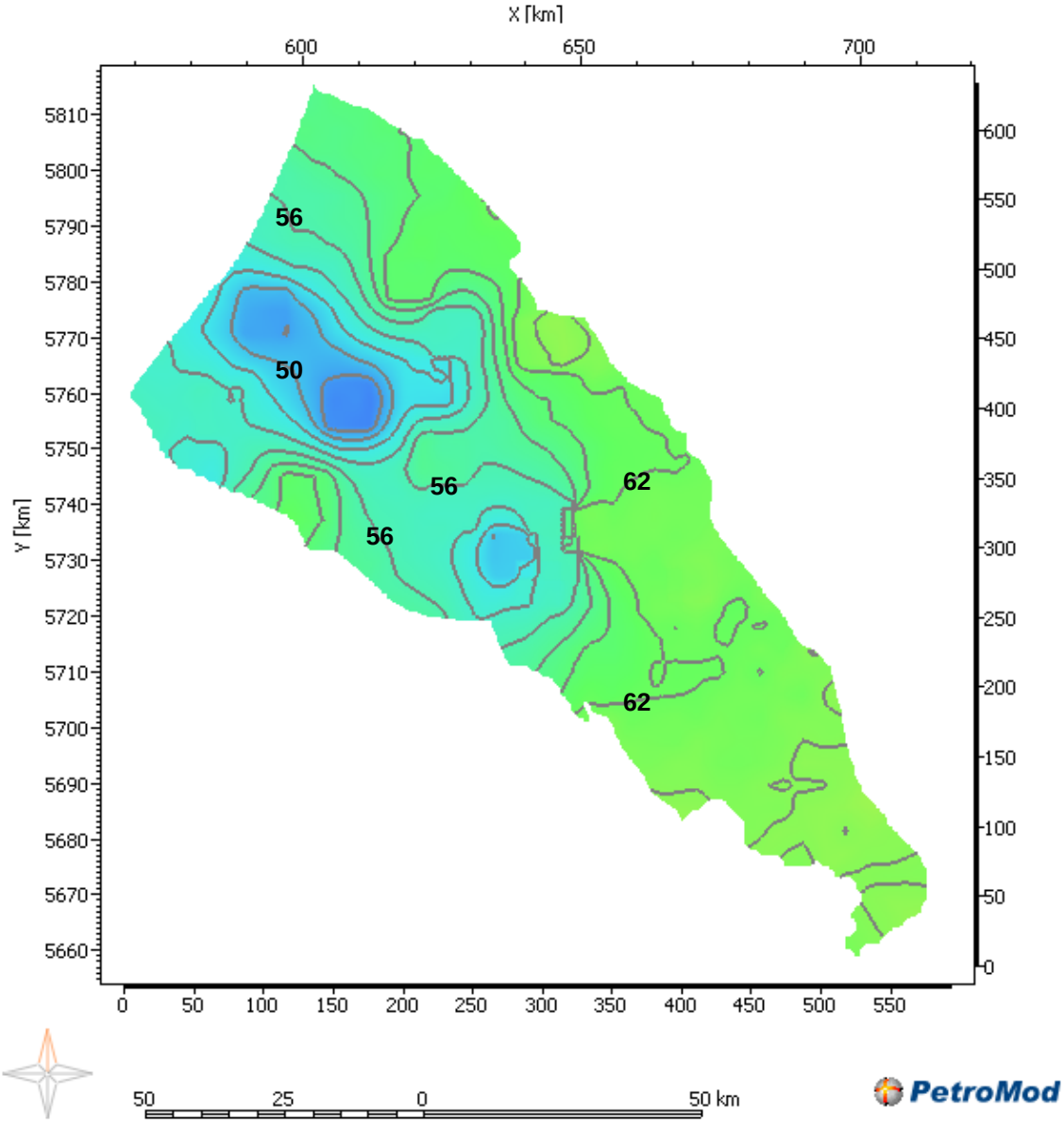

Figure 49 Heat flow map at 308 Ma

9.3 Appendix 3 Erosion maps

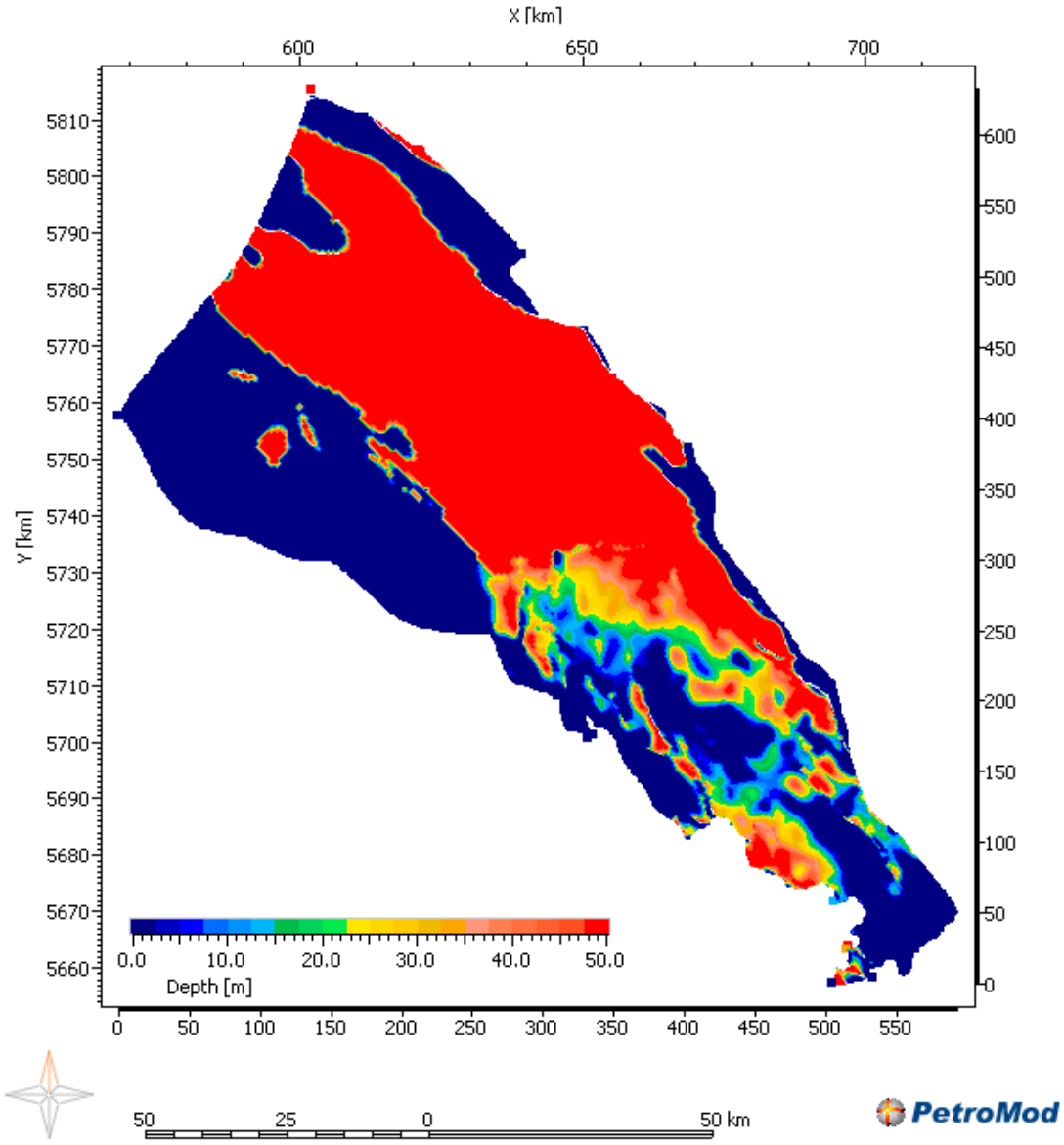

Figure 50 Erosion map of the CKEK formation

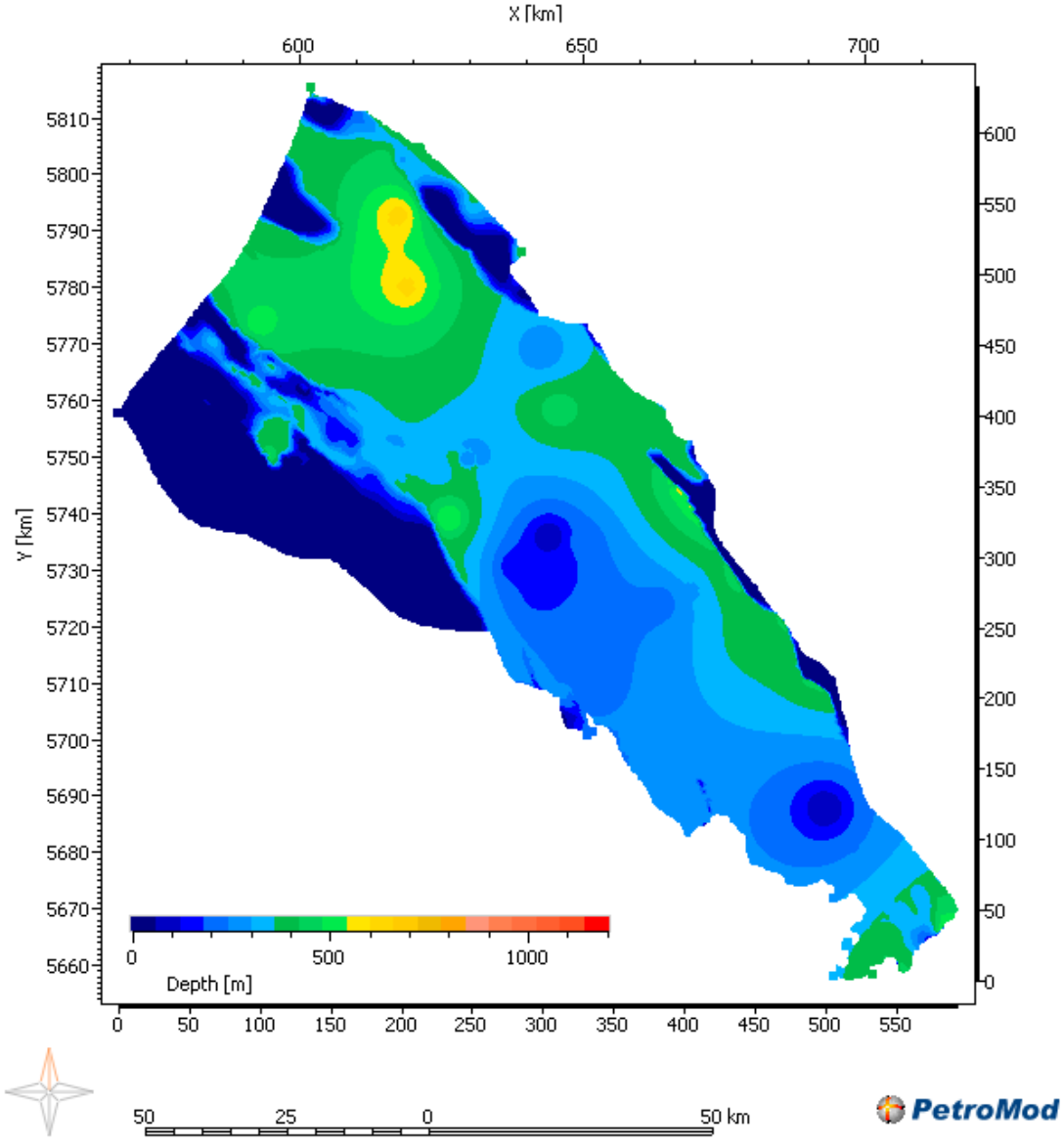

Figure 51 Erosion map of the rest of the CK group

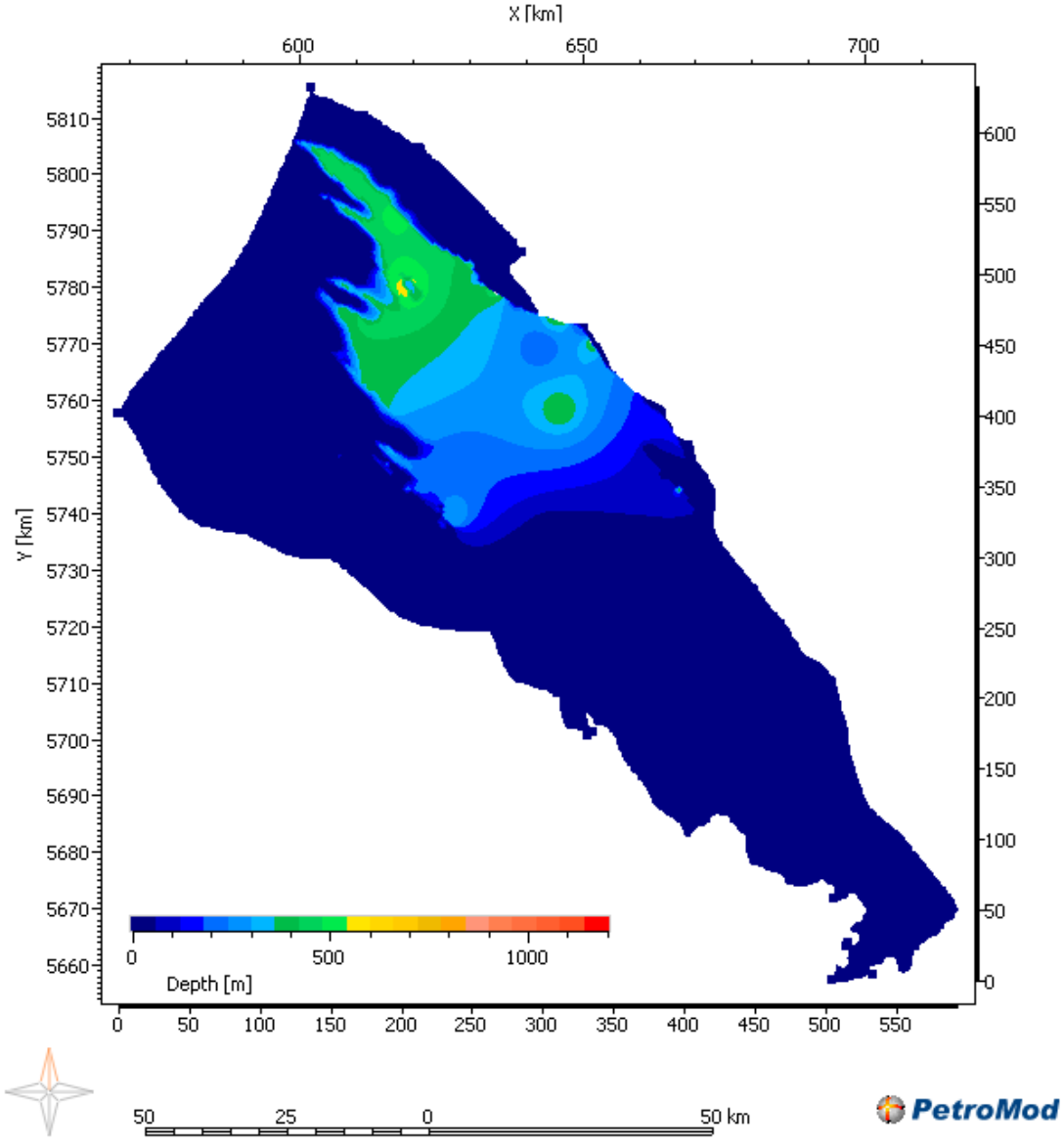

Figure 52 Erosion map of the KN group

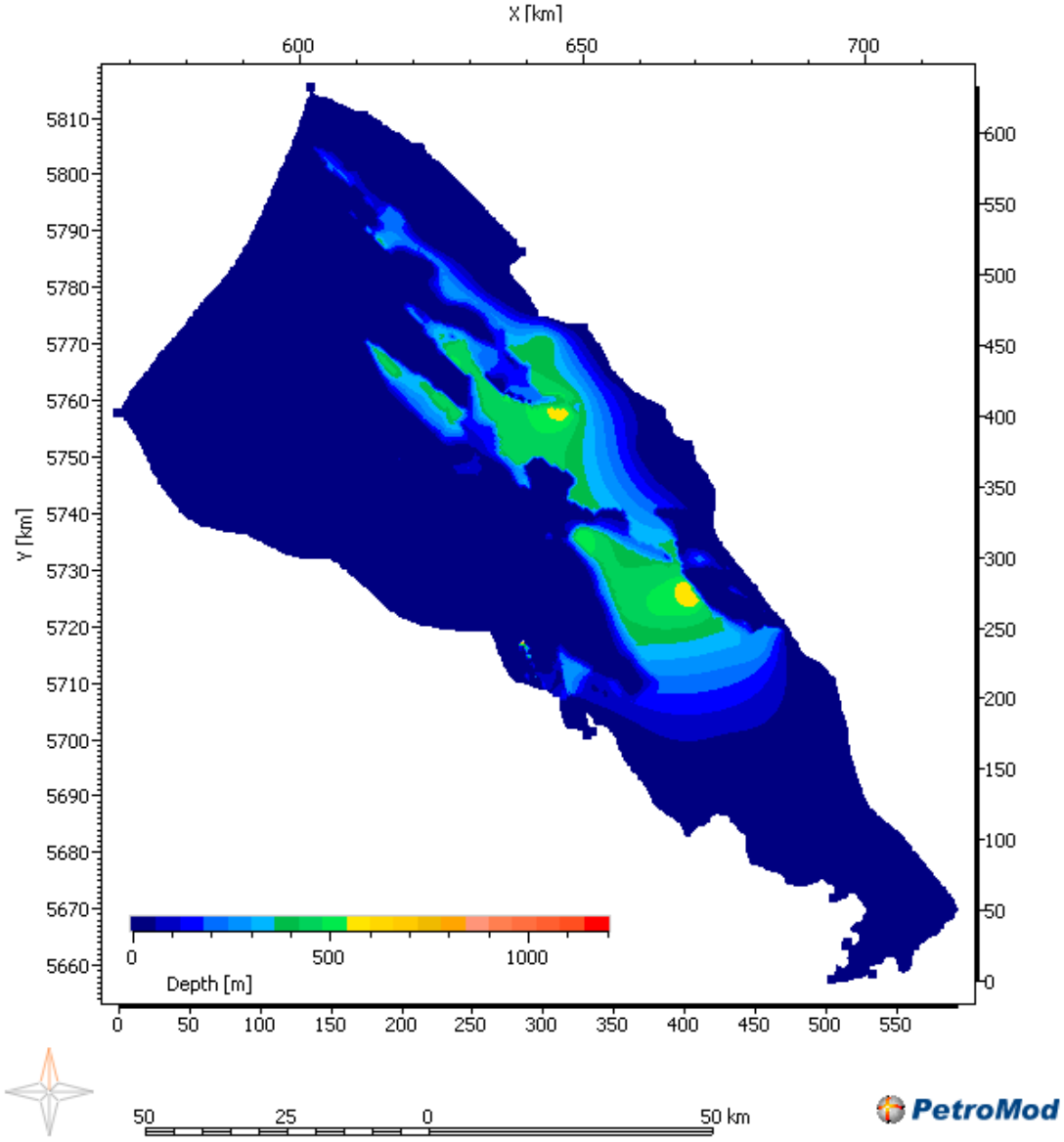

Figure 53 Erosion map of the S group during the Late Cretaceous erosion phase

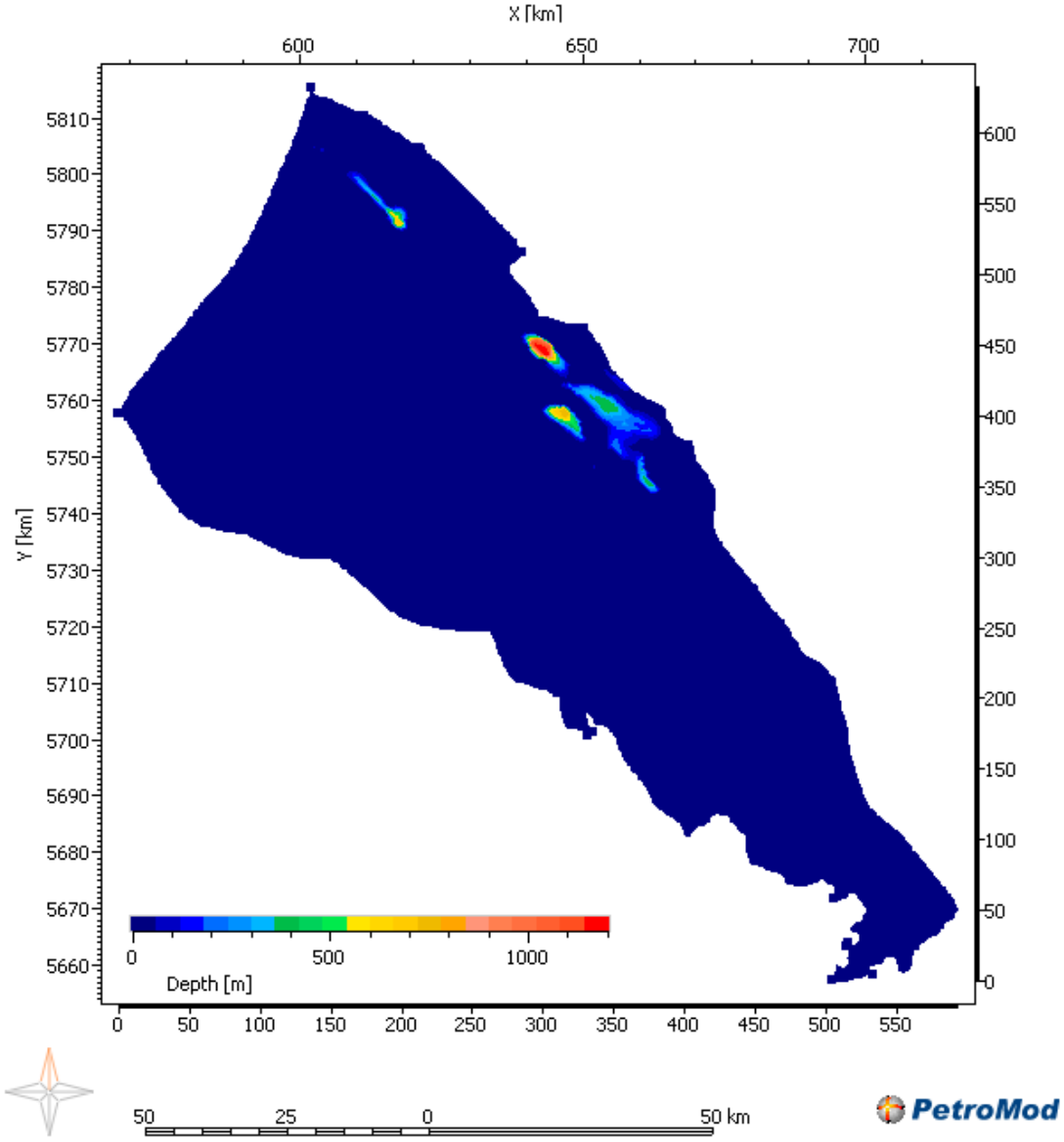

Figure 54 Erosion map of the AT group during the Late Cretaceous erosion phase

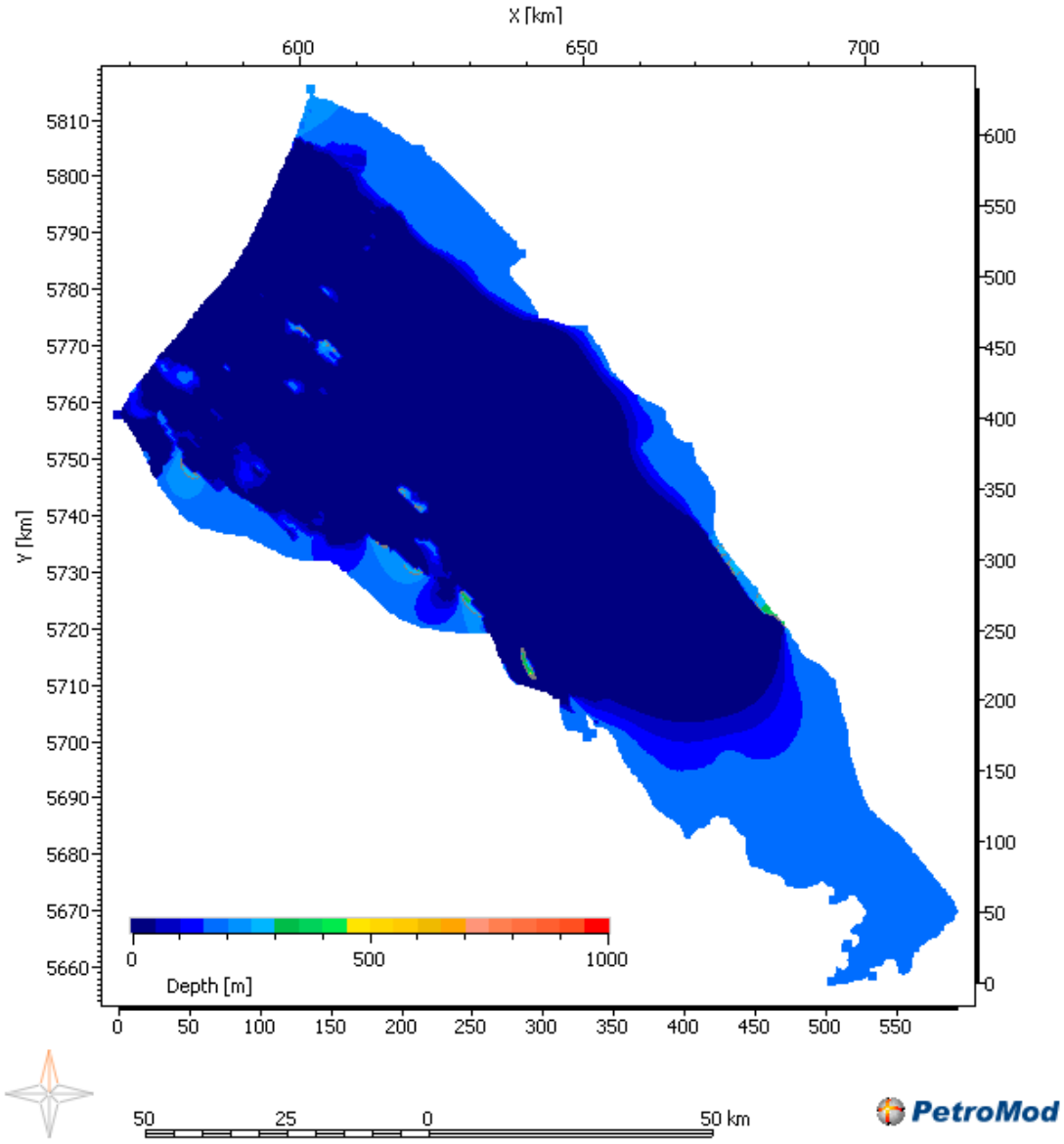

Figure 55 Erosion map of the S group during the Middle to Late Jurassic erosion phase

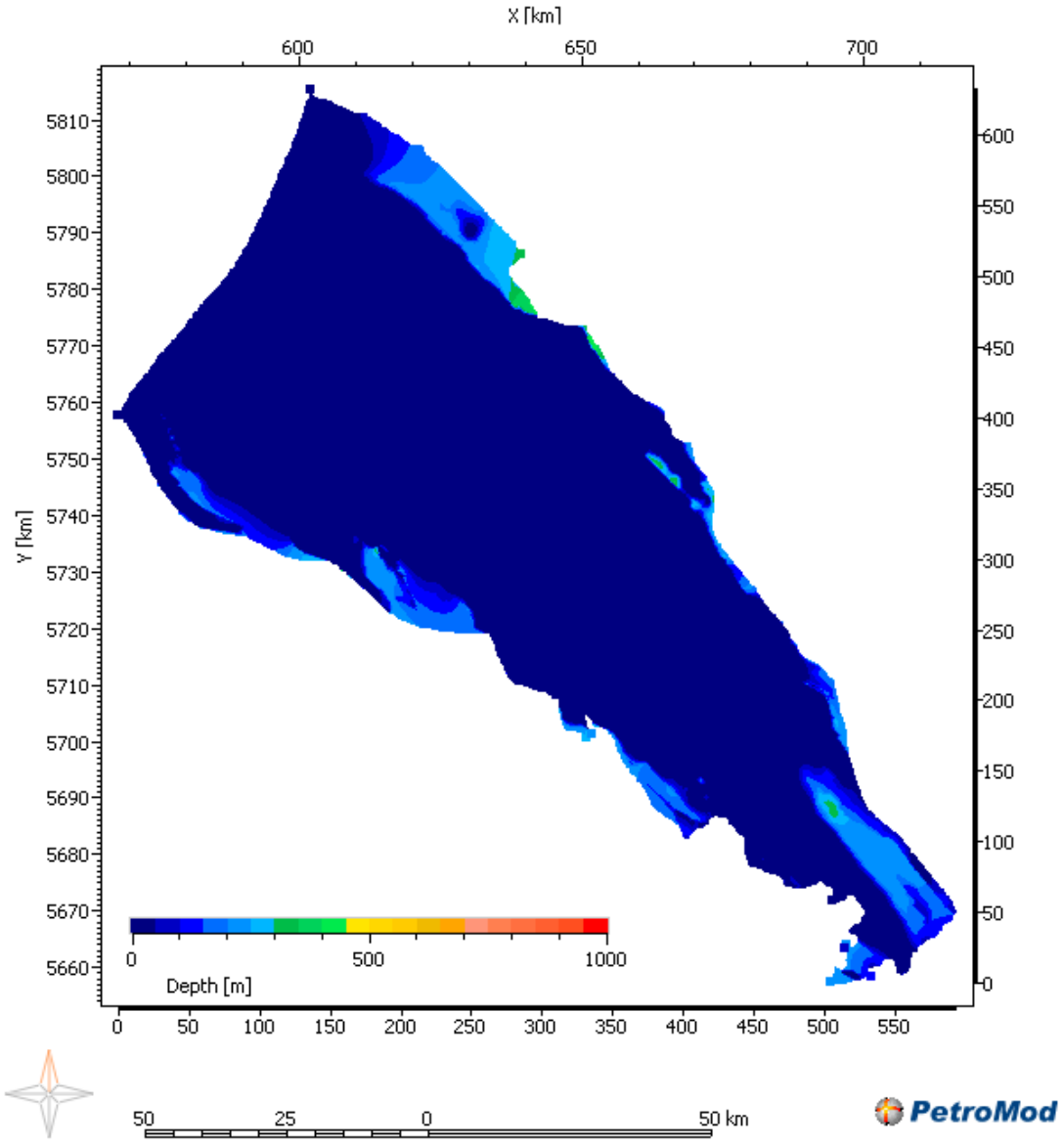

Figure 56 Erosion map of the AT group during the Middle to Late Jurassic erosion phase

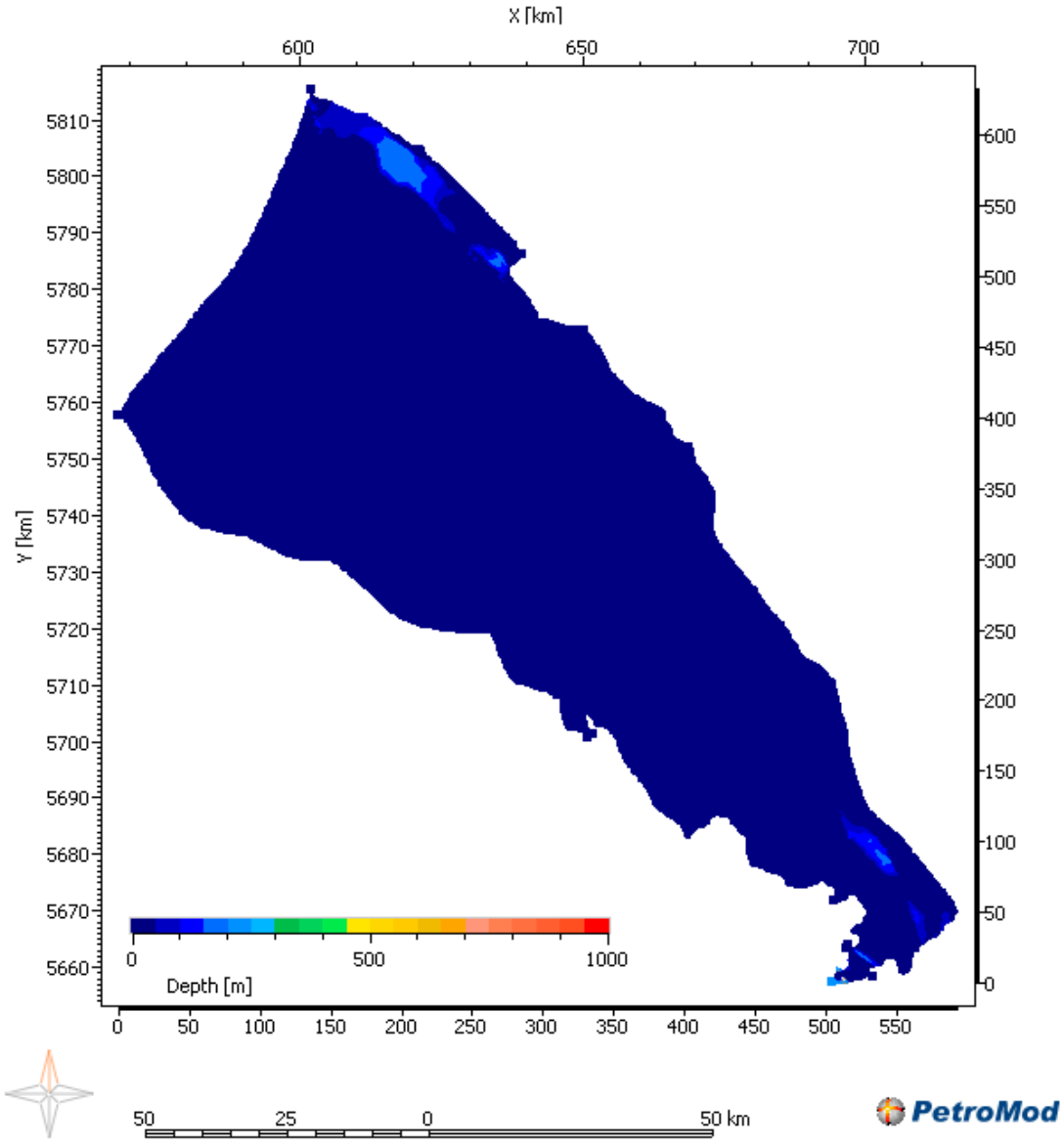

Figure 57 Erosion map of the RN Group during the Middle to Late Jurassic erosion

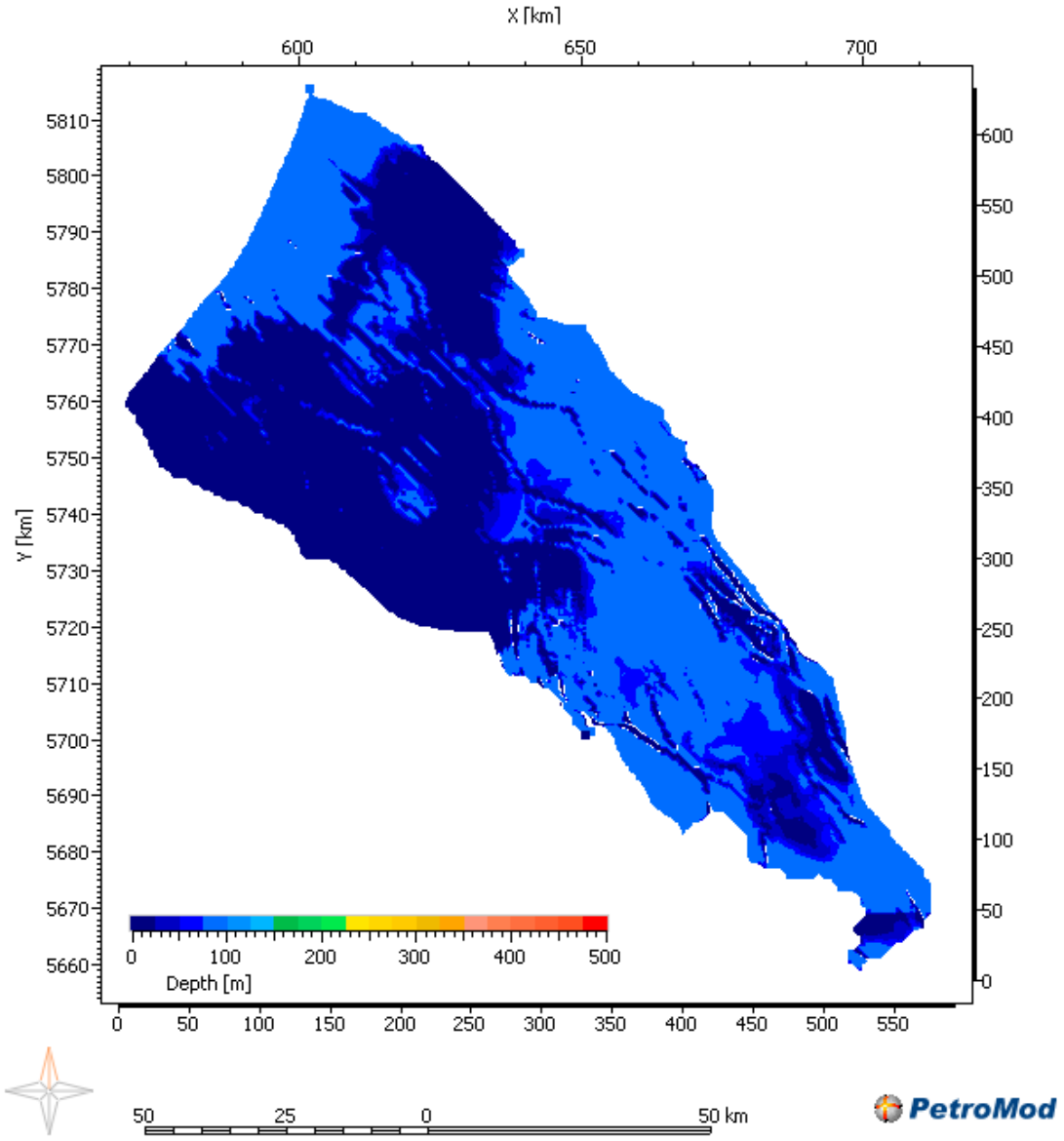

Figure 58 Erosion map of the DCH subgroup during the Early Permian erosion

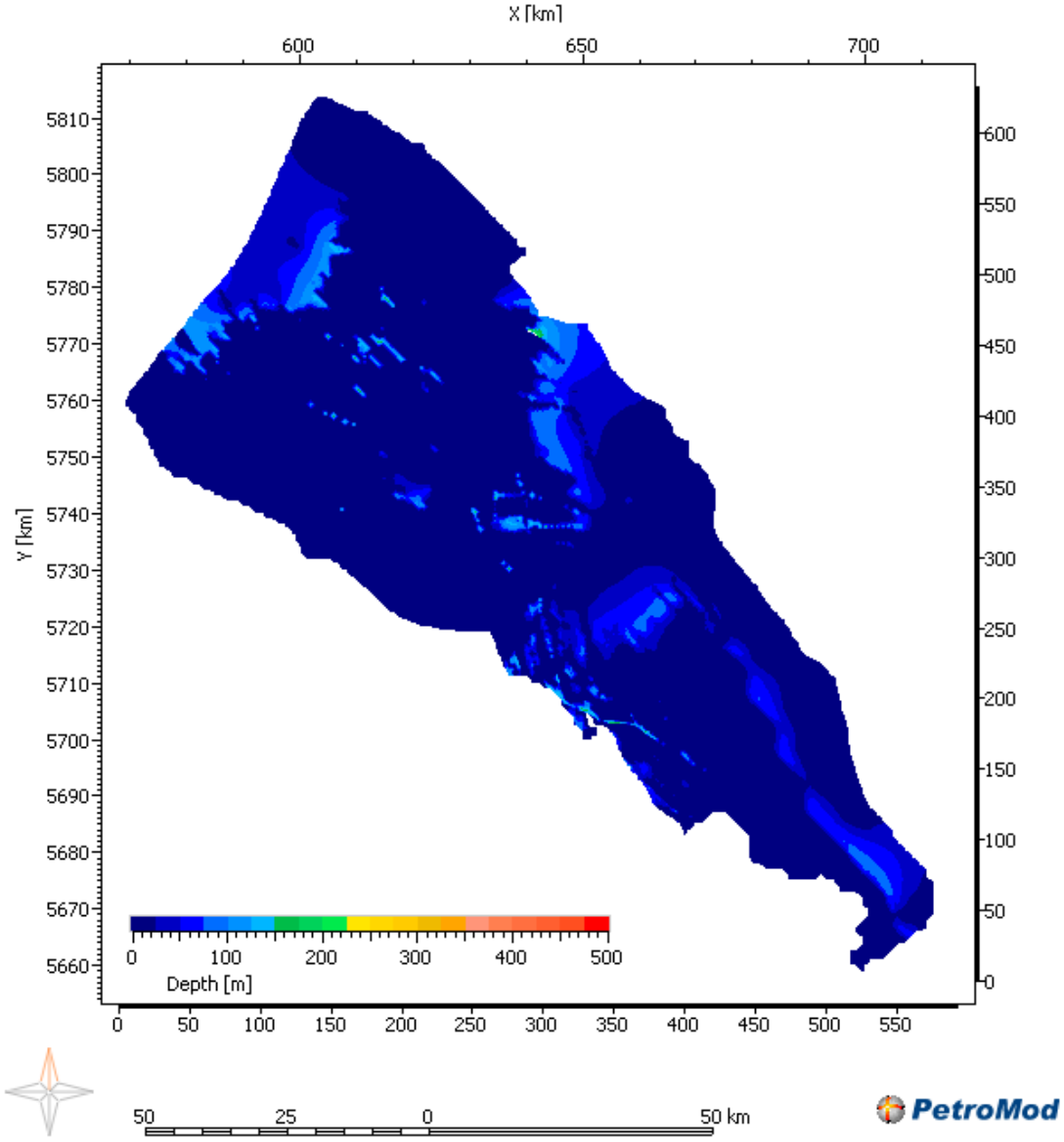

Figure 59 Erosion map of the DCD subgroup during the Early Permian erosion

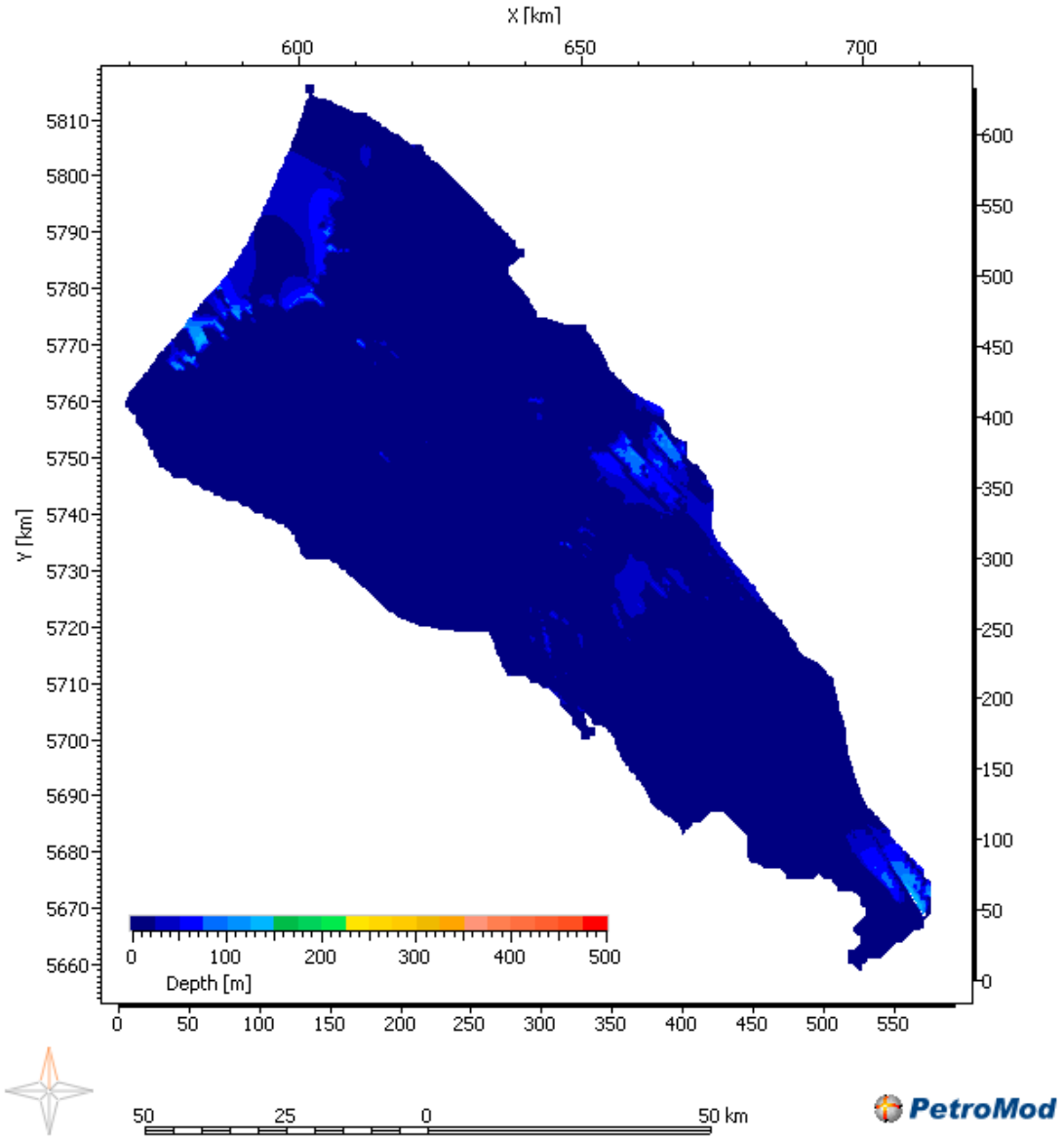

Figure 60 Erosion map of the DCCU formation during the Early Permian erosion

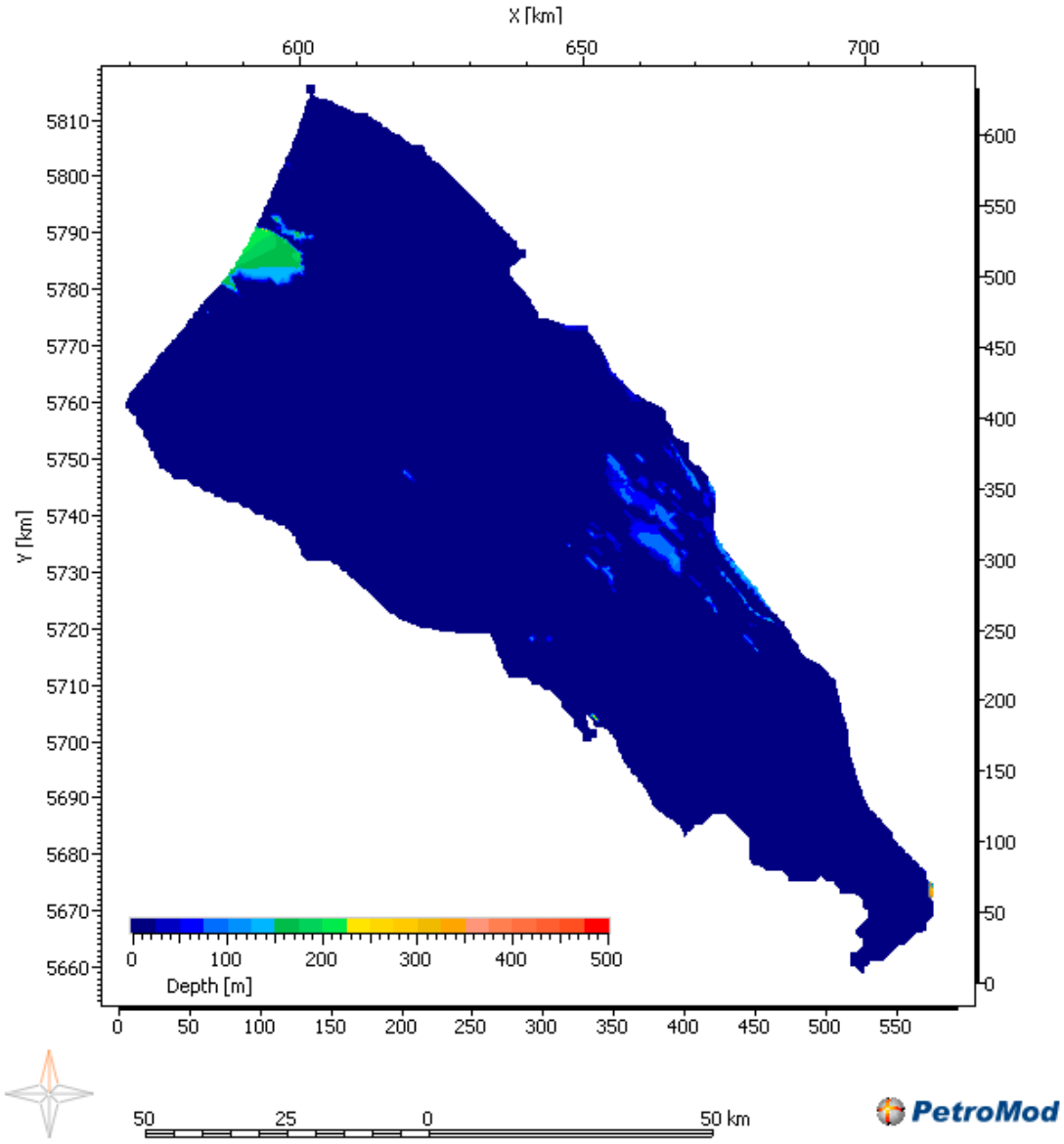

Figure 61 Erosion map of the DCCR formation during the Early Permian erosion

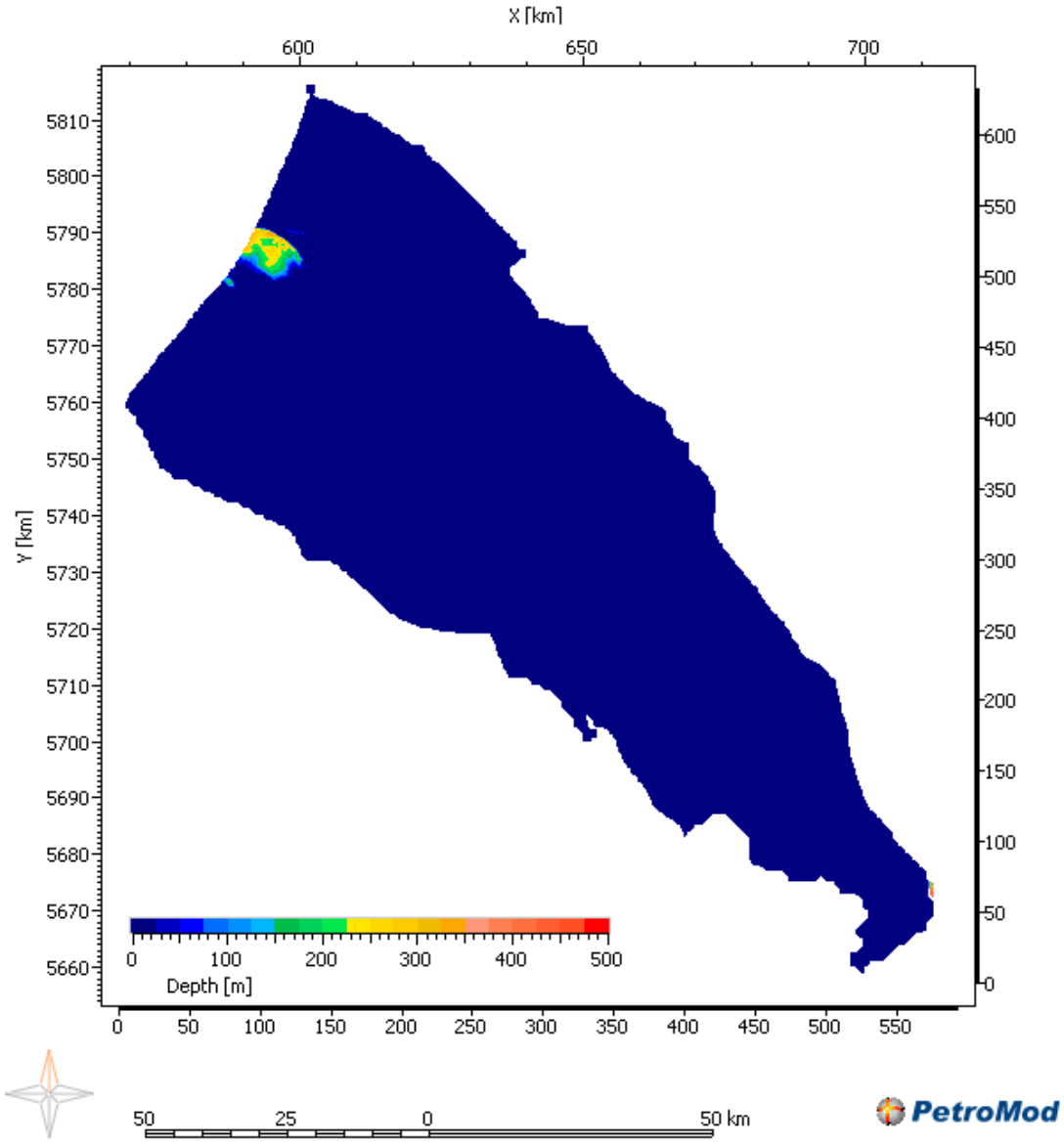

Figure 62 Erosion map of the DCCB formation during the Early Permian erosion

9.4 Appendix 4 Porosity influence of the burial anomaly on different reservoir layers

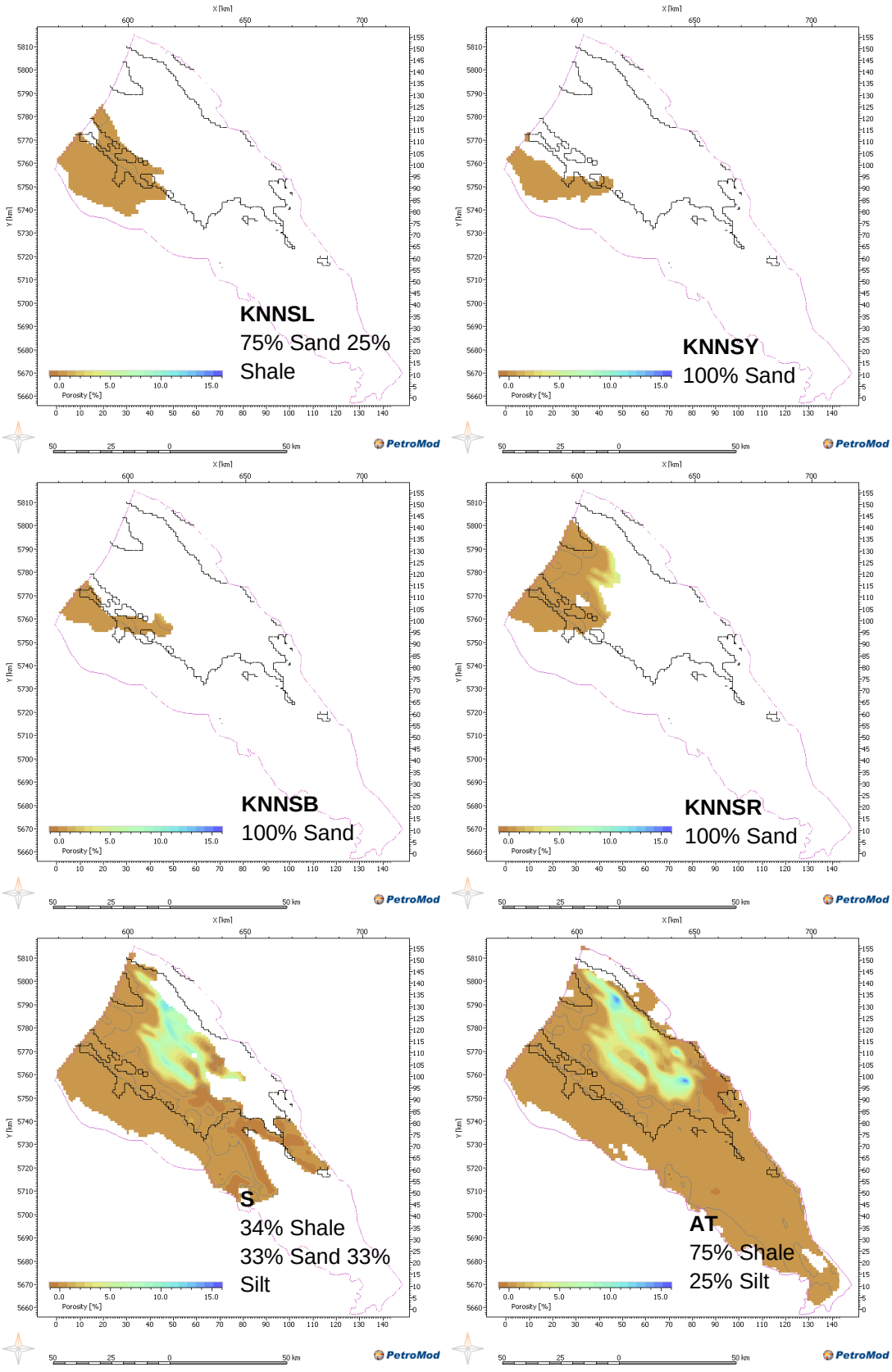

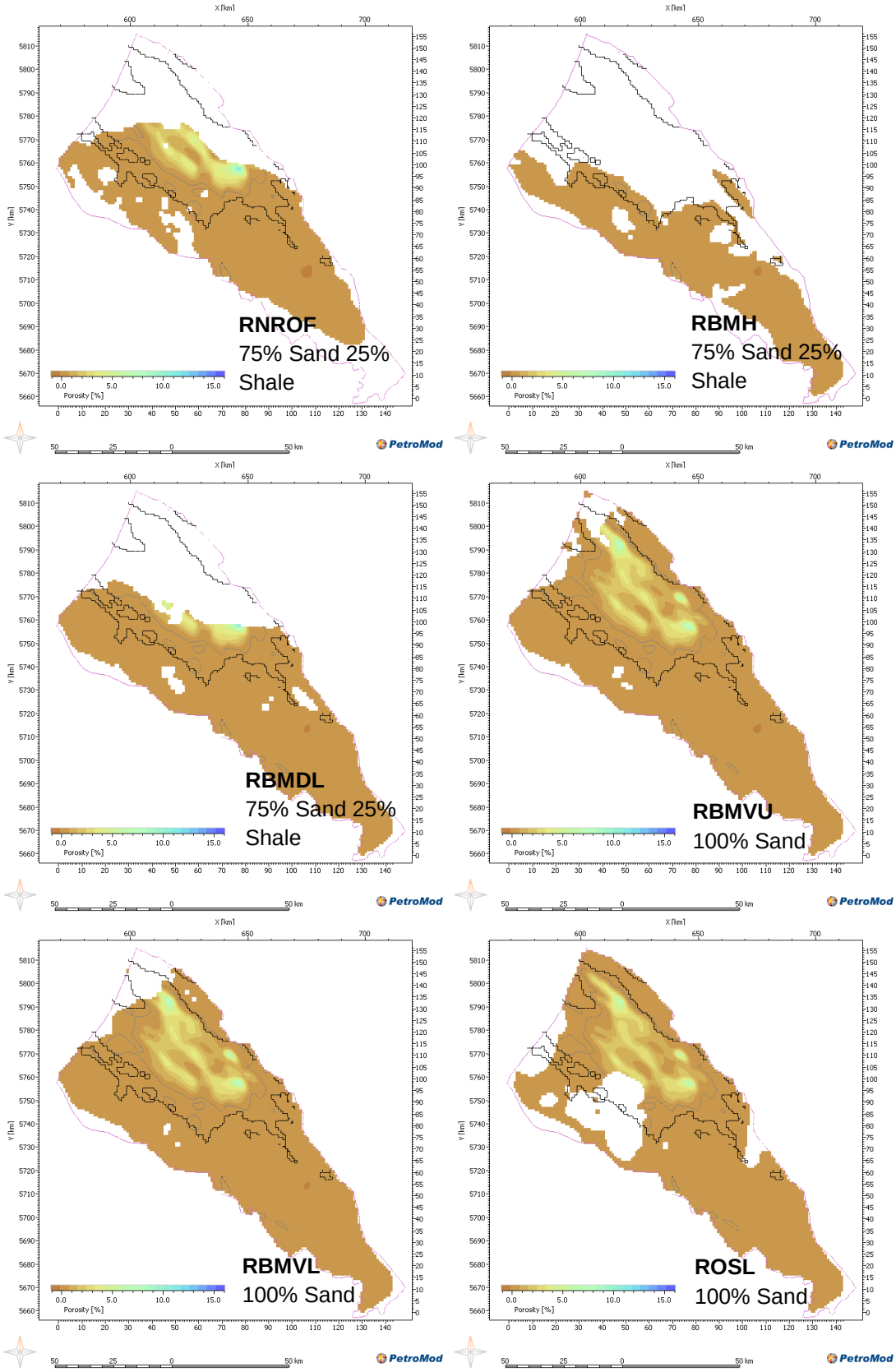

Figure 63 Difference in calculated porosity for a model with and without erosion. The outline of the burial anomaly region is displayed in black

9.5 Appendix 5 Permeability maps of the reservoir layers

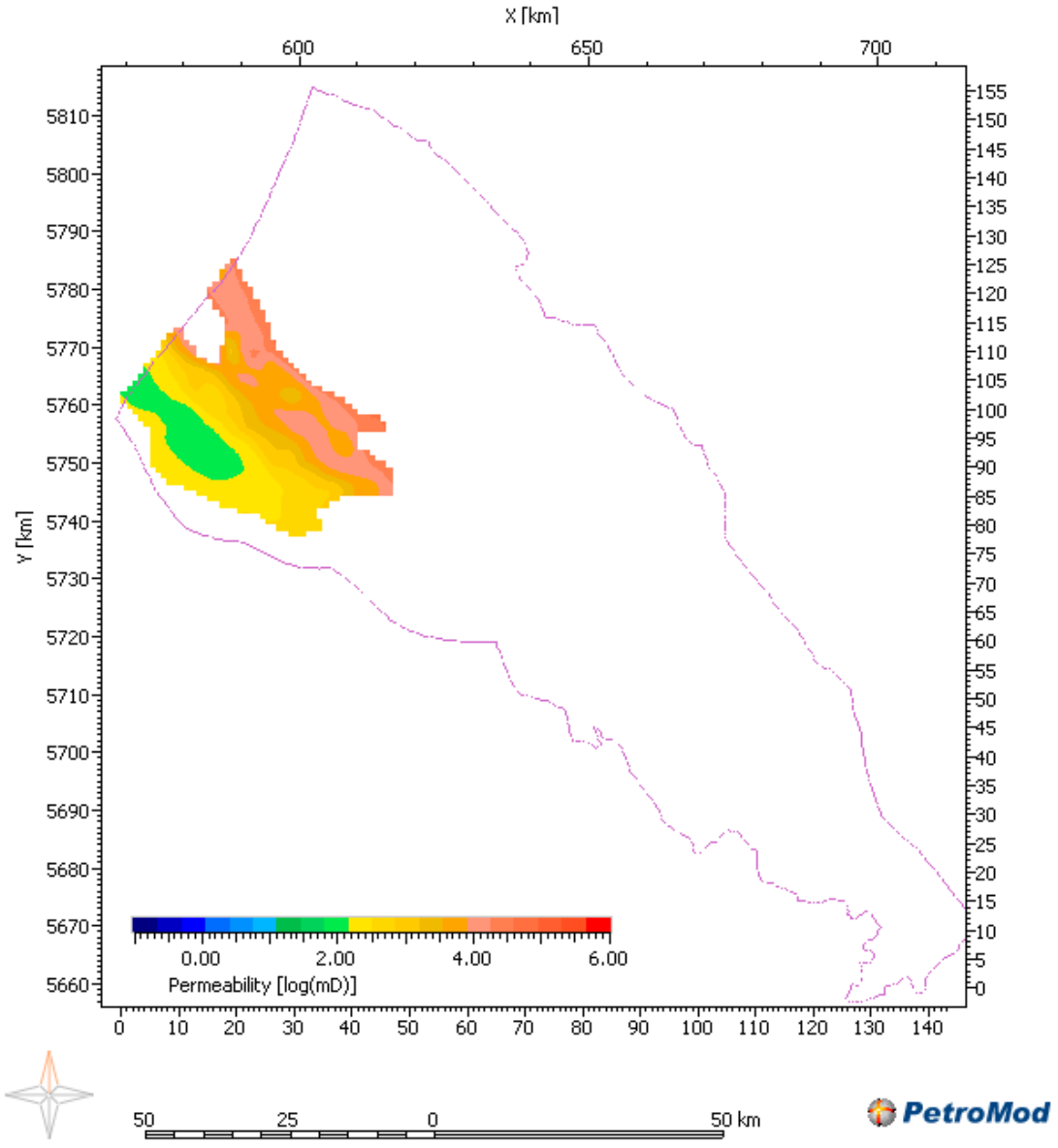

Figure 64 Calculated permeability of layer KNNSC

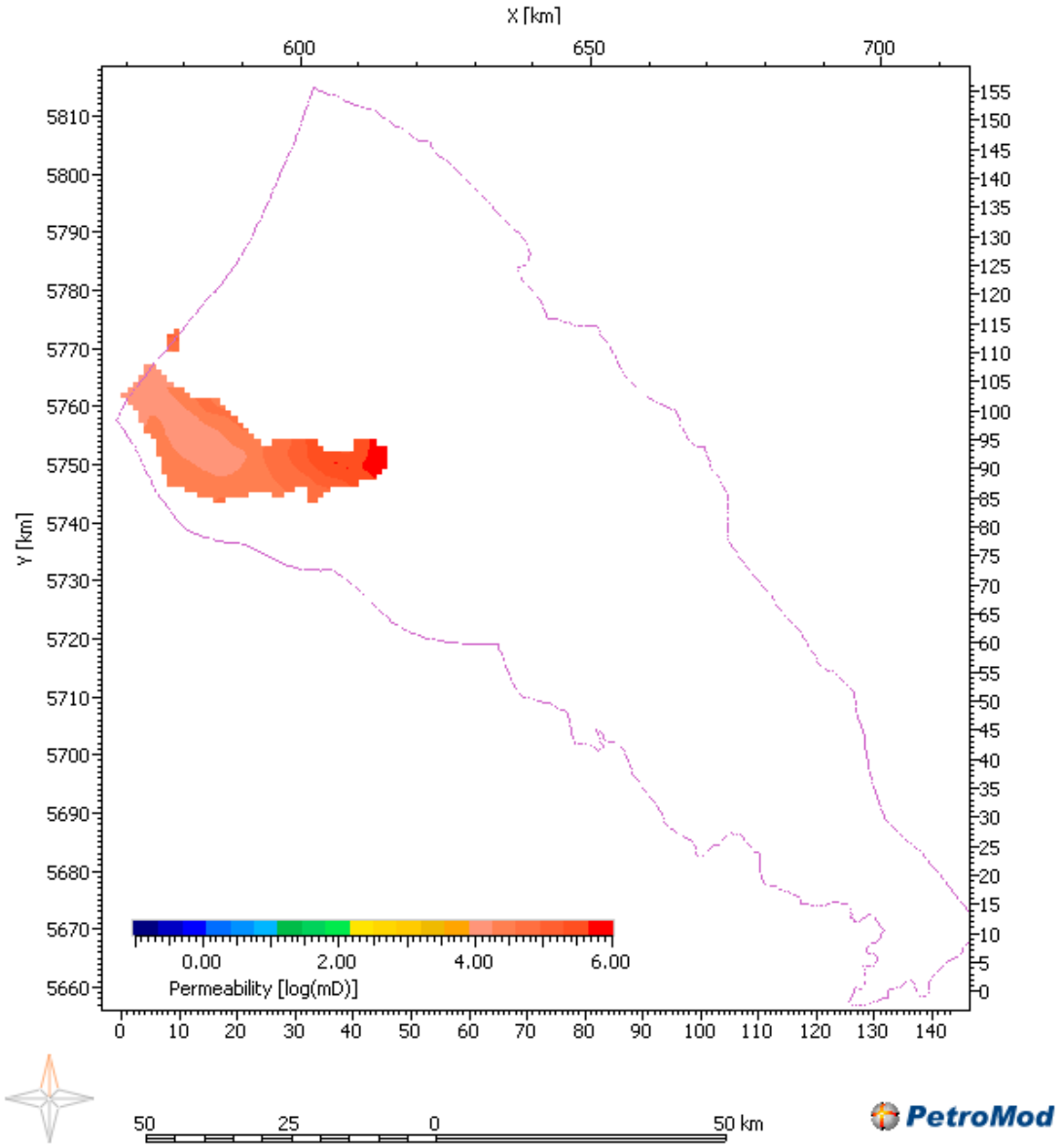

Figure 65 Calculated permeability of layer KNNSY

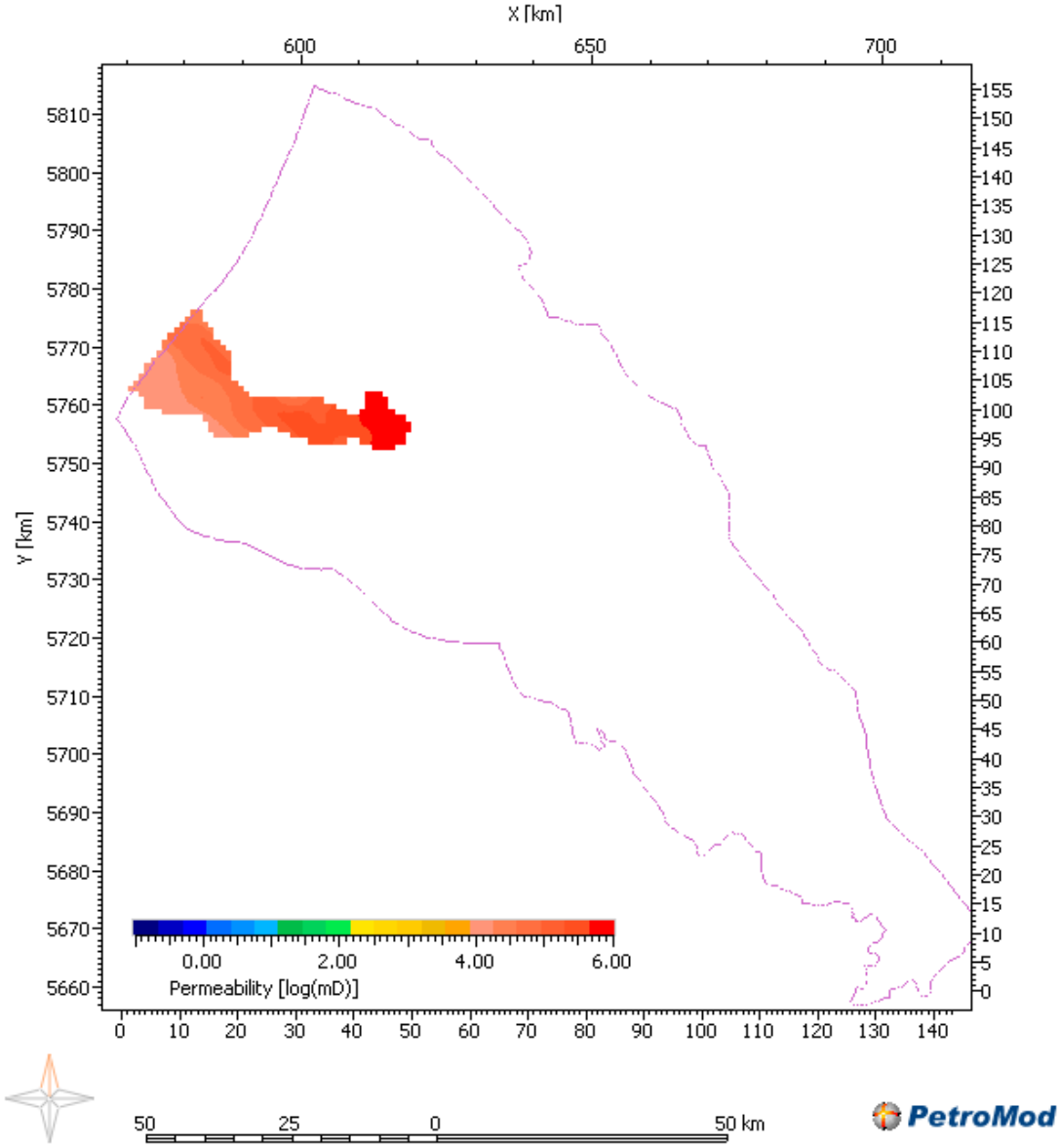

Figure 66 Calculated permeability of layer KNNSB

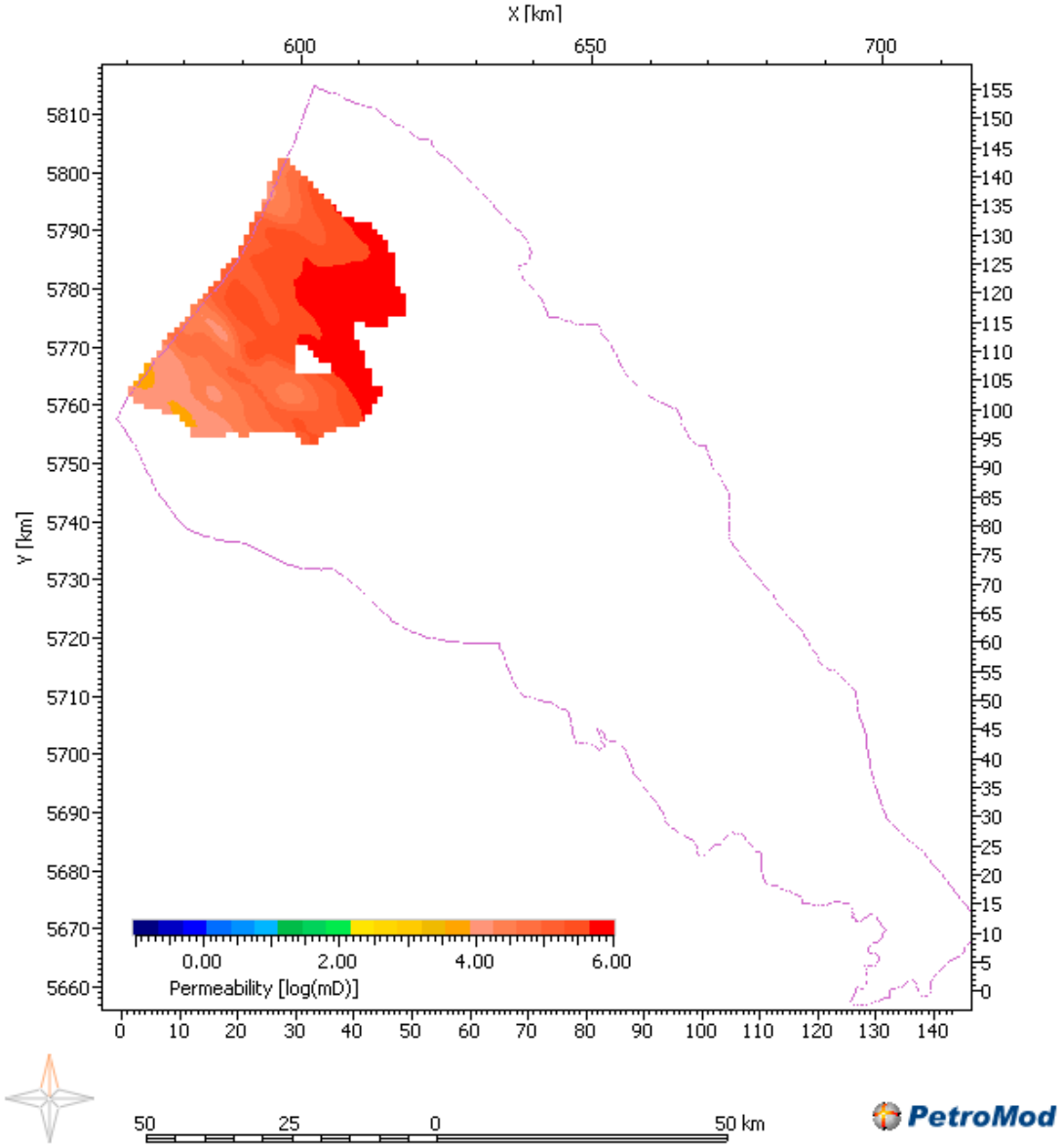

Figure 67 Calculated permeability of layer KNNSR

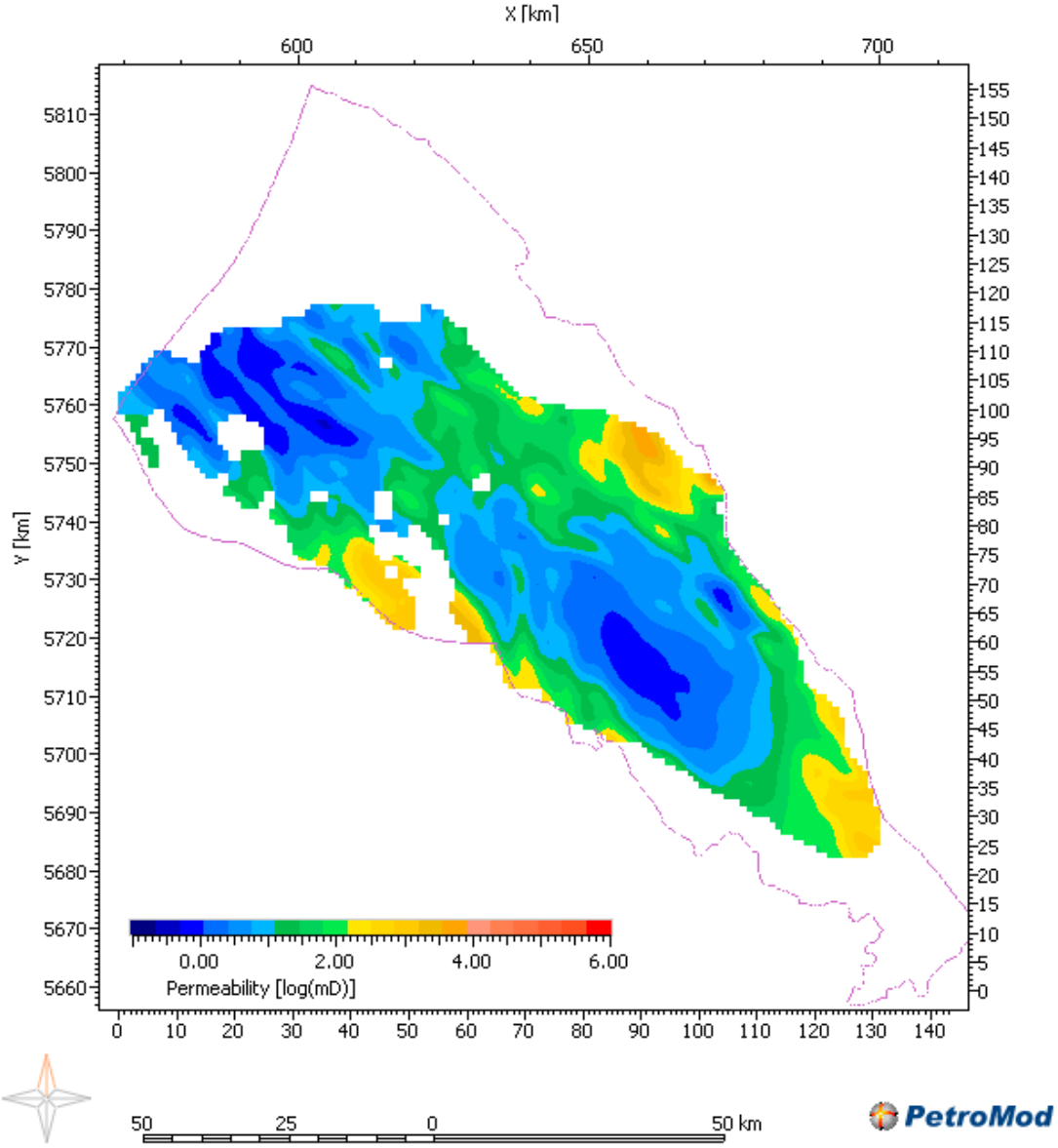

Figure 68 Calculated permeability of layer RNROF

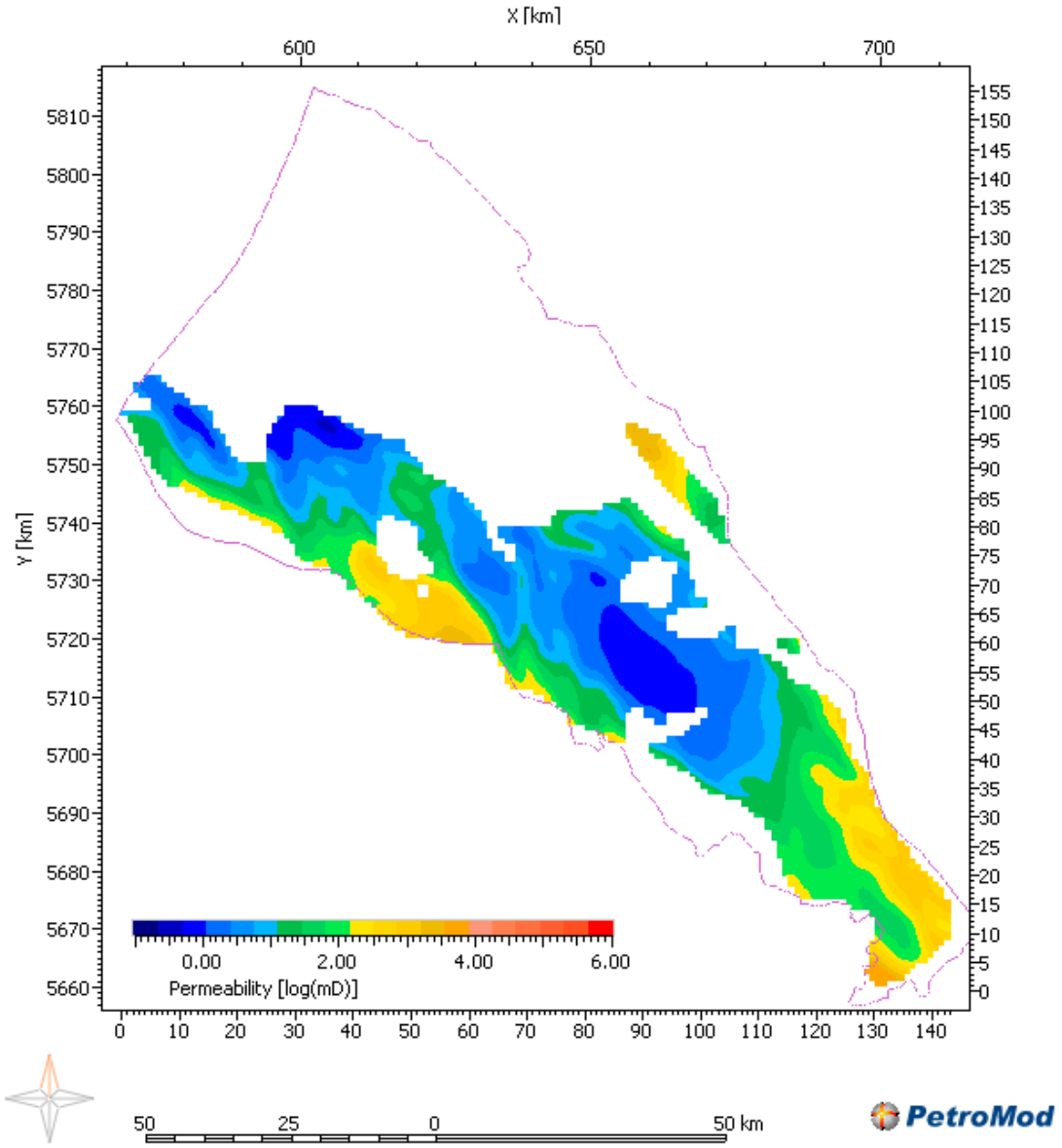

Figure 69 Calculated permeability of layer RBMH

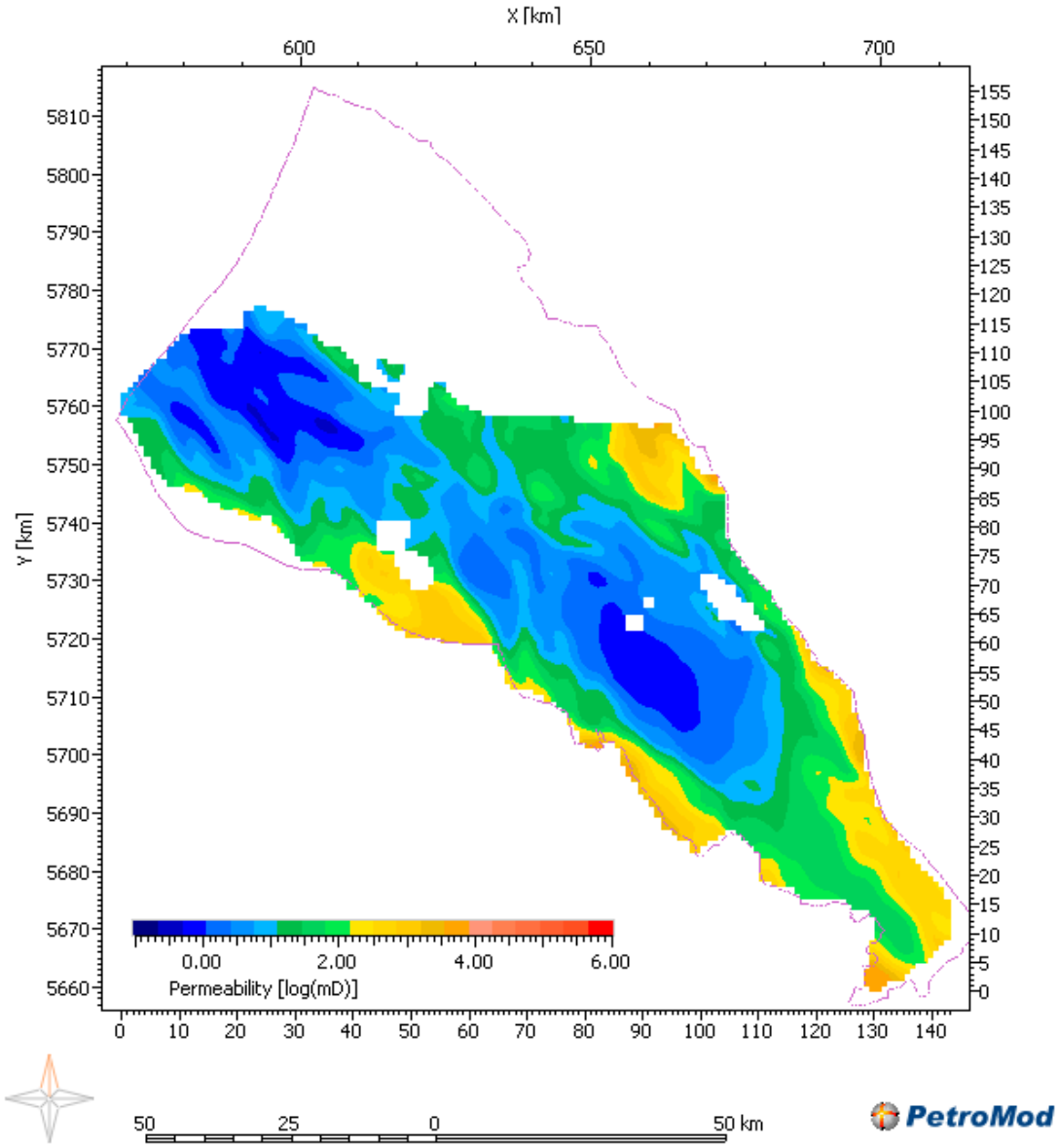

Figure 70 Calculated permeability of layer RBMDL

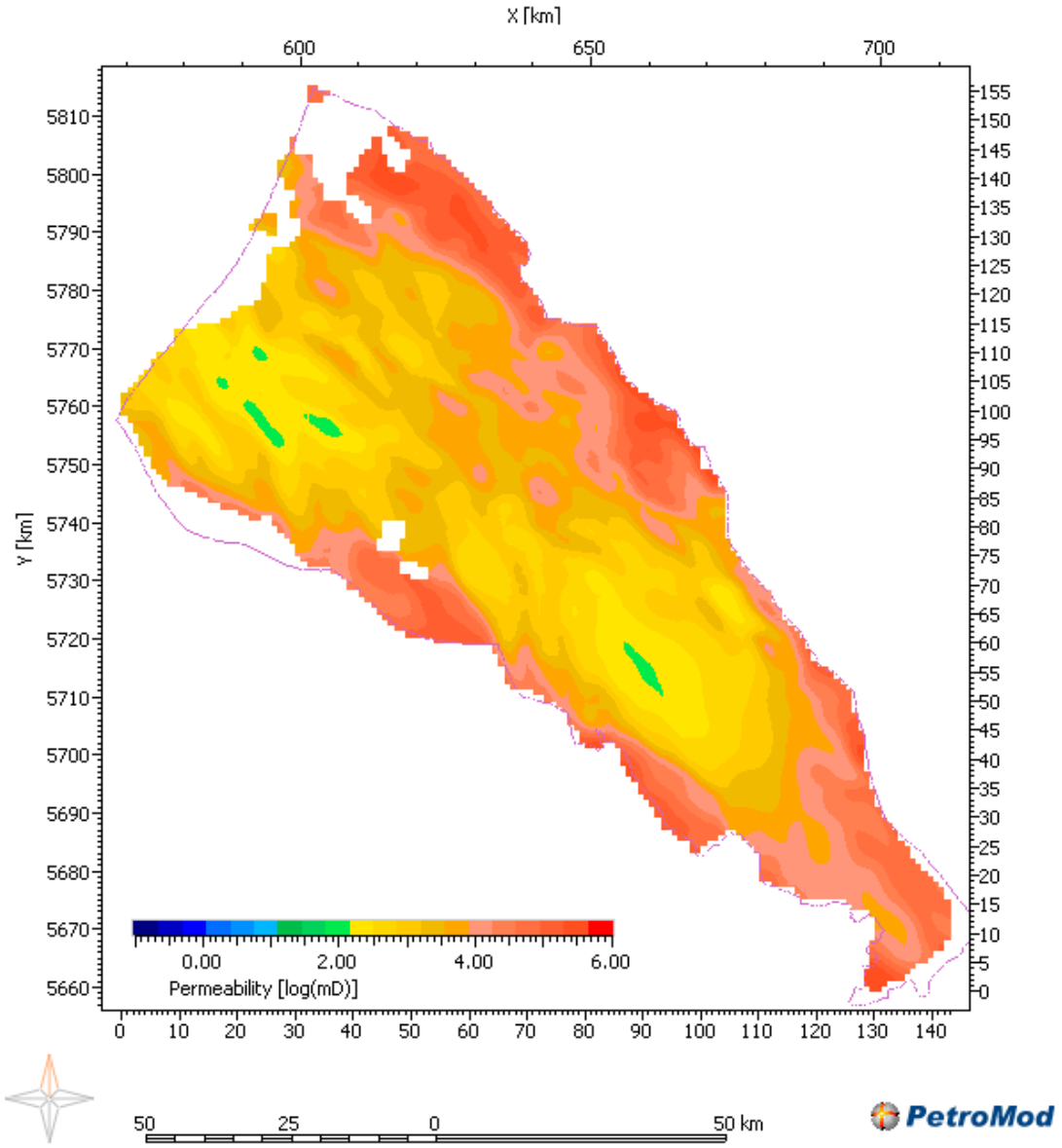

Figure 71 Calculated permeability of layer RBMVU

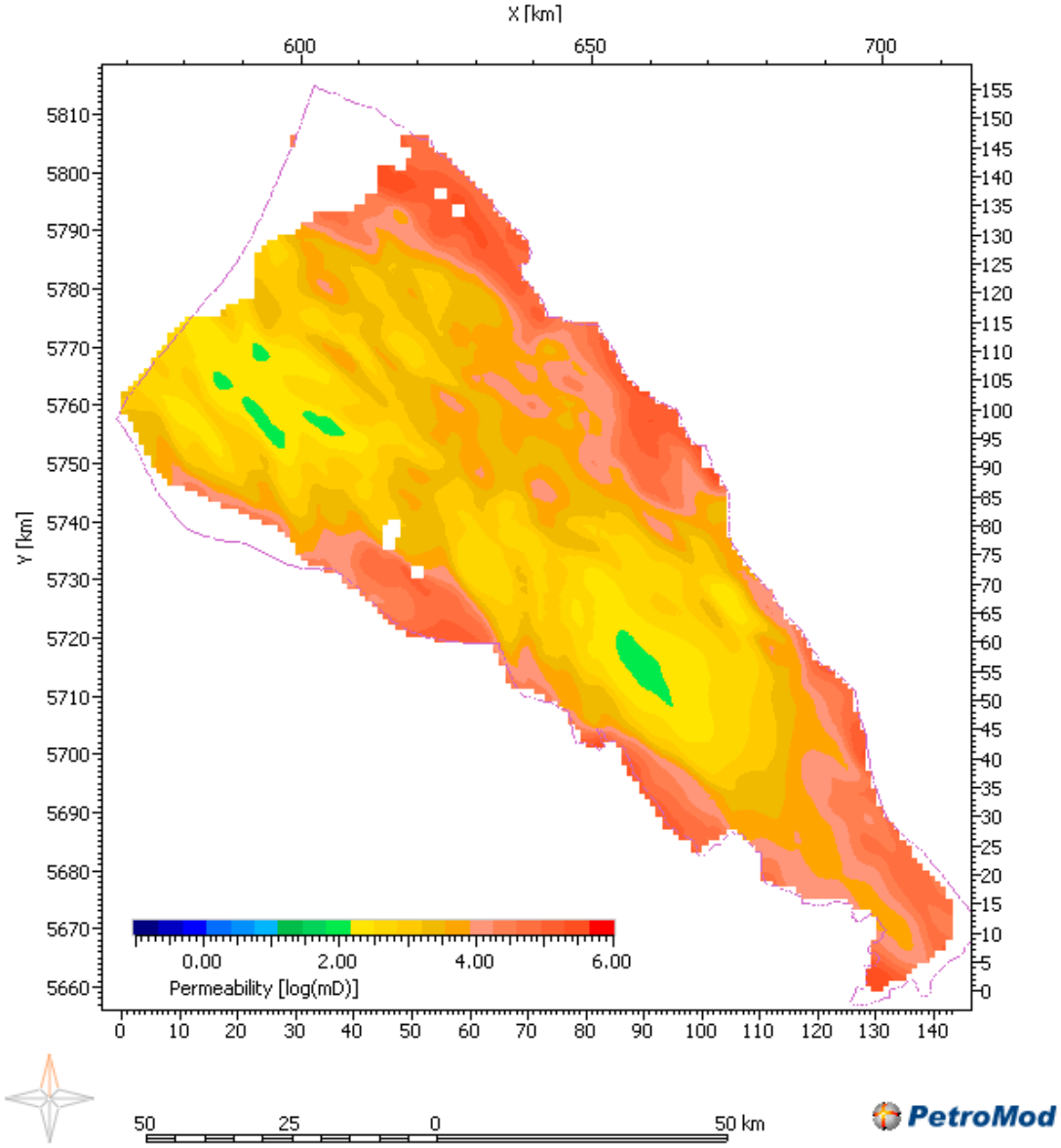

Figure 72 Calculated permeability of layer RBMVL

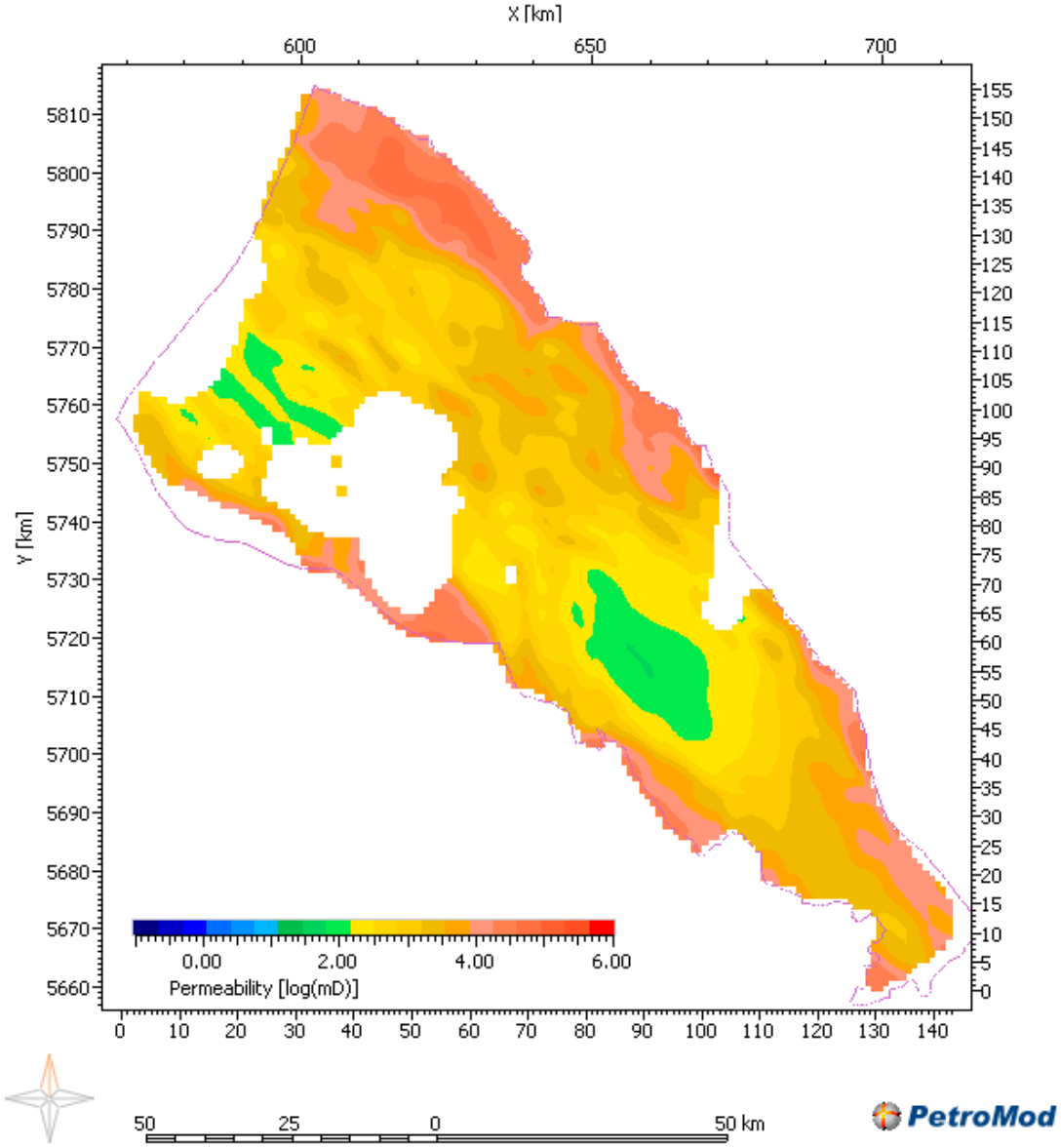

Figure 73 Calculated permeability of layer ROSL

9.6 Appendix 6 Calculated thermal conductivity maps for selected reservoir layers

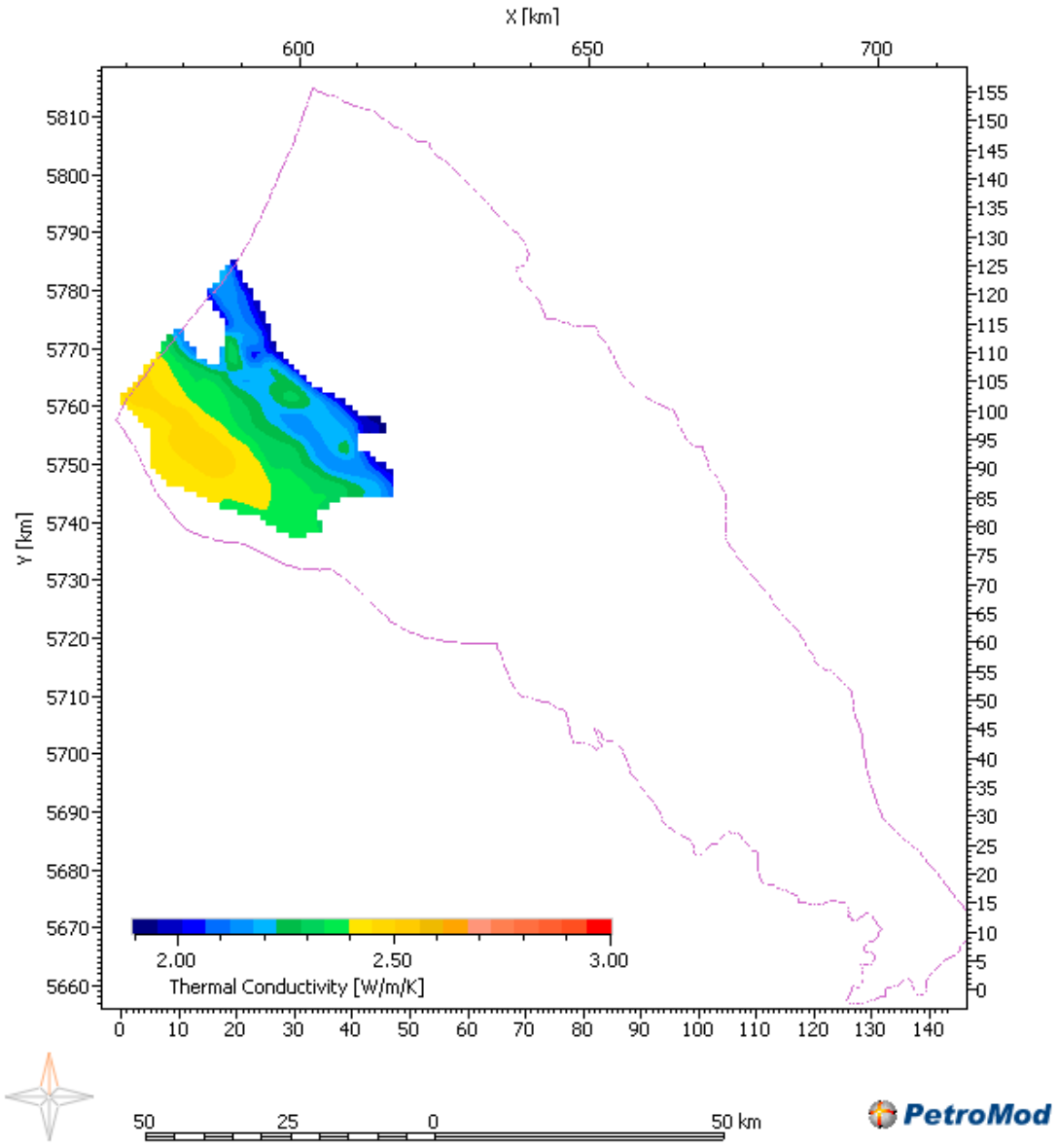

Figure 74 Calculated thermal conductivity of layer KNNSC

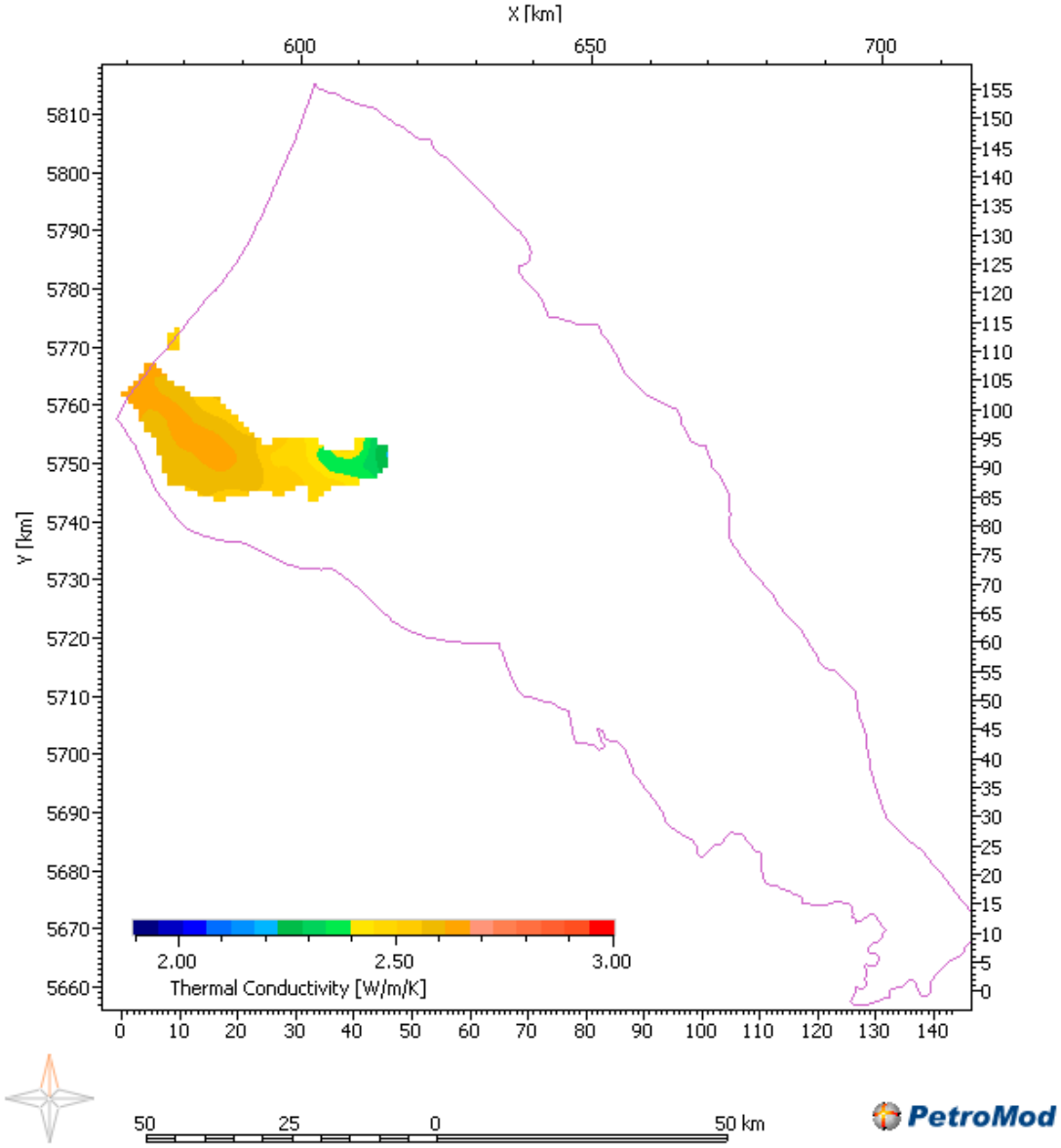

Figure 75 Calculated thermal conductivity of layer KNNSY

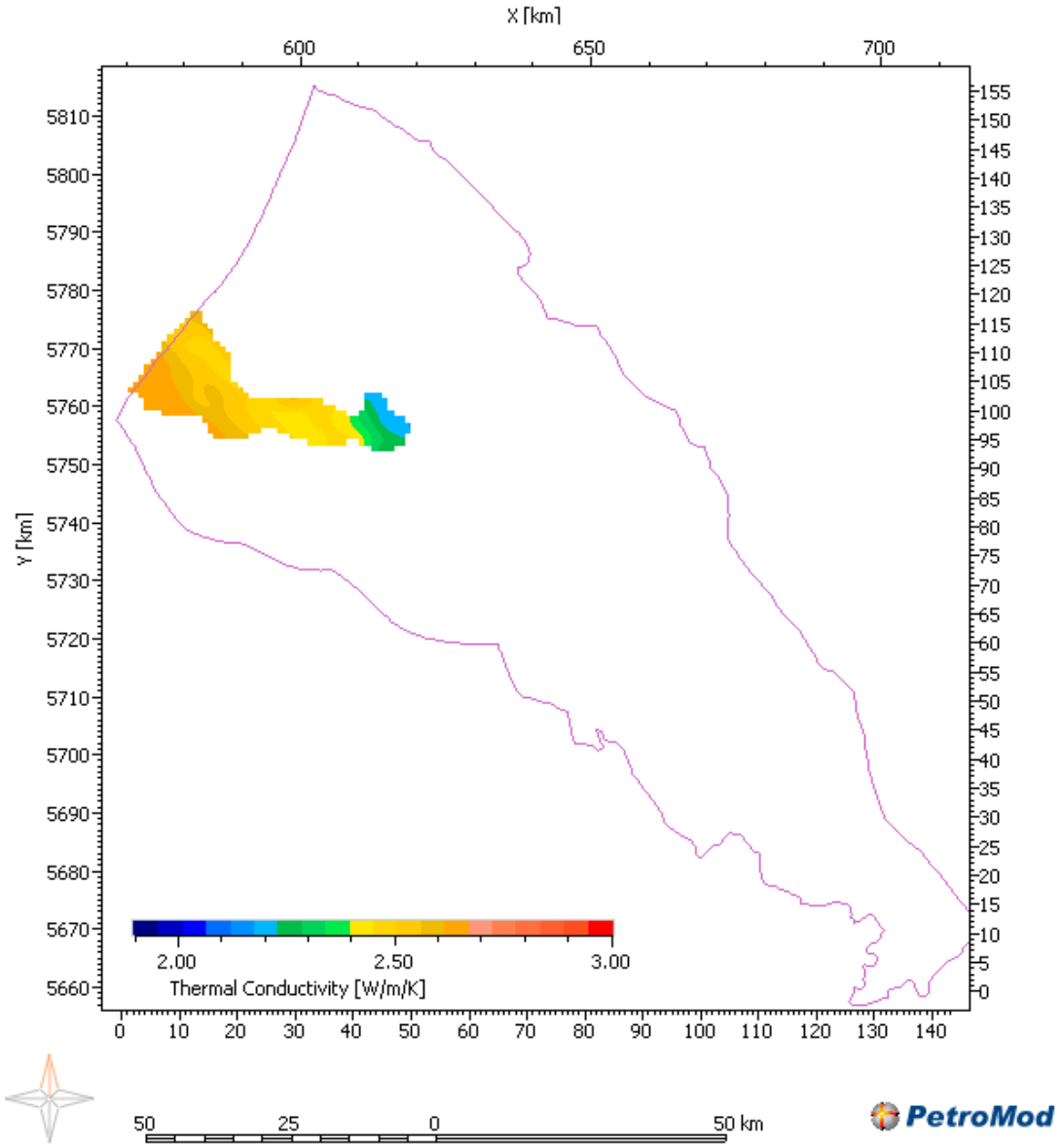

Figure 76 Calculated thermal conductivity of layer KNNSB

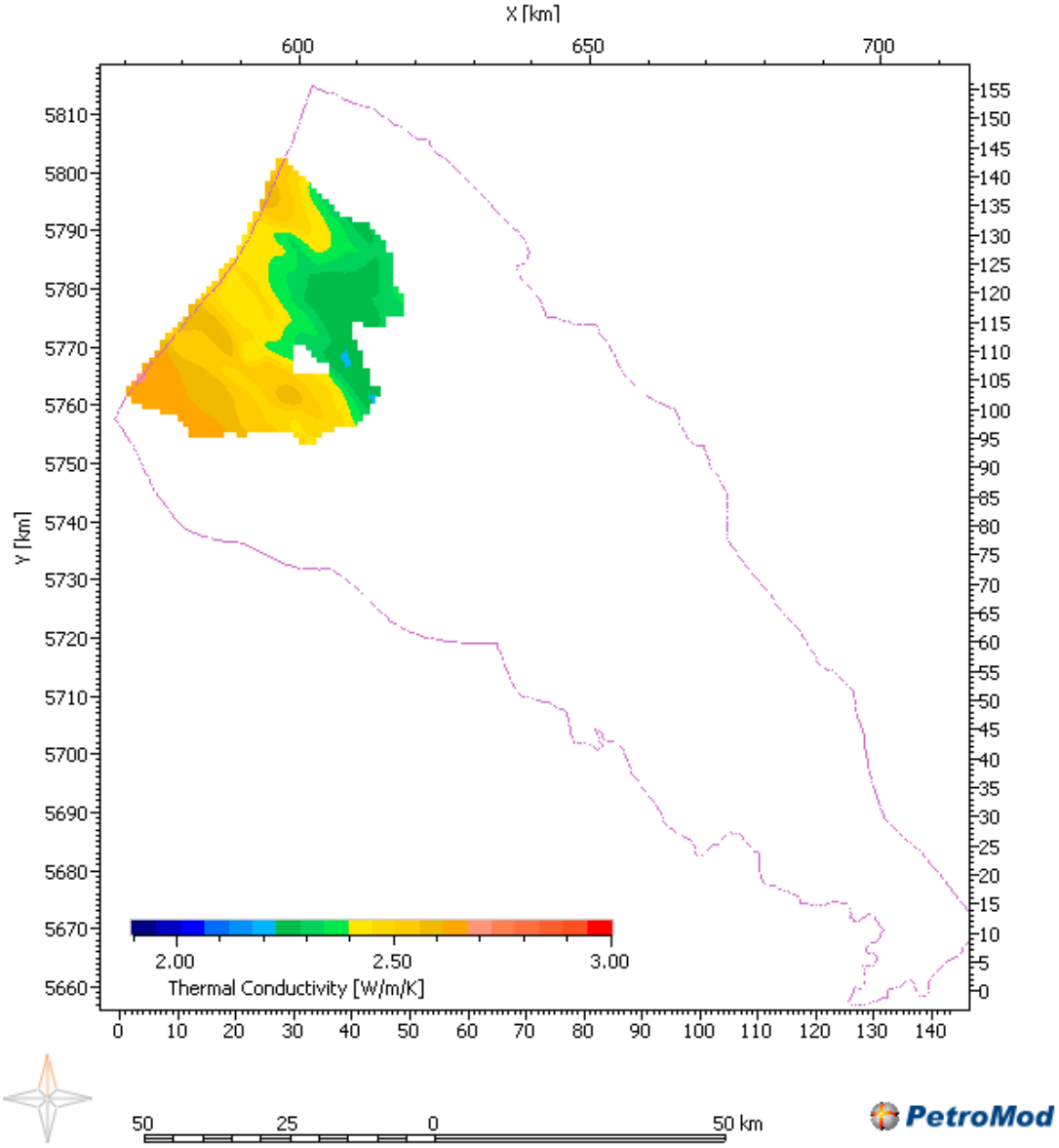

Figure 77 Calculated thermal conductivity of layer KNNSR

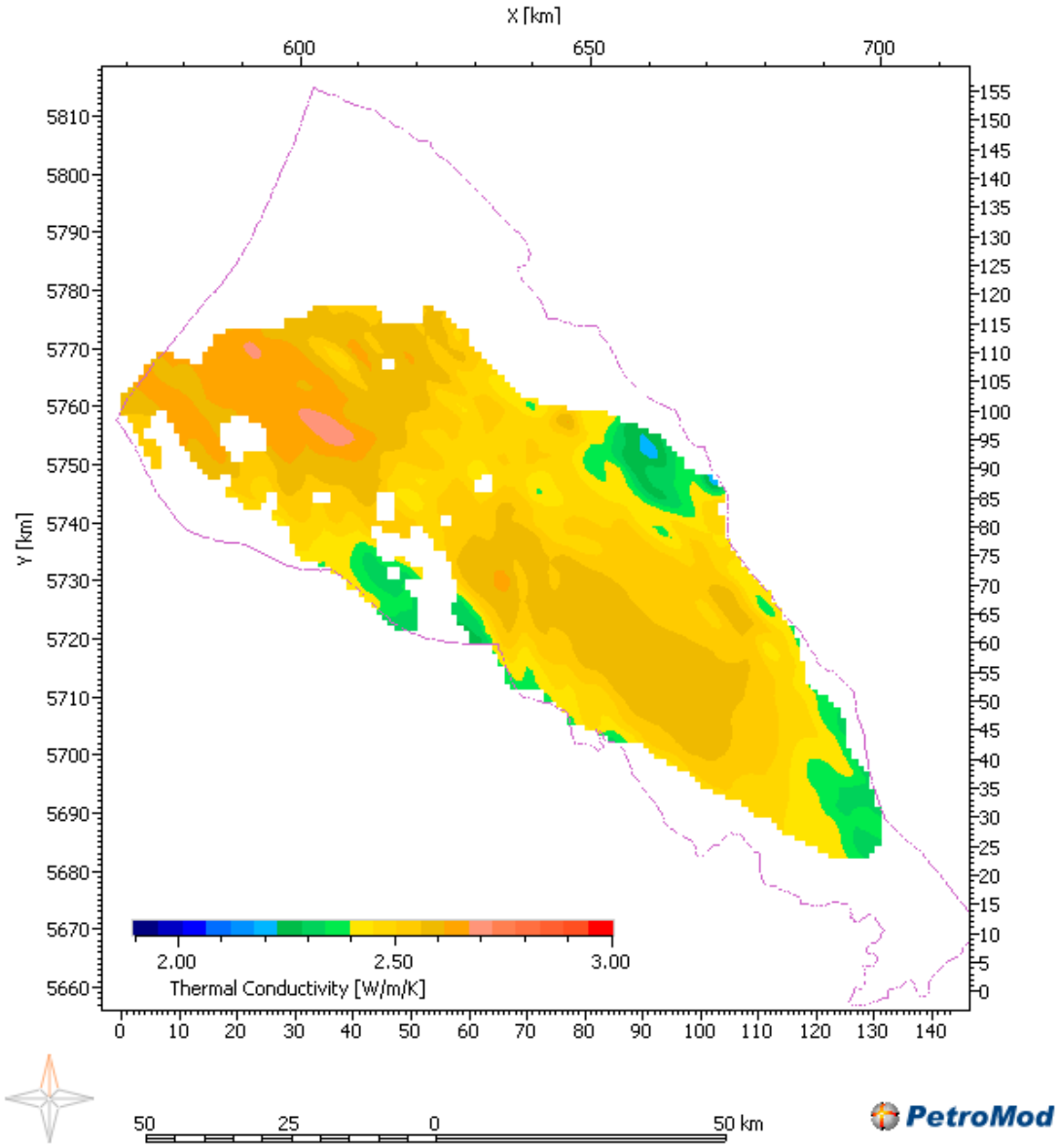

Figure 78 Calculated thermal conductivity of layer RNROF

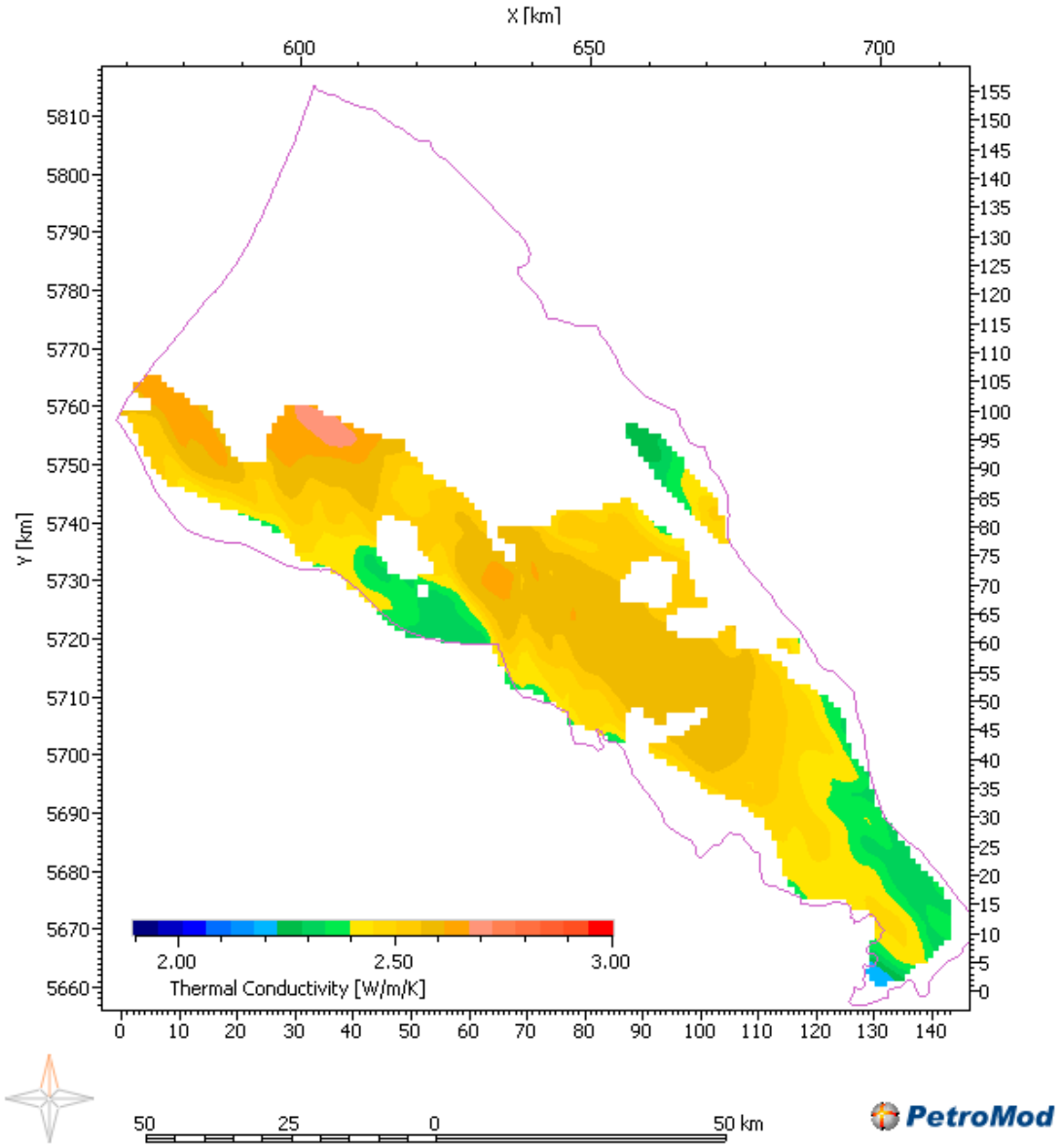

Figure 79 Calculated thermal conductivity of layer RBMH

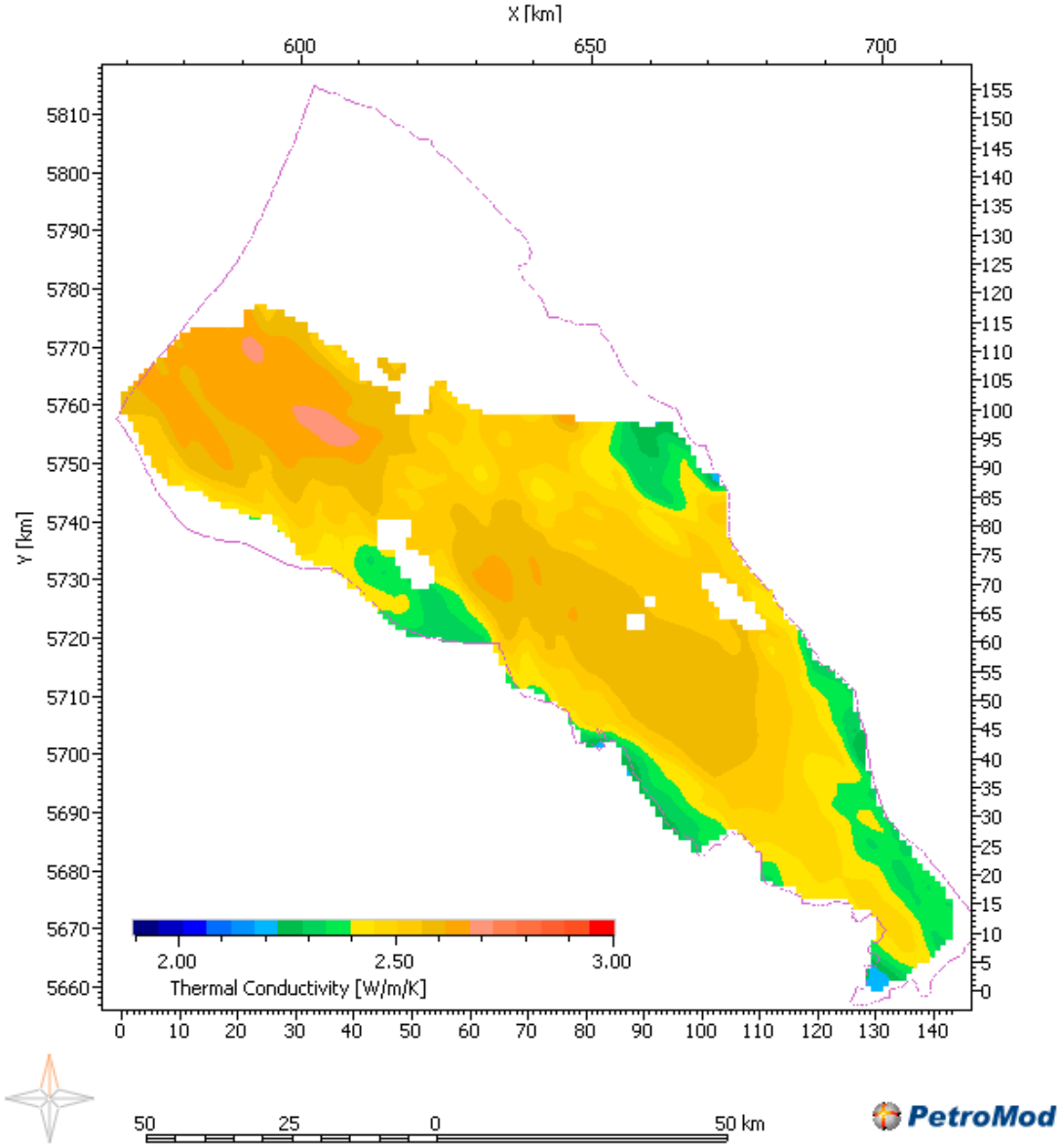

Figure 80 Calculated thermal conductivity of layer RBMDL

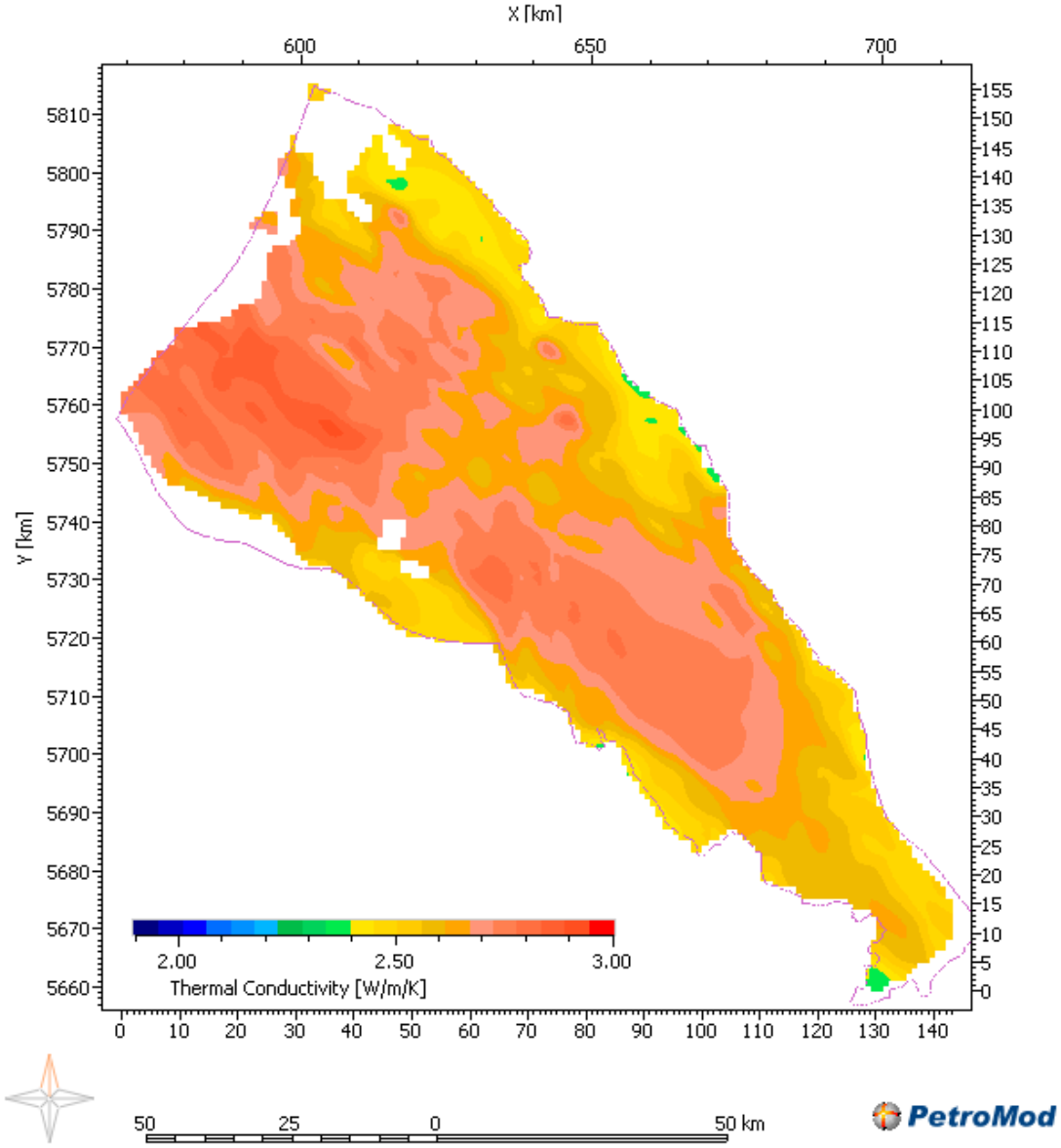

Figure 81 Calculated thermal conductivity of layer RBMVU

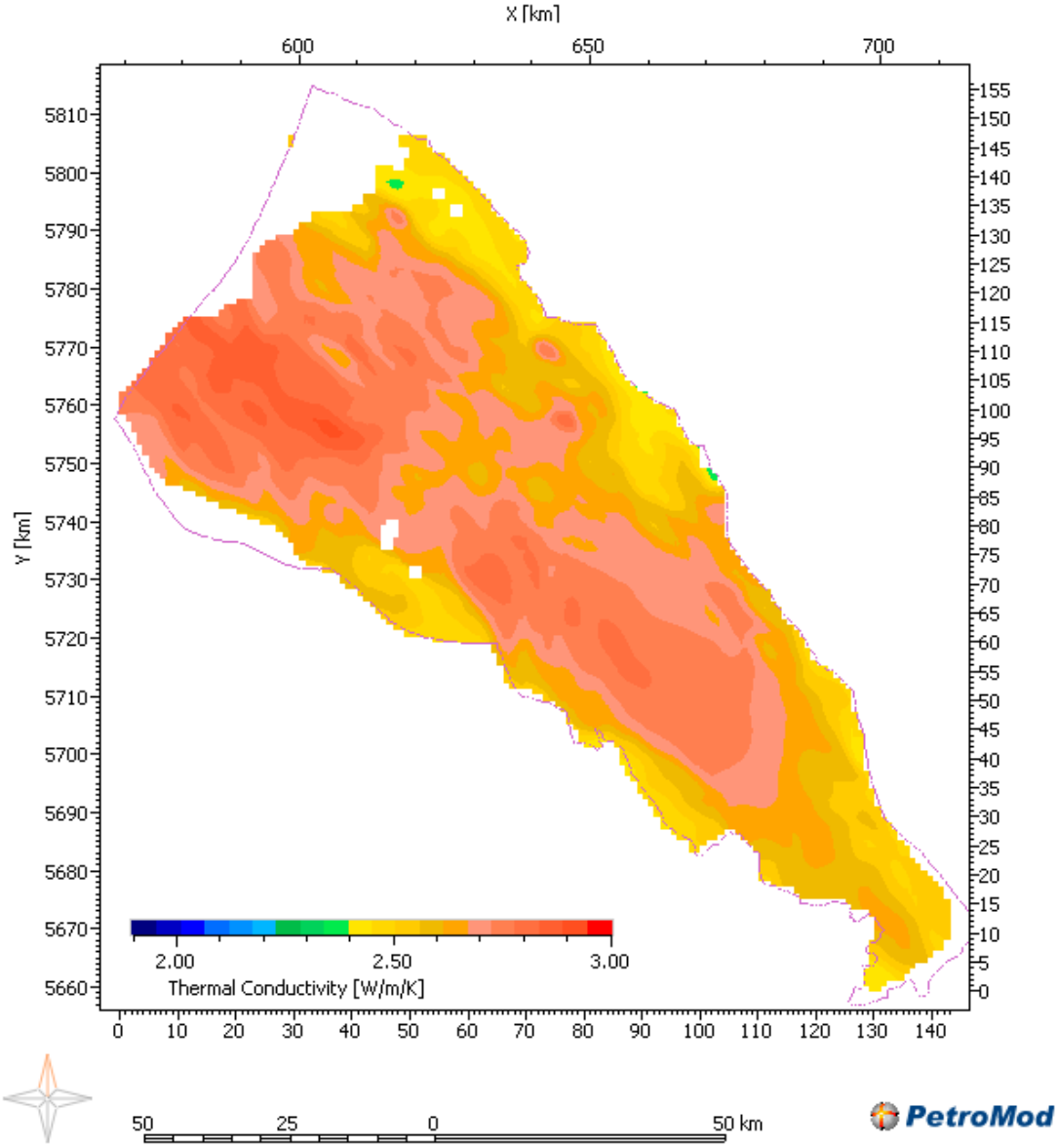

Figure 82 Calculated thermal conductivity of layer RBMVL

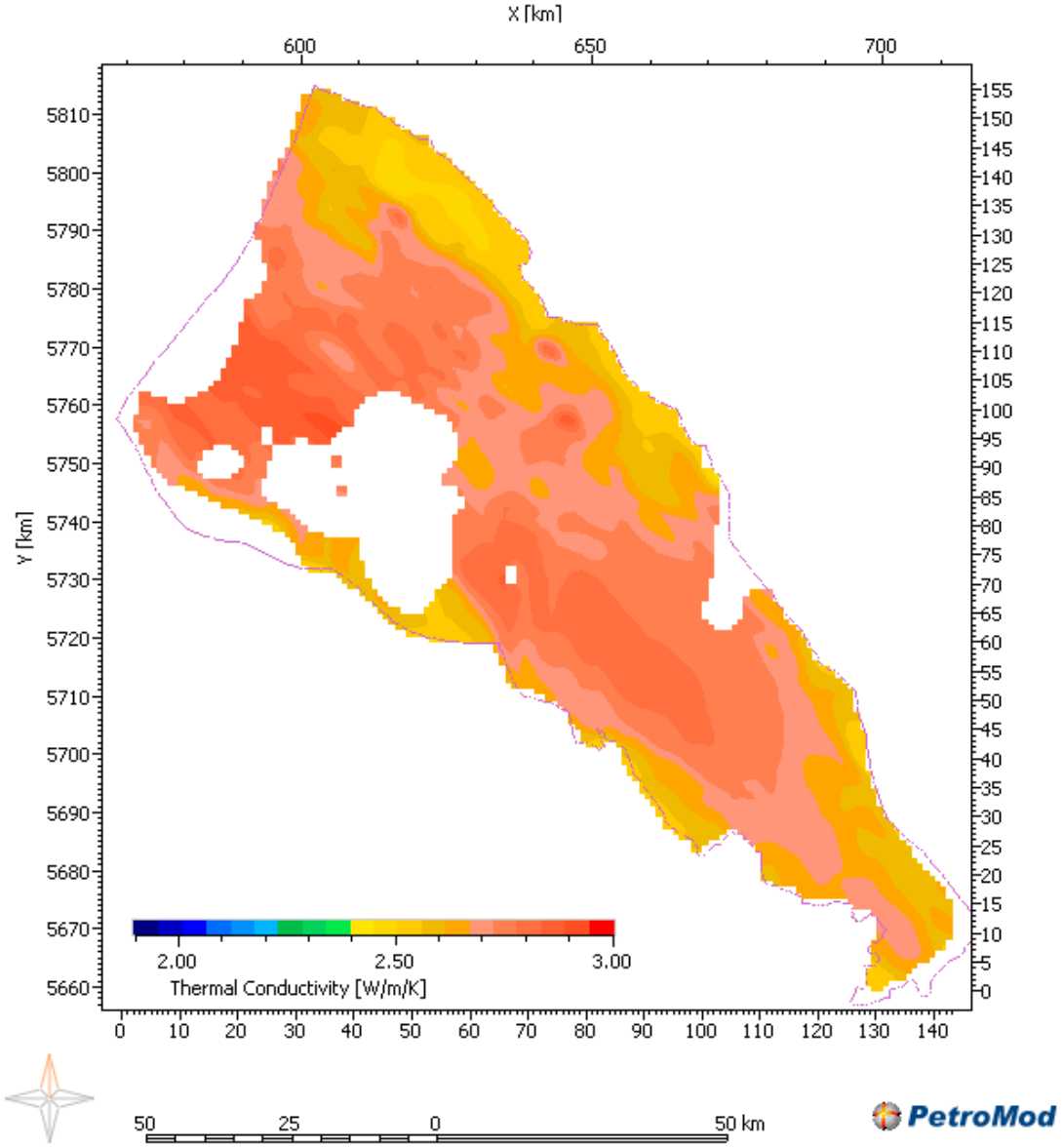

Figure 83 Calculated thermal conductivity of layer ROSL

10 Signature

Utrecht, <datum>	Placeholder
<naam afdelingshoofd> J.M. Verweij Head of department	S. Nelskamp Author